STUDIES OF AN AIR COOLER UNDER FROST CONDITION

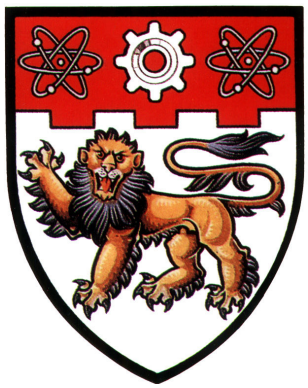

CHENG YEONG CHANG

SCHOOL OF MECHANICAL AND AEROSPACE ENGINEERING

NANYANG TECHNOLOGICAL UNIVERSITY

2006

Studies of an Air Cooler Under Frost Condition

Cheng Yeong Chang

School of Mechanical and Aerospace Engineering

A thesis submitted to Nanyang Technological University
in fulfillment of the requirements for the degree of
Doctor of Philosophy

2006

Abstract

Frost accumulation on an air cooler, a direct result of combined heat and mass transfer between the moist air flowing across a cold surface, causes heat transfer performance degradation due to the insulating effect of frost layer and the coil blockage as the frost grows. The complex geometry of finned tube air cooler leads to uneven wall and air temperature distribution inside the coil, and causes variations of frost growth rate and densification along the coil. In this study, a general distributed model with frost formation was developed. The equations for finned tube heat exchanger were derived in non-steady-state manner and quasi-steady state in the frost model. In order to make the model more realistic, the variation of frost along fin due to uneven temperature distribution was included. The presented model is able to predict the dynamic behavior of an air cooler both under non-frost and frost condition. Results include frost accumulation and its effect on energy transfer, air off-coil temperature, refrigerant liquid dry-out position and propagation of frost formation along the coil. Comparisons were made based on the frost mass accumulation, pressure drop across coil and energy transfer coefficient, and results were found to agree well with reported experimental results.

A field investigation was performed on the frost formation at an evaporator of a commercial full-scale refrigerated container that uses R-12 as the working refrigerant. Results show that the model is capable of predicting the dynamic behavior of a direct expansion evaporator under both non-frosting and frosting conditions. The air outlet and energy transferred compare well between experiment

and model, and within 20 % for the air pressure drop. The frost occurrence and propagation agree well generally, with the frost formation first occurring at the first row where the refrigerant enters the evaporator.

Acknowledgements

I would like to express my deepest gratitude to my supervisors, Assistant Professor Alvin Lai Chi Keung and Professor Tso Chih Ping for their guidance, advice, enthusiasm and ceaseless support throughout the entire project. It has been a great honour and pleasure to work with them. Without their patience and painstaking dedication, this project would not have been possible.

I would also like to extend my gratitude to Mr. Ng S.M. and Dr. Qin Wei of Carrier Transicold Pte Ltd, Singapore and Dr. Xiguo Jia for their technical advice on this study. .

I wish to acknowledge gratefully the Postgraduate Student Scholarship from Nanyang Technological University, without which I would not have a chance to work and learn in this program.

In everything I give thanks to God who I trust with my life, career and family. I thank Him for supportive and loving parents, siblings, my wife, Irene Ling Wen Lan and my lovely daughter, Joanna Cheng Wei Yi. I graciously admit that without their patience and encouragement, I would truly fall short of many goals in my life. Thank you for all of these blessings.

Table of Contents

List of Figures

List of Tables

Publication arising from this thesis

Journal articles

[1]. C.P. Tso, Y.C. Cheng and A.C.K. Lai, 2006, "An improved model for predicting performance of finned tube heat exchanger under frosting condition, with frost thickness variation along fin", Applied Thermal Engineering, 26(1), pp. 111-120.

[2]. C.P. Tso, Y.C. Cheng and A.C.K. Lai, 2006, "Dynamic behavior of a direct expansion evaporator under frosting condition. Part I: Distributed model", International Journal of Refrigeration. (*In press*)

[3]. C.P. Tso, Y.C. Cheng and A.C.K. Lai, 2006, "Dynamic behavior of a direct expansion evaporator under frosting condition. Part II: Field Investigation on a shipping container", International Journal of Refrigeration. (*In press*)

Nomenclature

A_{free} - outside minimum flow area (m^2)

A_i - cross section area of tube inside (m^2)

$A_{i,t}$ - inside area of tube per meter (m^2/m)

A_o - cross section area of tube outside (m^2)

$A_{o,t}$ - outside area of tube wall per meter (m^2/m)

$A_{r,\ell}$ - cross section area of liquid refrigerant (m^2)

$A_{r,v}$ - cross section area of vapor refrigerant (m^2)

$A_{t,f}$ - $A_{fin} + A_{tube}$ (m^2)

$c_{p,fin}$ - fin specific heat (kJ/kg K)

$c_{p,a}$ - specific heat of air (kJ/kg K)

$c_{p,w}$ - specific heat of tube wall (kJ/kg K)

D - diameter of tube (m)

D_v - binary diffusion coefficient for water vapor in air at the frost temperature (m^2/s)

D_c - collar diameter (m)

D_h - coil hydraulic diameter ($4A_{free}L_dL/A_{t,f}$)

f_{wv} - friction between liquid refrigerant and wall per meter (N/m^3)

$f_{w\ell}$ - friction between vapor refrigerant and wall per meter (N/m^3)

$f_{v\ell}$ - friction between vapor and liquid refrigerant per meter (N/m^3)

f_x - friction pressure loss per meter, $f_x = f_{wv} + f_{w\ell}$ (N/m^3)

G_r - refrigerant mass flux (kg/m^2 s)

h_a - enthalpy of air (kJ/kg)

h_{fin} - enthalpy of air at fin surface (kJ/kg)

$h_{fst,s}$ - enthalpy of air at frost surface (kJ/kg)

$h_{r,\ell}$ - enthalpy of liquid refrigerant (kJ/kg)

$h_{r,v}$ - enthalpy of vapor refrigerant (kJ/kg)

$\tilde{h}_r$ - mixed enthalpy of refrigerant (kJ/m^3) (equation 3.31)

h_{sg} - enthalpy of sublimation (J/kg)

h_w - enthalpy of air at wall (kJ/kg)

j_a - Colburn j factor

K - entrainment factor (equation 3.12)

k_a - thermal conductivity of air (W/m K)

k_{fin} - thermal conductivity of fin (W/m K)

k_{fst} - thermal conductivity of frost (W/m K)

k_{ice} - thermal conductivity of ice (W/m K)

k_w - thermal conductivity of wall (W/m K)

$k_{r,\ell}$ - thermal conductivity of liquid refrigerant

$k_{r,v}$ - thermal conductivity of vapor refrigerant

Le - Lewis number (ratio of thermal diffusivity to mass diffusivity, $\frac{U_o}{c_{pa} U_m}$)

M_t - total number of cells

M_w - mass per meter of tube wall (kg/m)

$\dot{m}_{lv}$ - phase change liquid to vapor refrigerant (kg/m^3 s)

$\dot{m}_v$ - mass flux from air to frost (kg/m^2 s)

$\dot{m}_\delta$ - mass flux for increase in thickness (kg/m^2 s)

$\dot{m}_{\rho}$ - mass flux for increase in density (kg/m^2 s)

m_a - air mass flow rate (kg/s)

m_r - refrigerant mass flow rate (kg/s)

N_r - number of row

Pr - Prandtl number (ratio of momentum diffusivity to thermal diffusivity, $\frac{\mu c_p}{k}$)

p_r - refrigerant pressure (Pa)

P_a - air pressure (kPa)

ΔP_a - pressure drop across coil (Pa)

Q - total energy transfer (W)

q_{fin} - heat transfer rate per meter to fin (W/m)

q_t - heat transfer rate per meter to tube (W/m)

$\dot{q}_{a,fst}$ - heat flux at frost air interface (W/m^2)

$\dot{q}_{tr}$ - heat flux from tube to refrigerant (W/m^2)

Re_a - Reynolds number for air (ratio of inertial force to viscous force, $\frac{G_a D_h}{\mu_a}$)

$Re_{r,\ell}$ - Reynolds number for liquid refrigerant flow ($\frac{G_r D}{\mu_{r,\ell}}$)

r_o - tube outside radius (m)

S - slip ratio

S_{fin} - fin spacing (m)

S_{fin} - fin spacing (m)

T_a - temperature of air (K)

T_{fin} - temperature of fin (K)

T_{fst} - temperature of frost (K)

$T_{fst,s}$ - temperature at frost air interface (K)

T_r - temperature of refrigerant (K)

T_w - temperature of wall surface (K)

t - time (s)

u_r - refrigerant velocity (m/s)

$u_{r,\ell}$ - velocity of liquid refrigerant (m/s)

$u_{r,v}$ - velocity of vapor refrigerant (m/s)

U_m - mass transfer coefficient of outside air (kg/s m^2)

U_o - heat transfer coefficient of outside air (W/m^2 K)

U_r - heat transfer coefficient of refrigerant (W/m^2 K)

$U_{t,r}$ - heat transfer coefficient from tube to refrigerant (W/m^2 K)

X_l - longitudinal tube pitch (m)

X_t - transverse tube pitch (m)

x - coordinate axis in the direction of refrigerant flow (m)

y - coordinate axis in the direction of air flow (m)

z - coordinate axis in the direction normal to cold surface (m)

Greek Letters

α - void fraction

δ_{fin} - fin thickness (m)

δ_{fst} - frost thickness (m)

δ_w - wall thickness (m)

$\mu_{r,\ell}$ - viscosity of liquid refrigerant (Pa s)

$\mu_{r,v}$ - viscosity of vapor refrigerant (Pa s)

ρ_a - density of air (kg/m^3)

$\rho_{a,v}$ - density of water vapor in air (kg/m^3)

ρ_{fin} - density of fin (kg/m^3)

ρ_{fst} - density of frost (kg/m^3)

ρ_{ice} - density of ice (kg/m^3)

ρ_r - density of refrigerant (kg/m^3)

$\rho_{r,\ell}$ - density of liquid refrigerant (kg/m^3)

$\rho_{r,v}$ - density of vapor refrigerant (kg/m^3)

$\tilde{\rho}_r$ - average density of liquid and vapor refrigerant (kg/m^3)

σ - surface tension (N/m)

τ - tortuosity factor

χ - refrigerant vapor quality

ω_a - absolute air humidity (kg/kg)

$\omega_{fst,\,s}$ - absolute air humidity at frost air interface (kg/kg)

ω_w - absolute air humidity at wall surface (kg/kg)

Φ_{fst} - absorption coefficient (as defined in Eq. 3.70)

CHAPTER 1
Introduction

1.1 Background

Evaporator or air cooler absorbs heat from the air as the air passes through the coil. If the surface temperature of the air cooler is below the dew point temperature of the moist air, mass transfer by condensation of the water vapor will occur. When the surface temperature reaches below the freezing temperature (0^{o}C at normal atmospheric pressure), water droplets on the cold surface will subsequently freeze and form frost. The frost accumulation is a direct result of the combine heat and mass transfer between the moist air flowing across a cold surface and the cold surface.

Frost is comprised of air trapped in a porous matrix of ice crystal. During frost growth, heat is transferred from the warmer humid air adjacent to the frost-air interface by convection and conducted to the colder heat exchanger through the frost layer. Water vapor is diffused by molecular diffusion through the frost layer towards the cold heat exchanger surface. Phase change from vapor to ice crystals occurs both at the air-frost interface and within the frost layer. This process releases the latent heat of sublimation. During the development of frost layer, the frost properties vary continuously. The frost-air interface temperature changes both with respect to time and position because of the change in the frost property. As the interface temperature changes, the partial pressure of water vapor at the surface also changes,

thus changing the thermal and diffusion boundary layers and eventually affecting the heat transfer and frost growth rates. Further complications arise due to the occurrence of repeated cycles of melting and refreezing, known as melt-back phenomenon/ permeation process, once the air frost interface temperature reaches the freezing temperature. This will result in structural changes in the frost layer that tends to increase both the frost density and thermal conductivity with time, without a proportional increase in the frost thickness. This phenomenon is more likely to occur in high humidity and/or high temperature environments than in low humidity and low temperature ones. In the latter case, the frost-air interface temperature will rise to a steady value, below melting point, such that the rate of frost deposition is balanced by the rate of sublimation from the frost. In short, the frosting process is a complicated phenomenon involving simultaneous heat and mass transfer with phase change and a moving boundary under unsteady condition.

The existence of frost on the surface of air cooler is undesirable and it is a common problem in refrigeration system. As the frost grows, it acts to block the air flow passage. This blockage causes decrease in the air flow area and result in higher pressure drop across the coil and hence affects the fan system characteristics. The porous structure of frost contains low thermal conductivity air pores that lead to low thermal conductivity of frost layer. This layer results in a significant heat transfer resistance from the air to the air cooler surface. It acts as insulation to the cold evaporator surface from the warmer air which results in reduction in heat transfer rate between the air and the refrigerant. The reduction in airflow and increased thermal resistance reduce the heat energy extracted by the evaporator and decrease

the system capacity and efficiency. When the evaporator heat transfer rate is reduced, the evaporator temperature drops and suction pressure drops. This lower evaporator temperature may create mechanical problems in the system such as liquid refrigerant flooding back to the compressor, since less refrigerant boils off. To prevent damage to the system and maintain the system performance, periodic defrost is required. During the defrosting cycle, it is noted that power consumption still occurs, melting the frost on the evaporator without cooling capacity. Frequent or long defrosting cycles cause the energy consumption to increase and the system efficiency to decrease. This defrost process extracts an additional penalty in the energy consumption. Defrost process using hot gas or electric heater supplied heat to raise the temperature of the air cooler above freezing point. Niederer (1976) indicated that only 15% to 20% of the heat supplied was actually carried out for defrosting while the rest of the heat input increased the temperature of the air cooler and it was lost to the surrounding enclosure. The water evaporated during defrost cycle often ends up back on the air cooler in the next cycle of operation.

To cater for the capacity lost due to frost accumulation, designs of refrigeration systems currently used in the industry often oversize the coil by about 50% as compare to the case of no frost, while the average energy input is 25% greater than the same system with no frost accumulation (Chen et al. 2002). The penalty of over sizing the coil could be close to optimum design if the characteristics of the frost growth and its impact on the performance of the air cooler are better understood. The elements should be considered and modeled are the heat and mass

transfer coefficients, air side friction factor and change of the geometrical shape of the evaporator due to the frost deposition.

Considerable work has been done on frost formation and properties in simple geometries such as flat plate and cylinder. The literature available on finned tube heat exchangers with regards to frosting is limited due to its complex geometries. The results of the studies on frost growth on finned tube heat exchanger have shown that there are large temporal and spatial variations in the frost growth which depend on the design of the heat exchanger and its operating conditions (Ogawa et al. 1993). In spite of the large number of refrigeration, heat pump and heat recovery applications, designing heat exchanger surfaces to accommodate frost growth and selecting defrost cycles have been limited to test results of specific equipment due to the lack of empirical data and theoretical model of frost growth (Oskarsson et al. 1990a; Senshu et al. 1990; Rite and Crawford 1991a; Ismail et al. 1999). Such studies, although essential for the efficient operation of heat exchangers under frosting conditions, do not give all the information required for the design of surface and air flow geometry for frost accumulation and defrosting heat exchanger.

The problem with heat exchangers under frosting condition is very complicated because frost growth and the properties vary with location and time. There are seven or more independent operating and design variables for heat exchangers with frost growth, namely, time, coil depth, coil surface temperature, air supply temperature, humidity, air velocity and coil geometry. Correlating such frost data with seven or more independent variables would be very difficult and for some

variables such as humidity and temperature, the uncertainty is large. This could cause poor reliability of correlations.

1.2 Research Objectives and scope

The main purpose of this research was to develop a mathematic model to predict the transient performance of the evaporator for condition with and without the presence of frost. The refrigeration system commonly used utilizes volatile refrigerant as working fluid. Owing to the two-phase evaporating flow inside the coil, the condition of air properties such as temperature and humidity inside the coil varies. Therefore, a general distributed model with two-phase flow and single-phase flow for refrigerant coupled with a frost model was developed for dynamic response of an evaporator. The model was developed based on fundamental heat and mass transfer and it allows for a variety of environmental input conditions. An iterative quasi-steady state approach was used to compute the frost-air interface temperature, partial pressure of water vapor at the frost surface and the frost property. The model provides the capability for adjusting the frost density and thermal conductivity properties. The performance degradation due to the heat transfer resistance that resulted from the growth of frost layer can also be included.

A field investigation on a commercial container refrigeration system was carried out and the operation data was measured and collected. The results obtained from the field investigation were compared with the predicted results from the model. Apart from that, results from other investigators are compared with the predicted results using the model developed.

1.3 Overview of the Report

Chapter 2 provides literature survey on the fundamental studies of frost properties, frost growth and the overall impact of frost on the performance of finned tube air cooler. The discussion on the performance of finned tube air cooler will be the focus since that is of primary concern in the present study. The mathematical model of the evaporator and frosting process is discussed in Chapter 3. This includes the distributed modeling of two-phase and single-phase refrigerant, air and frost characteristic. The governing equations for the heat and mass transport processes were derived using local averaging techniques for mass, momentum and energy transport.

Results of the simulation program are presented in Chapter 4. Comparisons of results from the existing experimental data are presented. A description of the field investigation is presented in Chapter 5. Schematic diagrams and explanation of the commercial container refrigeration system are included. Results from the field investigation and model are presented. The summary and conclusions of this research study are presented in Chapter 6.

CHAPTER 2

Literature Review

A review of published research has been conducted. It is found that a substantial amount of literature is available on the general topic of frost formation and growth. Early studies on frost were concentrated on frost properties, mechanism of frost growth and heat transfer for simple geometry such as flat plates, parallel plates, tubes and cylinders. The studies on frost formation and growth on finned tube coils are limited. This could be attributed to the very large number of variables involved and to the complexity of the surface geometry of the finned tube air cooler/heat exchanger. The literature review is organized into these different sections: (1) frost property, (2) frost growth and (3) frost on finned tube heat exchanger. This review will focus more onto the studies on frost formation and growth on finned tube heat exchanger.

2.1 Frost Property

The property of frost is important and will be used in the analytical and mathematical modeling of frost growth. Therefore, it is important to have a better understanding and knowledge of the property of frost.

Frost thermal conductivity, k_{fst}, and density, ρ_{fst}, are two properties that have major effects on the heat transfer and frost growth calculations. The frost density is dependent on the structure of the frost layer; therefore, it is affected by the

environmental parameters such as temperature, diffusion and deposition of the water vapor within the frost layer. The thermal conductivity of frost changes as the frost density varies because they are related.

There is a general consensus in the literature that a relationship exists between these two properties. Chen and Rohsenow (1964), Chung and Algren (1958b) and Yamakawa et al. (1972) concluded that the frost thermal conductivity not only plays a major role in the heat transfer mechanisms, but increases with frost density. As frost forms on the cold surface, both of these properties can change by an order of magnitude. A change in one property usually indicates changes in the others. A number of investigators have made both experimental and theoretical studies to determine the rate of heat transfer and thermal conductivity but the results are inconclusive. O'Neal and Tree (1985) summarized most of the available literature before 1985.

Yonko and Sepsy (1967) carried out comparison on correlations for frost density and thermal conductivity available in the literature in 1967. They correlated their experimental data of frost thermal conductivity as a function of density. However, their experimental data was considerably scattered. They concluded that the conductivity of frost was a function of factors other than the frost density. Their correlation is valid for frost densities less than 573 kg/m^3.

Brian et al. (1969) and Biguria and Wenzel (1970) observed that the frost density had no spatial variation in the direction of frost growth. They correlated the

frost thermal conductivity not only with density but also the frost surface temperature, air velocity and humidity.

Jones and Parker (1975) assumed the frost density was spatially invariant to calculate the change in vapor mass flux with distance. With this approach, vapor diffusion in frost layer is postulated and they derived a semi-empirical model with application range of 50 to 130 kg/m^3 in density.

Marinyuk (1980) correlated frost thermal conductivity with frost density, frost surface temperature and wall temperature. His correlation was limited to frost densities up to 300 kg/m^3.

Dietenberger (1983) developed a method of calculating the frost thermal conductivity based on both theory and experimental data. His model, which was mostly fundamental and partly empirical, postulated a complicated frost structure which accounted for vapor diffusion, geometrical shapes of ice dendrites and for frost aging. It is basically a random mixture model with ice crystal and ice spheres immersed in moist air as the predominating structure at high densities. The proportions of these various structures were then calculated using experimental data and a generalized correlation of frost thermal conductivity was presented which depended on frost temperature and density. The range of application was $\rho_a < \rho_{fst} < \rho_{ice}$, 80 K < T_w < 273 K.

Ostin and Anderson (1991) and Lee et al. (1994) developed an empirical model as a function of density. Their model behaved poorly for the early stages of frost formation during which the frost density is low.

Mao et al. (1999) tested the frost properties with the variation of environmental parameters on a flat plate. They gave an empirical correlation that included the effect of humidity, temperature, air velocity and time on frost density and thermal conductivity. The correlation is valid only for the condition with cold plate temperature between -20 ^{o}C to -41 ^{o}C while supply air temperature range from -10 ^{o}C to -26 ^{o}C.

In the fundamental studies of frost formation on flat plate surfaces, Hayashi et al. (1977) described that frost formation can be divided into three periods:

a) crystal growth period

b) frost layer growth period

c) frost layer full growth period.

They developed correlations for the density of frost as a function of surface temperature. The relationship between the thermal conductivity and density of frost was not considered in their correlation and the restriction of the model validity is unclear.

Table 2.1 shows some of the earlier frost thermal conductivity and frost density correlations. Figure 2.1 shows comparison of some earlier frost thermal conductivity models. It shows that there is a wide spread in the predicted thermal conductivity for a particular frost density.

Table 2.1: ***Earlier frost thermal conductivity and frost density correlation***

Investigator	Correlation of Thermal Conductivity and Density	Range of application	Note
Yonko and Sepsy (1967)	$k_{fst} = 0.0140 + 0.00668\rho_{fst} + 0.000175\ \rho_{fst}^{2}$ (2.1) where ρ_{fst} in lb/ft^3, k_{fst} in Btu/(hr.ft.F).	T_w = 14 to -22^{o}F (-10 to -30^{o}C) T_a = 68 to 77^{o}F (20 to 25^{o}C)	Empirical
Brian et al. (1969)	$k_{fst} = 8.49\times10^{-17}T_{fst}^{5.44} + 6.86\times10^{-14}(\rho_{fst} - 0.025)T_{fst}^{4.84}$ (2.2) where ρ_{fst} in lb/ft^3, k_{fst} in Btu/(hr.ft.R) and T_{fst} in R	T_{fst} = 0 to 20^{o}F (-18 to -7^{o}C) ρ_{fst} = 1.6 to 8.1 lb/ft^3 (25 to 130 kg/m^3)	Empirical. This model could only be applied during early stage of frost growth due to small density range
Sanders (1974)	$k_{fst} = (1.202 \times 10^{-3})\ \rho_{fst}^{0.963}$ (2.3) where ρ_{fst} in kg/m^3, k_{fst} in W/(m.K)	T_w = -8 to 12^{o}F (-22 to 11^{o}C) T_a = 14 to 32^{o}F (-10 to 0^{o}C) u_a = 13 to 30 fps	Empirical

		(4 to 9 m/s) ρ_{fst} < 31.2 lb/ft^3 (500 kg/m^3)	
Hayashi et al. (1977)	$\rho_{fst} = 650e^{0.277T_s}$ (2.4) where ρ_{fst} in kg/m^3 and T_s in ^oC	T_w = -10 to 0^oC u_a = 2 to 6 m/s ω_a = 0.0075 kg/kg$_a$	Empirical
Marinyuk (1980)	$k_{fst} = 1.3(T_s - T_w)[0.156e^{0.0137T_s} - e^{0.0137T_w}] + 5.59\times10^{-5}\rho_{fst}[e^{0.0214T_s} - e^{0.0214T_w}]$ (2.5) where k_{fst} in W/m.K, ρ_{fst} in kg/m^3 and T_s and T_w in ^oK	ρ_{fst} = 3.7 to 18.7 lb/ft^3 (60 to 300 kg/m^3)	Empirical
Lee et al. (1994)	$k_{fst} = 0.132 + 3.13\times10^{-4}\times\rho_{fst} + 1.6\times10^{-7}\times\rho_{fst}^2$ (2.6) where k_{fst} is in W/mK, ρ_{fst} is density of frost layer in kg/m^3	ρ_{fst} = 50 to 400 kg/m^3	Empirical

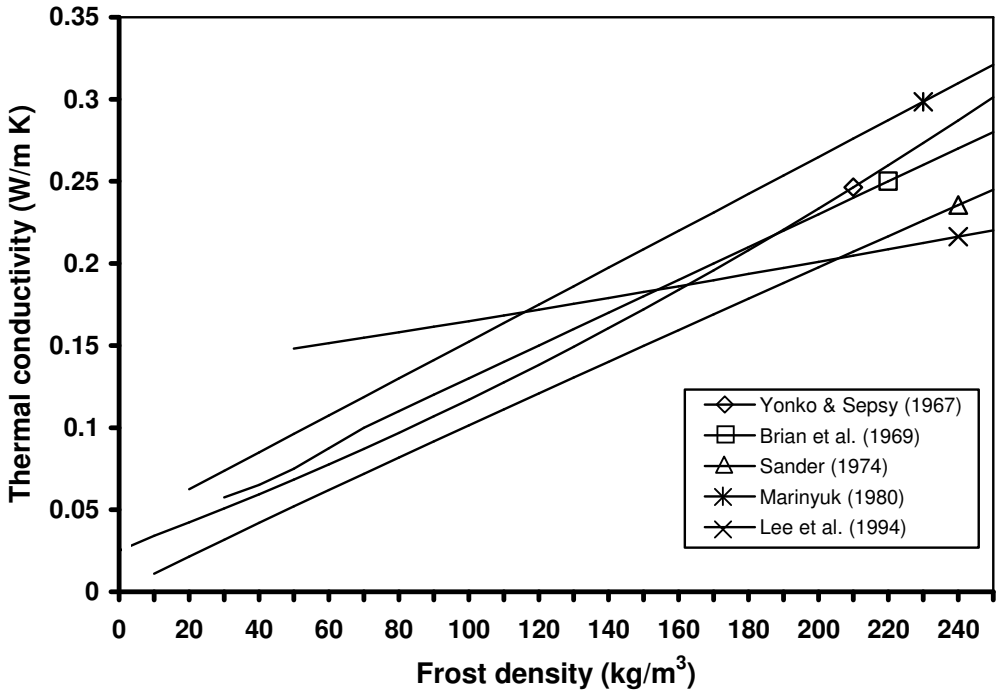

Figure 2.1: ***Variation in measured frost thermal conductivity as a function of frost density***

The wide variation probably results from a combination of differences in the internal crystalline structure of the frost for each investigation and differences in the porosity of the frost. Table 2.2 summarizes the observed frost crystal structure as a function of temperature (Mason and Hallet, 1971). Figure 2.2 shows some of the crystalline structure of frost mentioned in Table 2.2.

Table 2.2: ***Observed crystalline structure of frost as a function of plate temperature***

Temperature (^{o}C)	**Types of Crystals**
0 to -3	Thin hexagonal plates
-3 to -5	Needles
-5 to -8	Hollow prisms
-8 to -12	Hexagonal plates
-12 to -16	Dendrite crystals
-16 to -25	Plates
-25 to -50	Hollow prisms

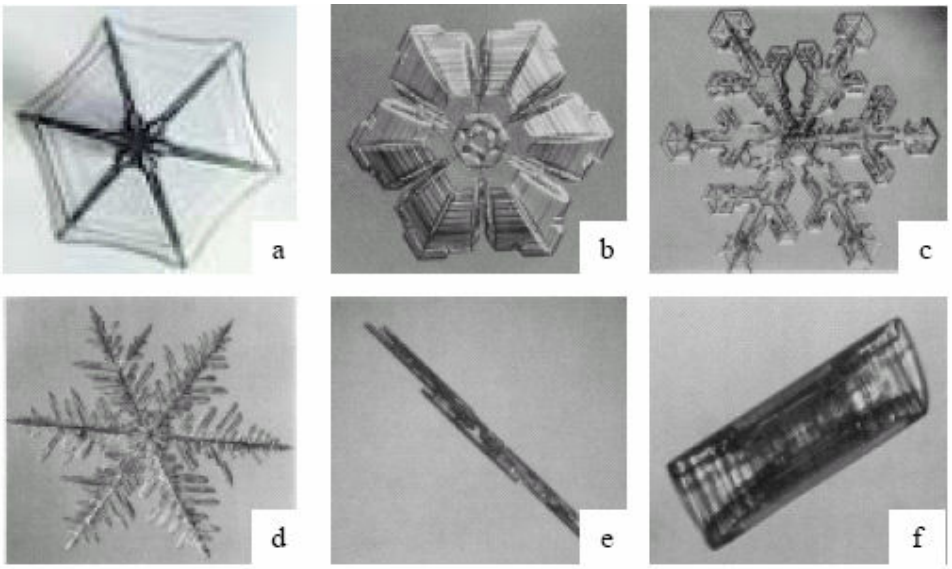

Figure 2.2: ***Crystalline structure of frost***

(Source:http://www.its.caltech.edu/~atomic/snowcrystals/primer/primer.htm)

a) plate, b) thin hexagonal plate, c) dendrite crystals, d) fern-like dendrite, e) needle and f) hollow prisms

Whenever a crystal is transferred to a new environment, the continued growth assumes a new habit characteristic. If the temperature of the frost surface reaches 0 ^{o}C, condensation occurs at the surface. This condensate soaks into the frost layer and freeze. It will affect the porosity, density, thermal conductivity and the water vapor migration in the frost layer. The rate at which the frost surface reaches 0 ^{o}C is dependent on the air temperature, air humidity, air flow rate and heat exchanger surface temperature. Therefore, the differences in these variables in the investigations may be the primary reason for the wide scattering in the data relating the thermal conductivity and density.

Table 2.2 also has implication for predicting frost growth in a particular experiment. If the wall initial temperature is at a very low temperature such as -40 ^{o}C, the frost with hollow prisms crystals will initially form at that temperature. As frost growth progresses, the surface temperature would eventually approach 0 ^{o}C. This will cause new frost with a difference structure than the initial frost forming on the top of the existing frost. It may also imply that two frost layers with identical density may have different thermal conductivity due to different frost layer. The shape and orientation of the ice crystals within the frost layer structure could affect the thermal conductivity as well. Therefore, the general rule for the relationship between the thermal conductivity and density should be used with caution. It is suggested that these correlations be utilized carefully and applied only in cases with conditions close to the experiments from which they were determined.

2.2 Frost Growth

In the process of frost formation and densification, water vapor from the air flow is transferred to the frost layer. Some of the water vapor deposits on the frost surface to make the frost layer thicker while the rest of the water vapor moves into the frost layer which result in the frost layer become denser. This phenomenon can be express mathematically as

$$\dot{m}_{v,fst} = \delta_{fst}\left(\frac{d\rho_{fst}}{dt}\right) + \rho_{fst}\left(\frac{d\delta_{fst}}{dt}\right) \tag{2.7}$$

The first term on the right hand side of Equation (2.7) refers to the densification rate of the frost layer while the second term is the frost growth rate.

Most of the previous works were based on experiments for a variety of simple geometry such as cylindrical, flat plate and parallel plate. From a general overview of the literatures, the major factors affecting the frost growth are:

a) Temperature of heat transfer surface

b) Humidity of moist air stream

c) Air velocity (or Reynolds Number)

d) Location along heat exchanger surface

From the literature, investigators agree on the first two factors mentioned above. Frost growth increases with a decrease in temperature of the heat transfer surface and with an increase in humidity of the air flowing across the surface.

However, as for the effect of air velocity, there is no conclusive evidence. Schneider (1978), Yonko and Sepsy (1967) and Brian et al. (1969) did not find that the air velocity had any effect on frost growth. In contrast, Yamakawa et al. (1972), Schulte and Howell (1982), Cheng and Wu (2003) showed data where Reynolds number (or air velocity) has influence on frost growth. O'Neal and Tree (1984) found that there was a critical Reynolds number of about 15900, above which the Reynolds number had no effect on frost growth but below which there was a strong dependence on Reynolds number. Data from other investigators such as Yamakawa et al. (1972) suggested that there is a critical Reynolds number above which the velocity has no effect. This critical number appears to lie between 12000 and 18000. These observations did not agree with other investigators such as Abdel-Wahed et al. (1984) and Lee and Ro (2001). Abdel-Wahed et al. (1984) took their data for the range of Reynolds number from 3000 to 140000 while Lee and Ro (2001) range from 10430 to 18200, but both results showed no sign of critical Reynolds number.

Another potential factor that influences frost growth is the location on the heat exchanger surface. Hayashi et al. (1977), Abdel-Wahed et al. (1984), Schulte and Howell (1982), Mao et al. (1992) and Cheng and Shiu (2002) found that the frost layer grows faster in the upstream than in the downstream of the plate. O'Neal and Tree (1984) observed that, for low flow rate, his results agreed with Hayashi's results but for higher flow rates, he observed no significant variation in thickness. Luer and Beer (2000) also observed that at higher Reynolds numbers, the frost layer is almost homogeneous, with the leading edge thickness remaining near constant and the downstream height increasing.

2.2.1 Modeling of Frost growth

Parish and Sepsy (1972) presented a numerical, finite difference formulation to study the frosting process under forced convection. Their method was based on a finite difference scheme with boundary layer momentum, energy and mass balance. The model allows for frost properties to be functions of the frost surface temperature. Chuang (1976) presented a simple mathematical model based on basic heat and mass transfer to study the frost formation process. His model accounts for humidity, air temperature, plate temperature and frost surface temperature. However, he assumed that the density of the frost was a constant.

Jones and Parker (1975) attempted to quantify the frost formation process via the use of molecular diffusion of the water vapor at the frost surface using energy and mass balances. They incorporated the humidity, plate surface temperature, porosity, mass diffusion of water vapor, density and thermal conductivity into their model. When compared with experimental results, it had an accuracy of about 30 %. To solve for the growth rate and densification rate of frost layer, the initial condition for the frost thickness and density are needed. They validated their model by varying the initial conditions for the frost thickness and density and found that the frost thickness could be very small (~ 2 x 10^{-5} m) without causing problem in the numerical solutions. The initial value of density, from their studies, should be kept smaller value than expected. As long as the initial frost thickness and density are given sufficiently small value, they will not affect the solution for the frost growth and densification.

White and Creamers (1981) suggested that the total mass of water vapor which diffuses into the frost layer approximately half of it goes to increase frost density and the other half goes to increase thickness of the frost layer. They found their hypothesis to be in good agreement with previously reported experimental results. Therefore, this hypothesis was useful in developing an analytical model for frost formation and growth. This concept has been used by other investigators in the course of their modeling attempts.

Sherif et al. (1993) presented simple method for modeling the average properties of frost in different geometries. They used the Brian correlation (1970) for thermal conductivity of the frost layer and Hayashi et al. (1977) correlation for the density. The numerical solution shows the model under predicting Yonko and Sepsy (1967) and Jones and Parker (1975) data with maximum 30% error.

Tao and Besant (1993) presented a physical model with coupled heat and moisture diffusion within the frost layer modeled as a porous media. Le Gall et al. (1997) modified that model by modifying the effective diffusion coefficient of water vapor using a continuous function. However, their models focused on water vapor diffusion in a frost layer rather than the growth rate itself. Na and Webb (2004) stated that the air is supersaturated at the frost surface and their model predicted the mass transfer rate with maximum 25 % error.

While many research efforts have proposed different models of frost growth, only Sherif et al. (1993) and Le Gall et al. (1997) proposed model to account for the

frost characteristic of partial melting and refreezing that occurs when the frost surface reaches 0 ^{o}C, which is known as permeation process. During this period, the frost layer undergoes a cycle of thinning and densification due to the melting and subsequent formation on an icy sub layer at the top of the deposit. This will result in structural changes in the frost layer that tends to increase both the frost density and thermal conductivity with time. Sherif et al. (1993) proposed a model which includes a constant value of mass ratio of frost melted to total frost deposited. According to their assumption, the constant value is between zero to 1 and this value can only be determined using experimental data. They did not provide further explanation on the changes in frost height during this process and the boundary condition changes arising from this. Le Gall et al. (1997) introduced a variable, volumetric fraction, for the water mass redistribution to the underlying frost layer. Their model, however, requires further study and validation by experiments.

2.3 Finned-Tube Heat Exchanger

As mentioned in section 2.2, the water vapor from air is transferred to the frost layer for growth and densification. The humidity of the air flow through the evaporator decreases along the flow direction due to the mass transfer to the fin surface. This phenomenon causes non-uniform frost thickness on the fins. The complex surface geometry of the heat exchanger, thermodynamic properties of refrigerant flow in the tubes and the thermodynamic properties of humid air complicate the matter further. In view of this, the problem becomes very complex and a complete general model is difficult to be formulated.

The available literature is limited and mainly focuses on measuring the performance of heat exchanger under frosting condition. That includes Stoecker (1957, 1960), Gatchilov and Ivanova (1979), Gates et al. (1967), Neiderer (1976), Kondepudi and O'Neal (1988, 1989, 1990, 1991), Ameen (1993), Yan et al. (2003) and Deng et al. (2003). From these studies the following conclusion can be drawn:

a. The growth of frost restricts air flow in the heat exchanger and also insulates the heat exchanger surface. The overall heat transfer coefficient decreases as the frost continues to grow.
b. The pressure drop across the heat exchanger increases with frost and is the most important factor affecting the heat exchanger performance.
c. The heat transfer coefficient for lower fin density coil was higher than high fin density coil after a period of frosting. Neiderer (1976) and Gatchilov and Ivanova (1979) pointed out that coils with variable fin spacing performs better than those with constant fin spacing.
d. Pressure drop across the coil and frost growth rate is higher when the air relative humidity is high and the coil surface temperature is low.
e. A lower refrigerant temperature increases the amount of frosting.

For the effect of air velocity on frosting rate, Gatchilov and Ivanova (1979), Kondepudi and O'Neal (1989) and Rite and Crawford (1991) agreed that as the air velocity increases, the frosting rate increases. The operating condition for Kondepudi and O'Neal (1989) were -10 ^{o}C refrigerant temperature, 80 % RH, 0 ^{o}C air temperature and air velocity of 0.66 m/s (130 fpm) and 1.62 m/s (200 fpm). With

an increase of 53 % in air velocity, the frost mass accumulated increased by 28 %. They explained that higher air velocity leads to a higher heat and mass transfer coefficient, thereby increasing the amount of moisture being converted to frost in the same time period. Senshu et al. (1990) and Yan et al. (2003) have opposite observation. Senshu et al. (1990) explicated that the mean temperature of fin increased as the air velocity increased which leaded to lower frosting rate. Yan et al. (2003) further explained that the surface temperature become colder as the air velocity decreased. Lower temperature tends to increase the frosting rate. Sanders' (1972) results agree initially, but as the velocity is further increased, the frosting rate decreases.

In the category of air temperature, Tantakitti and Howell (1986) and Rite and Crawford (1991b) found that increasing the air temperature increases the frosting rate but Sanders (1974) showed that the frost thickness was less at higher air temperature. Yan et al. (2003) in their experiment observed both phenomenons as shown in Fig. 2.3. It was a two rows coil operated at refrigerant temperature of -15 ^{o}C, 70 % RH and air volumetric flow 24 m^3/min for three different air temperatures. Higher air temperature has higher humidity ratio for the same relative humidity. Higher air temperature also means higher heat transfer rate which will increase the heat exchanger's surface temperature. In their experiment, when the air temperature increased from 2.5 ^{o}C to 5 ^{o}C with other parameters remains constant, the frost growth increased. This indicates that the effect of humidity ratio is dominant. However, the frost growth decreased when the air temperature increased from 5 ^{o}C to 7.5 ^{o}C. In this case, the effect of surface temperature is dominant.

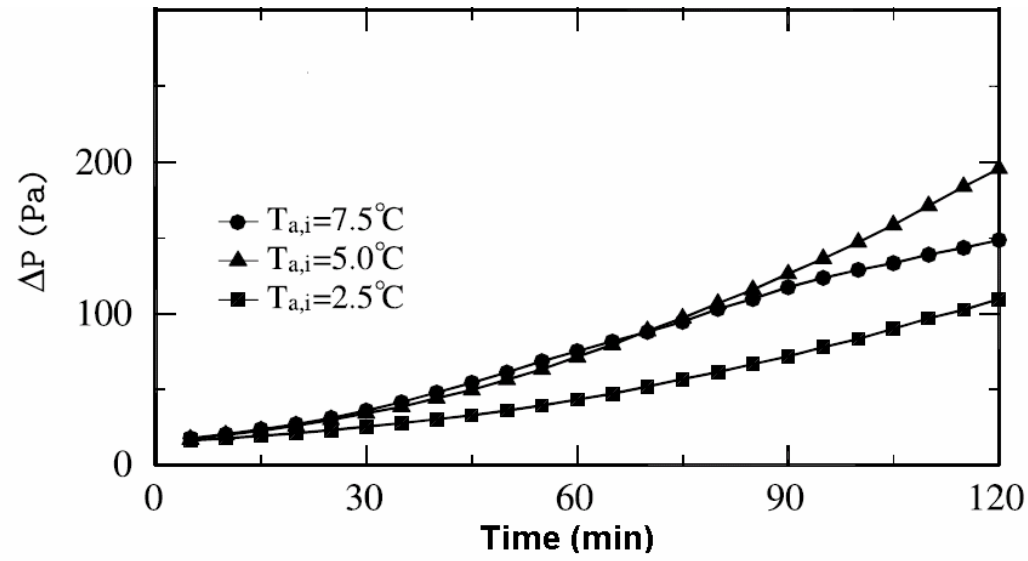

Figure 2.3: ***Effect of air temperature on air pressure drop under frost condition. (Yao et al. (2003))***

Ogawa et al. (1993) conducted series of tests to observe frost formation and investigated the performance of heat exchangers. The types of fins studied are shown in Fig. 2.4. Type-1, Type-2, Type-3 and Type-4 were used to investigate the effect of staging. Type-1 had front staging, Type-2 had front staging and side staging and Type-3 had only side staging. Type-4 had part of large fins cut and bent vertically in the air flow direction to guide fresh air in the side staging into the heat exchanger.

The Type-5, Type-6, Type-7, Type-8 and Type-9 were used to investigate the effect of fin width extension and partial cutting of fins. Type-5 was a basic type; Type-6 was extended along the leading edge with 1.5 times the fin width of Type-5 while Type-7 was 2 times the fin width of Type-5. The fin widths of Type-8 and

Type-9 were the same as that of Type-6 with partial cutting of fins between the tubes as shown in Figure 2.4.

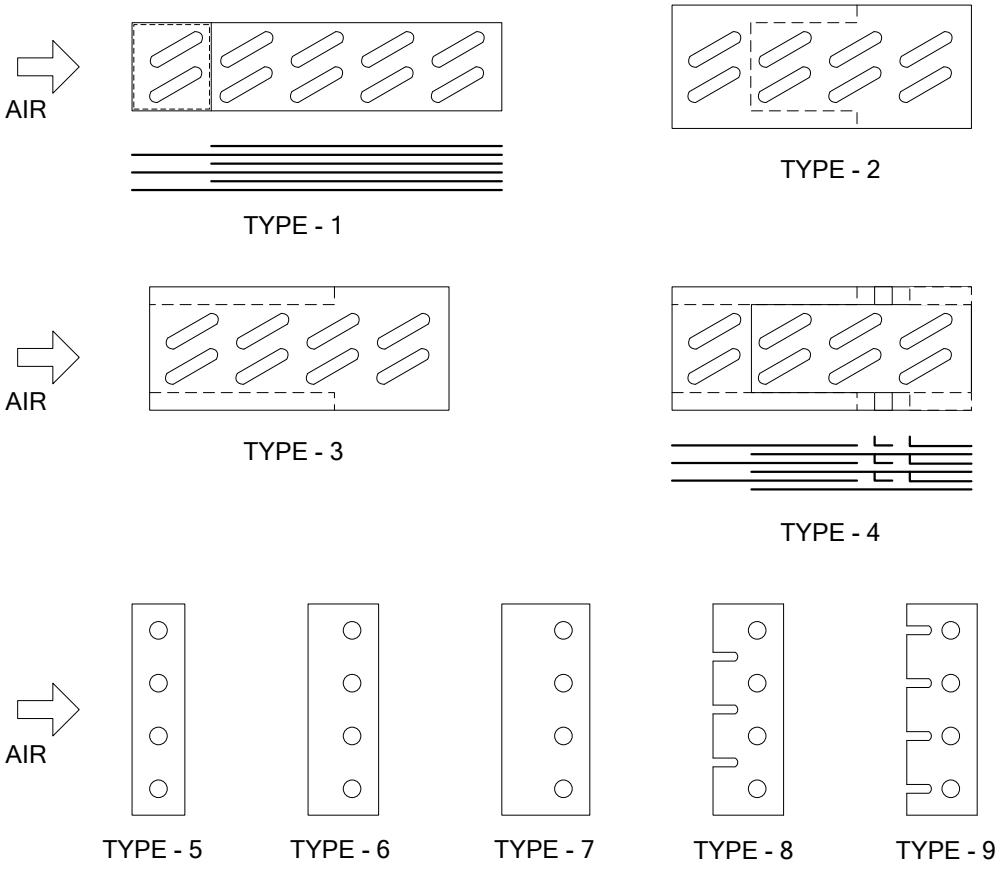

Figure 2.4: ***Fin configuration studied by Ogawa et al. (1993)***

Their observations indicated that frost should partly decreases at the leading edge of fins to reduce air pressure drop. They found that staging and partial cutting of fins to allow air bypass is effective in decreasing air pressure drop and increasing the heat transfer rate. Their results showed that staging, fin width extension and partial cutting of fins are all very effective in improving heat exchanger performance.

Based on their test results, the following conclusions can be highlighted:

a. Front staging reduced air flow blockage at the leading edge of fins of heat exchangers and reduced air pressure loss. The sample type with fin staging indicated an 8 % larger heat transfer rate and a 30 % smaller pressure loss coefficient as compared with the sample without fin staging.

b. Side staging has advantageous because part of the fresh air can be guided to the rear of the heat exchanger and promotes heat transfer there. There was a difference of 25 % heat transfer rate when the frost accumulation was 0.14 kg/m^3.

c. Fin width extension was effective in improving performance under frosting conditions. Because the fin surface temperature around the leading edge was increased by fin width extension, frost accumulation was reduced at the leading edge and air flow blockage was decreased. Although the heat transfer rate for heat exchanger with width extension was smaller than that without width extension, the rate of decrease was much less when the frost accumulation quantity was large.

d. The effect of partial cutting of fins was similar to the effect of staging. The frost accumulation was localized around the tubes by partial cutting of fins and the increase of the total air pressure loss was suppressed because the air pressure loss by the tubes was not dominant. It was desirable to provide partial cutting of fins just in front of the tubes.

Waters et al. (2001a, 2001b) studied the effect of fin staging on performance of heat pump. Their results showed that widening of first row increases cycle time

and cyclic COP but narrowing of back row reduces the benefit in COP compared to the base case, while increasing the benefit in frost/defrost time. They also pointed out that longer frosting times result in more frost accumulation on the evaporator fins, which takes more time and energy expenditure to melt. This trade-off results in marginal improvements in cyclic COP and overall system performance.

Kondepudi and O'Neal (1989a, 1989b, 1990, 1991) conducted experiments on different fin configurations on the performance of fin-tube heat exchanger. Flat, wavy, louver and corrugated type were used. The following results were observed:

a. Coils with louvered fins have more frost accumulation than other fin types. This can be attributed to the increased surface area of contact for the mass transfer to occur and frost to settle down. The other three fin types were very close together, ostensibly because of similar geometries.
b. Coils with louvered fins have the greatest pressure drop.
c. Enthalpy drop across coil was more on those with higher fin density. Higher humidity also leaded to a greater enthalpy drop because of the increasing latent energy being transferred. However, the enthalpy drops for the higher humidity begun to slowly decline with time whereas the lower humidity was quite constant. The louvered fin type has the greatest enthalpy drop due to both higher sensible and latent energy transfers than the other three types.
d. Heat exchanger effectiveness increased with an increased in humidity. Increased in face velocity decreased the effectiveness. The louvered fin type has the highest effectiveness when compared to the other three.

Tassou and Marquand (1987) and Ameen (1993) studied the overall performance of heat pump under frosting condition. The mass of frost accumulated on the evaporator increases with air relative humidity. As frosting commences, the heat extracted from the air by evaporator is reduced, resulting in a decrease in refrigerant temperature, yielding a decrease in refrigerant density at the compressor inlet and leading to reduction in both refrigerant flow rate and compressor power. The heating capacity and COP of the heat pump increased initially but later showed a gradual drop due to the insulating effect and drop in air flow. Air mass flow rate also decreases caused by increased resistance of the passage due to frosting. This also affects the fan power consumption which is directly proportional to the air mass flow. Payne (1994) performed an experiment to investigate the insulating effects of frost on heat pump system by controlling air flow. He found that the heating capacity remained within 5 % of its peak value but cycle times were increased by as much as 43 % when keeping the air flow through the outdoor heat exchanger was kept constant. His research showed that the drop in air flow due to the presence of frost on the fins was the primary factor in reducing the capacity and COP of the heat pump system.

Aoki et al. (1991) presented their experimental results on heat exchangers consisted of four rows. They used brine/coolant as the working refrigerant. They reported that the frost layer depended on cold surface temperature and the air water vapor concentration. For parallel flow, which means that both the air and coolant flow the same direction from 1st row to 4th row, the frost thickness was thicker at first

row than the forth row as shown in Fig. 2.5. In the counter flow, where the coolant flow from the 4th row to the 1st row, both the cold surface temperature and water vapor concentration difference decreased along the direction of the air flow. The frost thickness at forth row, which the coolant inlet, was thicker as compare to first row but the difference was not as great as compare to parallel flow configuration. In both cases, at the row where the coolant inlet was, thicker frost was observed as compared to other rows.

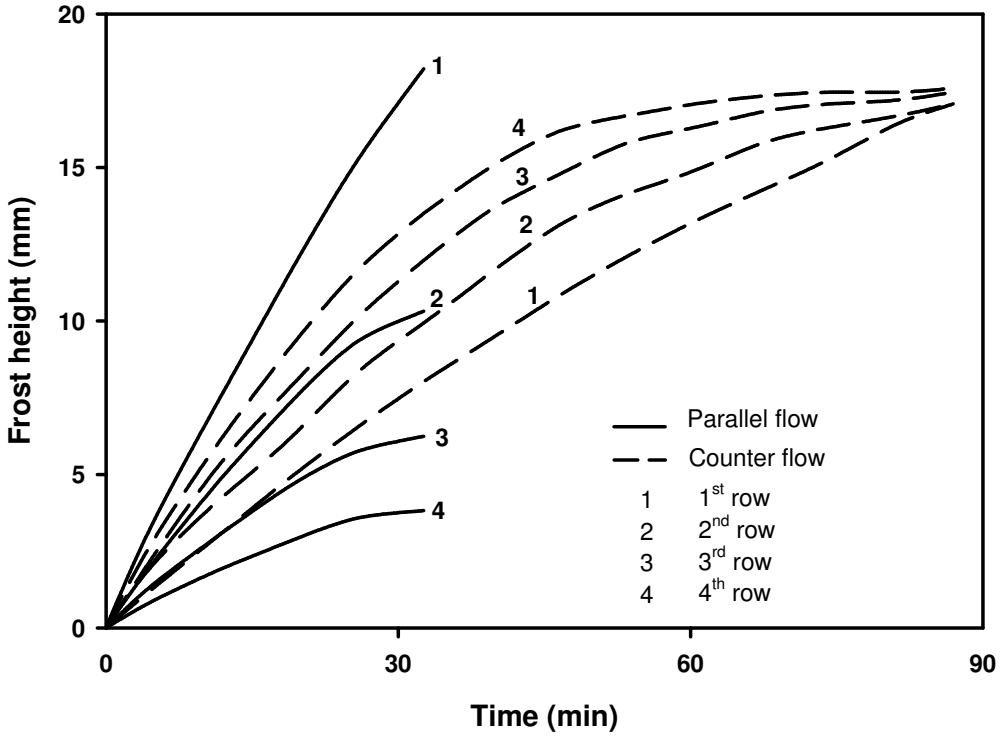

Figure 2.5: ***Comparison for frost thickness on each row between parallel and counter flow types. (Aoki et al. (1991))***

The literature pertaining to the theoretical models for predicting the growth rate of frost layer is very limited. Oskarsson et al. (1990) proposed a model for

evaporator operating with dry, wet and frosted surface. Their model used mostly empirical correlations to predict the air side, refrigerant side and frost properties. Yasuda et al. (1990) in their simulation model included refrigeration cycle simulator, frost formation simulator and fan characteristic simulator. They assumed the refrigeration cycle to be in steady state condition, frost density and thickness has no influence on the air heat transfer coefficient. These assumptions oversimplify their model.

Kondepudi and O'Neal (1993a) proposed a model assuming a homogeneous distribution of frost on the entire heat exchanger and modeled the overall frost growth mechanism. Their experiment used glycol/water mixture as working refrigerant. They model did not include the variation of wall temperature and frost along the heat exchanger. Their prediction is within 15 % to 25 %, as compared to the experimental results. Seker et al. (2004a) also presented a similar model with homogeneous distribution of frost on entire heat exchanger. The effect of coil depth was not taken into consideration. They assumed that the property of air, wall temperature and refrigerant temperature were the same inside the coil. These assumptions cannot be applied to a practical heat exchanger. In validating their model, they compared their model with their experimental data (Sekar et al. 2004b) in terms of overall heat transfer coefficient and air pressure drop across the coil. Their experimental results shows similar trend as predicted but the difference between the experimental and prediction were more than 50 %.

Martinez-Fais and Aceves (1999) incorporated a frost model in a steady state heat pump model. Their frost model was developed by using a combination of first principles and empirical correlations. Their results were only compared with frost results for parallel plates.

Chen et al. (2000a, 2000b) modeled the frost characteristics on heat exchanger fins with physical model that couples heat and moisture diffusion within the frost layer. They found that for a constant air flow rate through the heat exchanger fins, the blockage of air flow resulting from the frost growth increases the pressure drop across the fin by up to a factor of 8 times while the heat transfer rate decreases by as much as 20 %. They compared the mathematical model results with experimental data for frost height, density and heat transfer rate through the cold base and found that they agreed within the experimental uncertainty. Their results, however, only limited to the studies on heat exchanger fin only and not the practical finned tube heat exchanger.

Modeling of finned tube evaporator in the refrigeration system uses volatile refrigerant as a cooling medium to cool the air is complicated as compared to single-phase fluid such as brine or glycol/water concentration. Because of the two-phase evaporating flow inside coils, the local heat transfer coefficient varies in a great range at different locations. This varying local heat transfer coefficient results in an uneven air temperature distribution off the evaporator. To fully simulate the heat transfer processes, air temperature and other parameter distributions inside the coil, the distributed parameter models have gained popularity. However, one of the key

problems in these models is the description of void fraction and two-phase flow. MacArthur (1984) ignored the momentum exchange between liquid and vapor in the two-phase flow region; the momentum equation was omitted. Wang and Touber (1991) used a simplified void propagation equation to describe the liquid and vapor mass transport phenomena occurring in the two-phase region. In their analysis, the evaporating temperature was assumed constant in the two-phase region when integrating the energy equation. In Nyers and Stoyan's model (1994), the two-phase evaporating flow was assumed to be homogeneous and the evaporator was simplified to be a bundle of parallel pipes with the cross flow of air, which is not the case for most of refrigeration evaporators in refrigeration systems. Jia et al. (1995) presented a distributed model that is applicable for the serpentine coil type evaporators. However, the two-phase evaporating flow inside the tube was simplified as homogeneous flow. Their model, however, did not include the frost model.

Yao et al. (2004) presented a distributed model with homogeneous distribution of frost on fins and tube. There are some typography errors in the models and equations were inconsistent from which they referred to. For example the equation for frost accumulation rate in their equation (2) and air side heat transfer coefficient in their equation (29) as quoted below:

$$m_{fst} = m_a\left(\omega_{a,in} - \omega_{a,out}\right) = \frac{d}{dt}\left(\delta_{fst}\rho_{fst}\right) = \rho_{fst}\frac{d\delta_{fst}}{dt} + \delta_{fst}\frac{d\rho_{fst}}{dt}$$

[kg/s] [kg/s] [kg/m^2 s] [kg/m^2 s] [kg/m^2 s]

$U_o = \frac{m_a j}{A_{\min} Sc^{2/3}}$, where j is Colburn j factor and Sc is Schmidt Number

[W/m^2 K] [kg/m^2 s]

The units were inconsistent in both equations. As for the equations for airside pressure drop and fin efficiency were different from the paper which they referred to. For example in their equation (32) the friction coefficient as quoted below:

$f = 0.129\left(\frac{m_a D_o}{A_{\min}\mu_a}\right)^{-0.227}$, whereas the from their quoted reference

$f = 0.589\left(\frac{A_o}{A_t}\right)^{-0.28}(\mathrm{Re})^{-0.27}$

The simulated results for the frost distribution for their counter flow configuration was different as reported by Aoki et al. (1991). Their results showed that the frost at the refrigerant outlet was thicker than the refrigerant inlet row. The reason for this disagreement is uncertain.

2.4 Conclusions

There are several major conclusions that can be drawn from the above literature survey.

1. Frost growth is generally detrimental to heat transfer in heat exchangers.
2. The literature available on finned-tube heat exchanger is limited. It has been agreed that frost formation and growth deteriorate their performance.

3. Frost growth increases with increasing of humidity and decreasing of heat transfer surface temperature.
4. The overall heat transfer coefficient decreases due to the increase in thermal resistance of frost layer.
5. The overall heat transfer increases with the relative humidity of the air flowing across the coils.
6. Heat exchangers with wider fin spacing perform better as comparing with narrow fin spacing under frosting condition. Variable fin spacing or fin staging seems to perform better.
7. The pressure drop across the coils has an effect on the heat transfer performance of the coils.
8. There is still a need for an improved correlation for the air side heat transfer coefficient in the presence of frost for multiple row finned-tube heat exchangers.
9. Most information regarding frosting in finned-tube heat exchanger is experimental in nature. A satisfactory mathematical model to simulate the process with two-phase refrigerant flow flowing through coil and the variation of frost growth along the coil is required.

CHAPTER 3
Mathematical Models

Modeling frost growth using the fundamental heat and mass transfer relationships is a complicated process. The heat transfer from the air to the frost surface and from the frost surface to the heat exchanger surface must be taken into account. There is also mass transfer from the air streams to the frost surface and water vapor diffusion into the frost layer. On the refrigerant side, it is a two-phase flow which vapor and liquid phase changes along the coil. The growth of frost depends on the cold surface temperature and absolute humidity difference between the air and the cold surface. Due to the variation of wall temperature and absolute humidity along the coil, the frost growth on the coil is non-homogeneous.

Figure 3.1 shows the thermal resistance for finned tube evaporator under frosting condition. It is clear that the refrigerant thermal property inside the tube, the frost thermal property and air condition outside the tube are inter-related. Therefore, in order to present a simplified but practical mathematical model, certain assumptions have to be introduced.

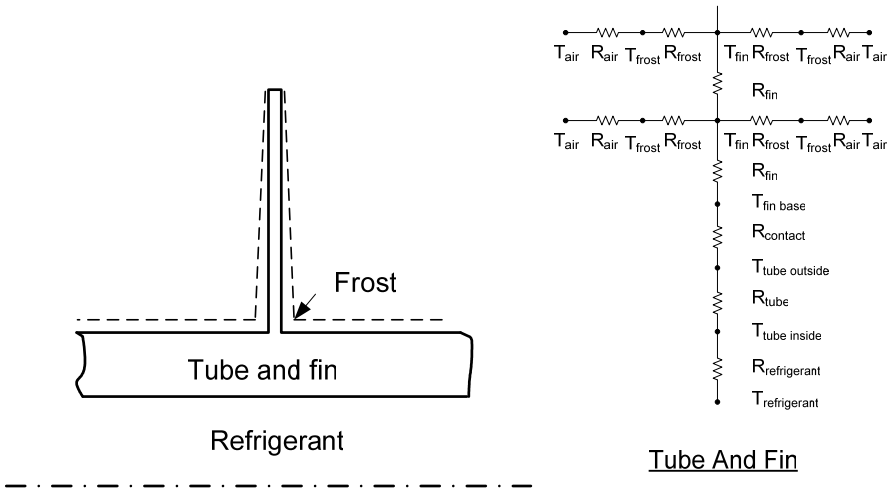

Figure 3.1: ***Thermal resistance for evaporator under frosting condition***

The type of evaporator coil circuit configuration for this study is shown in Figure 3.2. The refrigerant is distributed via a distributor into the first row of the coil and collects into a header at the last row. This type of coil circuit is used in Carrier refrigeration unit. The mathematical model, however, does not limited to this type of configuration. Because the model is purely distributed, it is applicable to various kinds of tube circuit arrangements of evaporator.

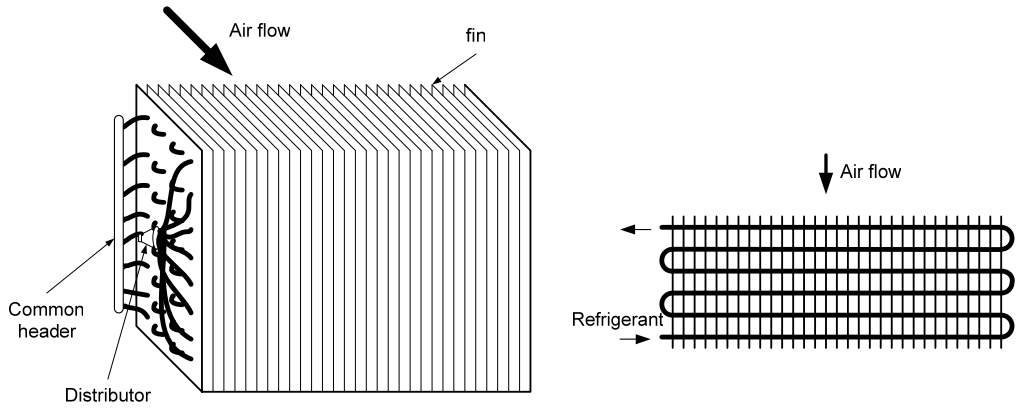

a) Pictorial view ***b) Top view***

Figure 3.2*: Schematic representation of evaporator*

3.1 Assumptions

The following assumptions are made in the model development:

1. The refrigerant mass flow rate in each circuit is considered uniform, and there is no heat conduction between circuits so that the evaporator is simplified as one circuit.
2. The two-phase evaporating flow inside the tube is simplified as a one-dimensional drift flux flow. The vapor and liquid flow are incompressible and in thermal equilibrium conditions.
3. The axial heat conduction within the tube wall is ignored, as transverse conduction along the fins will be dominant.
4. Frost formation process is assumed to be quasi-steady state.
5. The frost density at any instant is average value of a layer.
6. The amount of water vapor absorbed into the frost layer is proportional to water vapor density in the frost.

The governing equations for the heat and mass transport processes are derived using local averaging techniques for mass, momentum and energy transport. Figure 3.3 shows the configuration of the evaporator and frost for mathematical model.

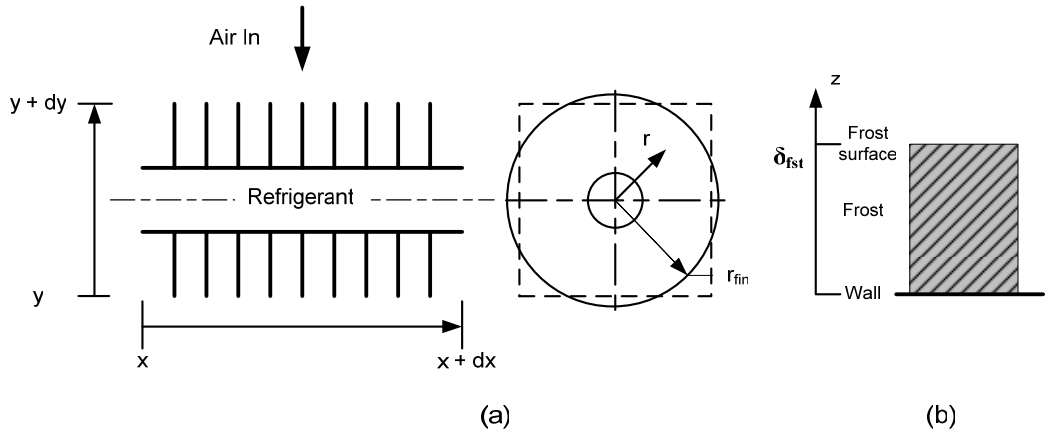

x is the distance in refrigerant flow direction

y is the distance in air flow direction

z is the distance perpendicular to cold surface

r_{fin} is the radial distance along fin

Figure 3.3: ***The configuration of evaporator and frost growth model***

3.2 Governing Equations for Refrigeration Side

3.2.1 Continuity equation

The continuity equation is derived from the mass conservation equation

Rate of mass in = Rate of mass out - Rate of mass accumulation

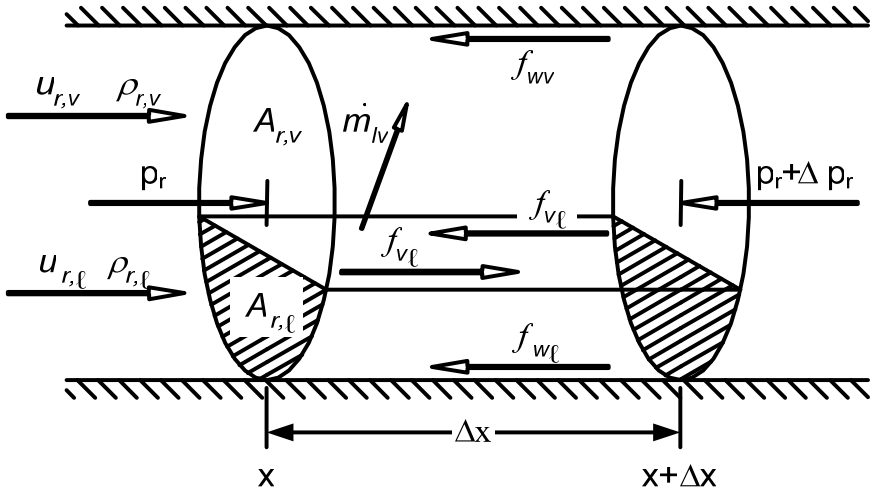

Figure 3.4: ***The control volume for the two-phase flow***

Consider a volume element between two sections x and (x + Δx) as illustrated in Figure 3.4. For the vapor phase,

$$(A_{r,v}\rho_{r,v}u_{r,v})_x + \dot{m}_{lv}.A_i.\Delta x = (A_{r,v}\rho_{r,v}u_{r,v})_{x+\Delta x} + (\frac{\partial \rho_{r,v}}{\partial t})A_{r,v}.\Delta x\,, \tag{3.1}$$

$$\frac{(\alpha\rho_{r,v}u_{r,v})_{x+\Delta x} - (\alpha\rho_{r,v}u_{r,v})_x}{\Delta x} + \alpha(\frac{\partial \rho_{r,v}}{\partial t}) = \dot{m}_{lv}\,, \tag{3.2}$$

where the void fraction, $\alpha = \frac{A_{r,v}}{A_i}, (1-\alpha) = \frac{A_{r,\ell}}{A_i}$.

Taking the limit of equation (3.2) as Δx approaches zero,

$$\frac{\partial}{\partial t}(\alpha\rho_{r,v}) + \frac{\partial}{\partial x}(\alpha\rho_{r,v}u_{r,v}) = \dot{m}_{lv}\,. \tag{3.3}$$

Similarly, for the liquid phase,

$$\frac{\partial}{\partial t}[(1-\alpha)\rho_{r,\ell}] + \frac{\partial}{\partial x}[(1-\alpha)\rho_{r,\ell}u_{r,\ell}] = -\dot{m}_{lv}\,. \tag{3.4}$$

The mixed density of the flow is $\tilde{\rho}_r = \alpha\rho_{r,v} + (1-\alpha)\rho_{r,\ell}$, (3.5)

and the average velocity of the vapor-liquid mixture is $u_r = \frac{G_r}{\tilde{\rho}_r}$. (3.6)

mass flux for vapor and liquid phase,

$$\chi G_r = \alpha\rho_{r,v}u_{r,v}, \tag{3.7}$$

$$(1-\chi)G_r = (1-\alpha)\rho_{r,\ell}u_{r,\ell} \tag{3.8}$$

where χ is the refrigerant vapor quality.

Equation (3.7) and (3.8) yield

$$\alpha = \frac{1}{1+S\frac{\rho_{r,v}}{\rho_{r,\ell}}\frac{1-\chi}{\chi}}, \tag{3.9}$$

where S is slip ratio.

Equations (3.3) and (3.4) yield:

$$\frac{\partial}{\partial t}[\alpha\rho_{r,v} + (1-\alpha)\rho_{r,\ell}] + \frac{\partial}{\partial x}[\alpha\rho_{r,v}u_{r,v} + (1-\alpha)\rho_{r,\ell}u_{r,\ell}] = 0. \tag{3.10}$$

Utilizing equations (3.5), (3.6), (3.7) and (3.8), the final form of the continuity equation can be written as:

$$\frac{\partial\tilde{\rho}_r}{\partial t} + \frac{\partial}{\partial x}(\tilde{\rho}_r u_r) = 0. \tag{3.11}$$

The calculation of the slip ratio, S, in equation (3.9) depends on the model selected. Below are some correlations that are commonly used:

(i) Homogeneous: In the homogeneous model, the two-phase flow is treated as a pseudo-fluid with average properties, therefore the slip ratio S is unity.

(ii) Smith's correlation: Smith (1970) suggested the following correlation to calculate the slip ratio based upon a simple physic model of stratified flow:

$$S = K + (1-K)\sqrt{(\frac{\rho_{r,\ell}}{\rho_{r,v}} + K\frac{1-\chi}{\chi})/(1+K\frac{1-\chi}{\chi})}\,, \tag{3.12}$$

where K is the entrainment factor and may be calculated by K= -1.09 + 0.11596 ln F

Here, F is the total mass flux ($lb_m\ ft^{-2}\ h^{-1}$)

(iii) Chilshom's correlation: Chilshom (1973) considered the relation between friction and void fraction and developed a correlation to calculate the slip ratio as follows:

$$S = \sqrt{1-\chi(1-\frac{\rho_{r,\ell}}{\rho_{r,v}})}\,. \tag{3.13}$$

(iii) CISE correlation: Premoli et al. (1971) proposed an empirical correlation for determining the slip ratio

$$S = 1 + E_1(\frac{\overline{y}}{1+\overline{y}E_2} - \overline{y}E_2)\,, \tag{3.14}$$

where

$$\overline{y} = \frac{\zeta}{\zeta - 1},\ \zeta = \frac{1}{1 + \frac{1-\chi}{\chi}\frac{\rho_{r,v}}{\rho_{r,\ell}}},$$

$$E_1 = 1.578\,Re_{r,\ell}^{-0.19}\left(\frac{\rho_{r,\ell}}{\rho_{r,v}}\right)^{0.22},$$

$$E_2 = 0.0273\,We_{r,\ell}\,Re_{r,\ell}^{-0.51}\left(\frac{\rho_{r,\ell}}{\rho_{r,v}}\right)^{-0.08},$$

$$Re_{r,\ell} = \frac{G_r D}{\mu_{r,\ell}},$$

$$We_{r,\ell} = \frac{G_r^{\,2} D}{\rho_{r,\ell}\sigma},$$

where $\rho_{r,v}$ and $\rho_{r,\ell}$ are the vapor and the liquid densities,

G_r is the total refrigerant mass flux,

D is the tube diameter,

$\mu_{r,\ell}$ is the refrigerant liquid viscosity,

σ is the surface tension.

3.2.2 Momentum equation

The momentum equation is based on Newton's second law of motion:

Rate of momentum out of element	-	*Rate of momentum into element*	+	*Rate of momentum accumulated within element*	=	*Sum of external forces acting on element*

Consider the volume element in Figure 3.4. For the vapor phase, the momentum equation is expressed as

$$\frac{(\alpha\rho_{r,v}u_{r,v}^2)_{x+\Delta x}-(\alpha\rho_{r,v}u_{r,v}^2)_x}{\Delta x}+\frac{\partial}{\partial t}(\alpha\rho_{r,v}u_{r,v})=-\alpha\frac{\Delta p_r}{\Delta x}-f_{v\ell}-f_{wv}, \tag{3.15}$$

where $\alpha=\frac{A_{r,v}}{A_i},(1-\alpha)=\frac{A_{r,\ell}}{A_i}$.

Taking the limit of equation (3.15) as Δx approaches zero yields

$$\frac{\partial}{\partial t}(\alpha\rho_{r,v}u_{r,v})+\frac{\partial}{\partial x}(\alpha\rho_{r,v}u_{r,v}^2)=-\alpha\frac{\partial p_r}{\partial x}-f_{v\ell}-f_{wv}. \tag{3.16}$$

Similarly, for the liquid phase,

$$\frac{\partial}{\partial t}[(1-\alpha)\rho_{r,\ell}u_{r,\ell}]+\frac{\partial}{\partial x}[(1-\alpha)\rho_{r,\ell}u_{r,\ell}^2]=-(1-\alpha)\frac{\partial p_r}{\partial x}+f_{v\ell}-f_{w\ell}. \tag{3.17}$$

Equations (3.16) and (3.17) yield:

$$\frac{\partial}{\partial t}[\alpha\rho_{r,v}u_{r,v}+(1-\alpha)\rho_{r,\ell}u_{r,\ell}]+\frac{\partial}{\partial x}[\alpha\rho_{r,v}u_{r,v}^2+(1-\alpha)\rho_{r,\ell}u_{r,\ell}^2]=-\frac{\partial p_r}{\partial x}-f_{wv}-f_{w\ell}. \tag{3.18}$$

Let $f_x = f_{wv} + f_{w\ell}$ as the friction pressure loss, equation (3.18) is rewritten as

$$\frac{\partial}{\partial t}(\tilde{\rho}_r u_r) + \frac{\partial}{\partial x}[\alpha\rho_{r,v}u_{r,v}^2 + (1-\alpha)\rho_{r,\ell}u_{r,\ell}^2] = -\frac{\partial p_r}{\partial x} - f_x . \tag{3.19}$$

Utilizing equations (3.5), (3.6), (3.7) and (3.8), final momentum equation can be written as:

$$\frac{\partial}{\partial t}(\tilde{\rho}_r u_r) + \frac{\partial}{\partial x}(\beta\tilde{\rho}_r u_r^2) = -\frac{\partial p_r}{\partial x} - f_x , \tag{3.20}$$

$$\text{where } \beta = \chi^2[1+\frac{\rho_{r,\ell}(1-\alpha)}{\alpha\rho_{r,v}}] + (1-\chi)^2[1+\frac{\alpha\rho_{r,v}}{(1-\alpha)\rho_{r,\ell}}]. \tag{3.21}$$

Friction pressure loss f_x of a two-phase flow in equation (3.20) can be calculated using Hewitt (1990) method:

$$f_x = \phi_\ell^2(-\frac{dp_r}{dx})_\ell . \tag{3.22}$$

The friction multiplier ϕ_ℓ is calculated as follows:

a) For the viscosity ratio, $\frac{\mu_{r,\ell}}{\mu_{r,v}} < 1000$, Friedel correlation is used (Hewitt 1990)

$$\phi_{\ell 0}^2 = E + \frac{3.23FH}{Fr^{0.045}We^{0.035}} . \tag{3.23}$$

b) For the viscosity ratio, $\frac{\mu_{r,\ell}}{\mu_{r,v}} > 1000$, Chisholm correlation is used (Hewitt 1990)

$$\phi_{\ell 0}^2 = 1 + (Y^2 - 1)[B\chi^{(2-n)/2}(1-\chi)^{(2-n)/2} + \chi^{2-n}], \tag{3.24}$$

where

$$E = (1-\chi)^2 + \chi^2 \frac{\rho_{r,\ell} f_{v0}}{\rho_{r,v} f_{\ell 0}} ,$$

$$\begin{cases} \mathrm{Re}_{r,v0} = \dfrac{G_r D}{\mu_{r,v}}, & \text{for } \mathrm{Re}_{r,v0} < 2000,\ f_{v0} = \dfrac{16}{\mathrm{Re}_{r,v0}} \\ & \text{for } \mathrm{Re}_{r,v0} > 2000, f_{v0} = 0.079\,\mathrm{Re}_{r,v0}^{-1/4} \\ \mathrm{Re}_{r,\ell 0} = \dfrac{G_r D}{\mu_{r,\ell}}, & \text{for } \mathrm{Re}_{r,\ell 0} < 2000,\ f_{\ell 0} = \dfrac{16}{\mathrm{Re}_{r,\ell 0}} \\ & \text{for } \mathrm{Re}_{r,\ell 0} > 2000, f_{\ell 0} = 0.079\,\mathrm{Re}_{r,\ell 0}^{-1/4} \end{cases}$$

$$F = \chi^{0.78}(1-\chi)^{0.224},$$

$$H = \left(\frac{\rho_{r,\ell}}{\rho_{r,v}}\right)^{0.91} \left(\frac{\mu_{r,v}}{\mu_{r,\ell}}\right)^{0.19} \left(1-\frac{\mu_{r,v}}{\mu_{r,\ell}}\right)^{0.7},$$

$$\mathrm{Fr} = \frac{G_r^2}{gD\rho_H^2}, \quad \text{homogeneous density}, \rho_H = \frac{\rho_{r,v}\rho_{r,\ell}}{\chi\rho_{r,\ell} + (1-\chi)\rho_{r,v}},$$

$$\mathrm{We} = \frac{G_r{}^2 D}{\rho_H \sigma},$$

n = power of the friction factor/Reynolds number relationship, n = 0.25.

$$Y^2 = \frac{(dp_r/dx)_{v0}}{(dp_r/dx)_{\ell 0}}, \qquad \begin{cases} (dp_r/dx)_{v0} = 2 f_{v0} G_r{}^2/D\rho_{r,v} \\ (dp_r/dx)_{\ell 0} = 2 f_{\ell 0} G_r{}^2/D\rho_{r,\ell} \end{cases}$$

$$B = \begin{cases} 55/G_r^{0.5} & 0 < Y < 9.5;\ G_r \geq 1900\ \text{kg/m}^2\ \text{s} \\ 2400/G_r & 0 < Y < 9.5;\ 500 < G_r < 1900\ \text{kg/m}^2\ \text{s} \\ 4.8 & 0 < Y < 9.5;\ G_r < 500\ \text{kg/m}^2\ \text{s} \\ 520/(YG_r^{0.5}) & 9.5 < Y < 28;\ G_r \leq 600\ \text{kg/m}^2\ \text{s} \\ 21/Y & 9.5 < Y < 28;\ G_r > 600\ \text{kg/m}^2\ \text{s} \\ 15000/(Y^2G_r^{0.5}) & 28 < Y. \end{cases}$$

3.2.3 Energy equation

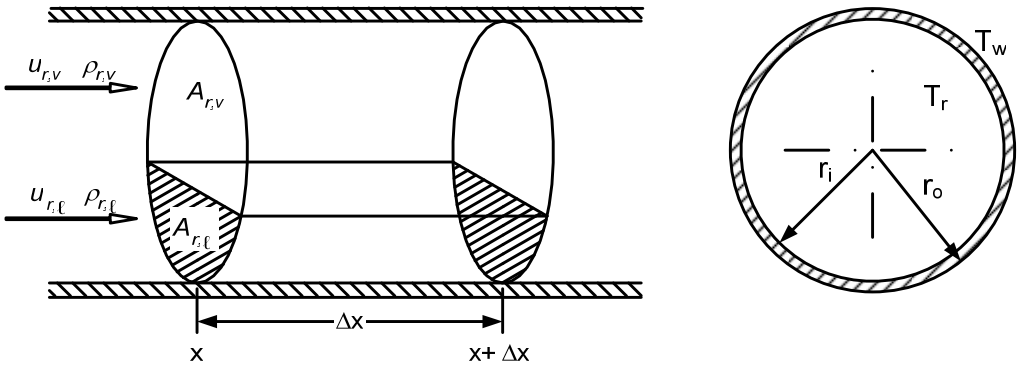

Figure 3.5*: Control volume for derive energy equation.*

The energy conservation equation applied to the control volume in Figure 3.5 is expressed as follows

Energy into element	-	*Energy out of element*	+	*Energy generated inside element*	=	*Energy stored in element*

The energy into the element, including internal energy of flow in and heat transferred through wall, is

$$E_{IN} = 2\pi r_o.\Delta x.\dot{q}_{tr}, \tag{3.25}$$

where $\dot{q}_{tr} = U_{t,r}(T_w - T_r)$ is the rate of heat transfer per unit area of tube wall to refrigerant and the heat transfer coefficient from tube to refrigerant is

$$U_{t,r} = \frac{1}{\frac{1}{U_r}\frac{A_o}{A_i} + \frac{\delta_w}{k_w}\frac{A_o}{A_{mean}}}.$$

The energy out of the element is

$$E_{OUT} = \left[(\rho_{r,v}u_{r,v}A_{r,v}h_{r,v}) + (\rho_{r,\ell}u_{r,\ell}A_{r,\ell}h_{r,\ell})\right]_{x+\Delta x}, \tag{3.26}$$

where h is the enthalpy of the refrigerant.

The energy stored in the element is

$$E_{STO} = \rho_{r,v}\frac{\partial h_{r,v}}{\partial t}.A_{r,v}.\Delta x + \rho_{r,\ell}\frac{\partial h_{r,\ell}}{\partial t}.A_{r,\ell}.\Delta x. \tag{3.27}$$

Therefore, the energy equation is written in the form of

$$2\pi r_o.\Delta x.\dot{q}_{tr} - \left[(\rho_{r,v}u_{r,v}A_{r,v}h_{r,v}) + (\rho_{r,\ell}u_{r,\ell}A_{r,\ell}h_{r,\ell})\right]_{x+\Delta x} = \frac{\partial}{\partial t}(\rho_{r,v}h_{r,v}A_{r,v} + \rho_{r,\ell}h_{r,\ell}A_{r,\ell})\Delta x. \tag{3.28}$$

Taking the limit of (3.28) as Δx approaches zero, $\alpha = \frac{A_{r,v}}{A_i}, (1-\alpha) = \frac{A_{r,\ell}}{A_i}$,

$$\frac{2\pi r_o}{A_i}\dot{q}_{tr} - \frac{\partial}{\partial x}\left[(\alpha\rho_{r,v}u_{r,v}h_{r,v}) + (1-\alpha)\rho_{r,\ell}u_{r,\ell}h_{r,\ell}\right] = \frac{\partial}{\partial t}[\alpha\rho_{r,v}h_{r,v} + (1-\alpha)\rho_{r,\ell}h_{r,\ell}]. \quad (3.29)$$

Rearranging the equation,

$$\frac{\partial}{\partial t}[\alpha\rho_{r,v}h_{r,v} + (1-\alpha)\rho_{r,\ell}h_{r,\ell}] + \frac{\partial}{\partial x}[\alpha\rho_{r,v}u_{r,v}h_{r,v} + (1-\alpha)\rho_{r,\ell}u_{r,\ell}h_{r,\ell}] = \frac{2\pi r_o}{A_i}\dot{q}_{tr} . \quad (3.30)$$

By definition,

$$\tilde{h}_r = \alpha\rho_{r,v}h_{r,v} + (1-\alpha)\rho_{r,\ell}h_{r,\ell}, \quad (3.31)$$

$$h_r = \chi h_{r,v} + (1-\chi)h_{r,\ell}. \quad (3.32)$$

Substituting (3.5), (3.6), (3.7), (3.8), (3.25) and (3.26) in (3.24) yield

$$\frac{\partial \tilde{h}_r}{\partial t} + \frac{\partial}{\partial x}(h_r\tilde{\rho}_r u_r) = \frac{2r_o}{r_i^2}U_{t,r}(T_{w,o} - T_r). \quad (3.33)$$

The evaporation heat transfer coefficient, U_r is calculated from Wongwises et al. (2000) as follows:

For two-phase,

$$U_r = \frac{2.4704}{X_{tt}^{0.6394}}U_{r,\ell}, \quad (3.34)$$

where X_{tt} is the Lockhart-Martinelli parameter and defined by

$$X_{tt} = \left(\frac{1-\chi}{\chi}\right)^{0.9}\left(\frac{\rho_{r,v}}{\rho_{r,\ell}}\right)^{0.5}\left(\frac{\mu_{r,\ell}}{\mu_{r,v}}\right)^{0.1},$$

$$U_{r,\ell}=0.023Re_{r,\ell}^{0.8}Pr_{r,\ell}^{0.4}(k_{r,\ell}/D)\ .$$

For single-phase,

$$U_{r}=0.023Re_{r,v}^{0.8}Pr_{r,v}^{0.4}(k_{r,v}/D)\ . \tag{3.35}$$

3.3 Governing Equation for Tube Wall Side

The tube wall of the heat exchanger consists of the bare tube and rectangular fins. The rectangular fin is converted into an equivalent circular fin of the same thickness and the same area as shown in Fig. 3.6. This approach is used by researchers such as Stocker and Jones (1982), Mago and Sherif (2002) and Hoffenbecker (2004).

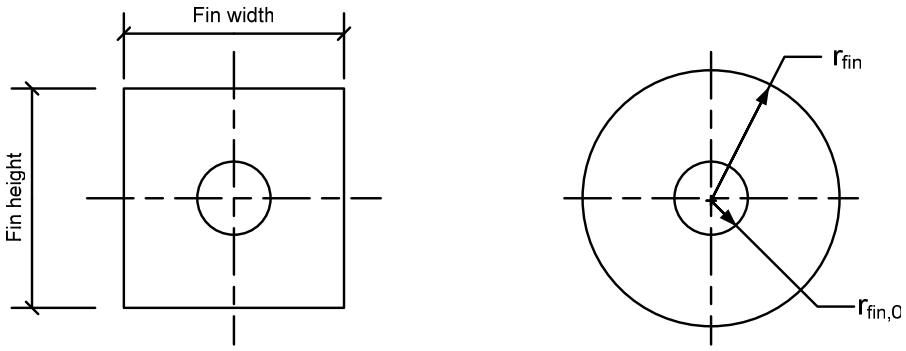

Figure 3.6: ***Converting a rectangle plate fin (a) into an equivalent circular (b)***

The outer radius of the circular fin is determined as

$$r_{fin}=\sqrt{\frac{\text{fin width x fin height}}{\pi}} \tag{3.36}$$

The governing equation for the tube wall side can be written as follows:

Energy stored = Energy in - Energy out

$$c_{p,w} M_w \frac{\partial T_w}{\partial t} = q_t + q_{fin} - U_{t,r} A_{i,t} (T_w - T_r), \tag{3.37}$$

where c_{pw} is the specific heat of tube and fin.

M_w is the mass of tube and fin per meter

The heat transfer rate per meter to tube, q_t, is

$$q_t = \frac{U_o A_{o,t}}{c_{p,a}} (h_a - h_w), \tag{3.38}$$

and when the wall temperature falls below freezing point, frost will form onto the surface of wall. The heat transfer rate to wall will be heat conducted through frost layer. The expression will now become:

$$q_t = k_{fst} \frac{\partial T_{fst}}{\partial z} A_{o,t}. \tag{3.39}$$

The heat transfer rate within the fin can be determined from

$$\rho_{fin} c_{p,fin} \frac{\partial T_{fin}}{\partial t} = k_{fin} \left(\frac{1}{r_{fin}} \frac{\partial}{\partial r_{fin}} \left(r_{fin} \frac{\partial T_{fin}}{\partial r_{fin}} \right) \right) + H, \tag{3.40}$$

where the heat source, H, is

$$H = \frac{2}{\delta_{fin}} \frac{U_o}{c_{p,a}} (h_a - h_{fin}), \tag{3.41}$$

where U_o is the air side heat transfer coefficient

and for condition when frost present on the fin surface, the heat source will be the heat conducted through frost layer

$$H = \frac{2}{\delta_{fin}} k_{fst} \frac{\partial T_{fst}}{\partial z}. \tag{3.42}$$

where k_{fst} is the thermal conductivity of frost

δ_{fin} is the fin thickness.

Wang and Chi (2000) correlated the air side heat transfer coefficients, U_o, from a total of 74 test cores. The proposed heat transfer correlation can predict 88.6% of the test points within ± 15%, with a mean deviation of 7.51%. The correlation is as follows:

$$j_a = 0.108\, Re_{D_c}^{-0.29} \left(\frac{X_t}{X_l}\right)^{b_1} \left(\frac{S_{fin}}{D_c}\right)^{-1.084} \left(\frac{S_{fin}}{D_h}\right)^{-0.786} \left(\frac{S_{fin}}{X_t}\right)^{b_2} \text{ for } N_r = 1 \tag{3.43}$$

where

$b_1 = 1.9 - 0.23 \ln (Re)$

$b_2 = -0.236 + 0.126 \ln (Re)$

$$j_a = 0.086\, Re_{D_c}^{c_1} N_r^{c_2} \left(\frac{S_{fin}}{D_c}\right)^{c_3} \left(\frac{S_{fin}}{D_h}\right)^{c_4} \left(\frac{S_{fin}}{X_t}\right)^{-0.93} \text{ for } N_r \geq 2, \tag{3.44}$$

where

$$c_1 = -0.361 - \frac{0.042 N_r}{\ln Re_{D_c}} + 0.158 \ln\left[N_r \left(\frac{S_{fin}}{D_c} \right)^{0.41} \right],$$

$$c_2 = -1.224 - \frac{0.076 \left(\frac{X_l}{D_h} \right)^{1.42}}{\ln Re_{D_c}},$$

$$c_3 = -0.083 + \frac{0.058 N_r}{\ln Re_{D_c}},$$

$$c_4 = -5.735 + 1.21 \ln \frac{Re_{D_c}}{N_r}.$$

S_{fin} is the fin spacing, D_c is the collar diameter of fin, X_l and X_t are the longitudinal and transverse tube pitch and N_r is the number of rows.

Colburn transfer factor, j_a, is

$$j_a = \frac{Nu}{Re\, Pr^{1/3}}, \tag{3.45}$$

3.4 Governing Equation for Air Side

3.4.1 Energy balance on air side

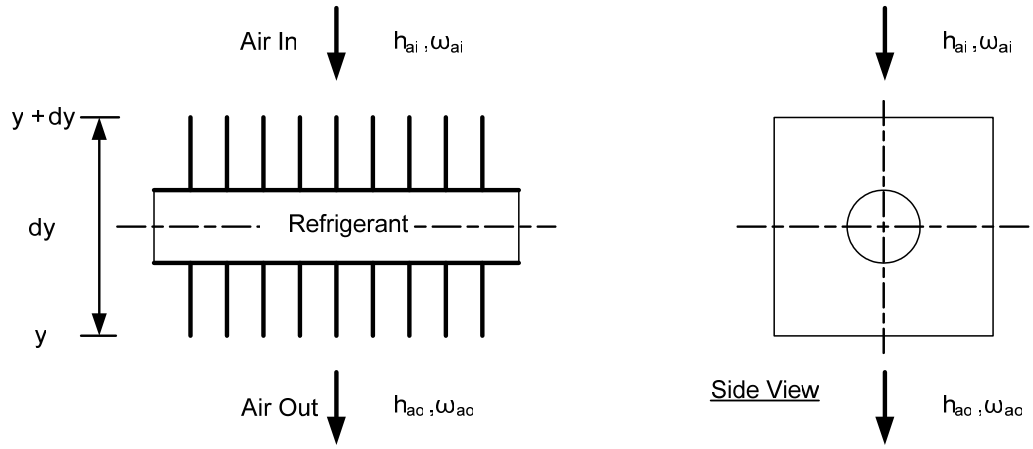

Figure 3.7*: Control volume along a tube with fins*

The energy transfer is the function of the enthalpy driving force between the air and tube wall and can be written as:

For condition without frost

$$\frac{m_a dh_a}{dy} = \frac{U_o A_o}{c_{p,a}}(h_a - h_w), \tag{3.46}$$

and for condition when frost is present on the wall surface, the energy transfer equation can be written as.

$$\frac{m_a dh_a}{dy} = \frac{U_o A_o}{c_{p,a}}(h_a - h_{fst,s}). \tag{3.47}$$

where $h_{fst,s}$ is the enthalpy of saturated air at frost surface.

3.4.2 Mass balance on air side

The variation of air absolute humidity along the air flow direction is the function of humidity difference between the air and wall and can be written as follows:

$$\frac{m_a d\omega_a}{dy} = U_m A_o (\omega_a - \omega_w), \tag{3.48}$$

and for condition with frost, the equation can be written as:

$$\frac{m_a d\omega_a}{dy} = U_m A_o (\omega_a - \omega_{fst,s}). \tag{3.49}$$

where $\omega_{fst,s}$ is the absolute humidity of air at frost surface and U_m is the mass transfer coefficient. This value of mass transfer coefficient is determined using the Lewis correlation (ASHRAE 2001)

$$U_m = \frac{U_o}{c_{p,a} Le^{2/3}}, \tag{3.50}$$

where, Le is the Lewis number. Lewis relation, where Le is closed to unity, is nearly true for air and water vapor at low mass transfer rates. The agreement between wet-bulb temperature and adiabatic saturation temperature is a direct consequence of the nearness of the Lewis number to unity for air and water vapor.

For the condition of frost, Lee et al. (2003) correlated their experimental results postulated the Lewis number as 0.905 ± 0.005. They predicted the behavior of frost formation within 10% error. Therefore, this correlation is adopted for the present numerical calculation.

The thermodynamic properties of moist air are taken from ASHRAE (2001).

3.4.3 Pressure drop across coil

Wang et al. (2000) correlated the friction factor, f, from a total of 74 test cores. The proposed friction factor correlation can predict 85.1% of the test cores within ± 15%, with a mean deviation of 8.31%. The friction factor was correlated based on the pressure drop equation proposed by Kays and London (1984).

$$\Delta P_a = \frac{G_{max}^2}{2\rho_{a,i}}\left[f\left(\frac{A_{t,f}}{A_{free}}\right) + \left(1+\sigma^2\right)\left(\frac{\rho_{a,i}}{\rho_{a,o}} - 1\right)\right], \tag{3.51}$$

The proposed friction factor from Wang et al. (2000) study is

$$f = 0.0267\,Re_{D_c}^{c_5}\left(\frac{X_t}{X_l}\right)^{c_6}\left(\frac{S_{fin}}{D_h}\right)^{c_7}, \tag{3.52}$$

where

$$c_5 = -0.764 + 0.739\left(\frac{X_t}{X_l}\right) + 0.177\left(\frac{S_{fin}}{D_c}\right) - \frac{0.00758}{N_r},$$

$$c_6 = -15.689 + \frac{64.021}{\ln Re_{D_c}},$$

$$c_7 = 1.696 - \frac{15.695}{\ln Re_{D_c}}.$$

The above friction factor is only valid for the condition without frost. When frost forms and grows on the surface of the finned tube heat exchanger, the free flow area will decrease. The variation of the free flow area with time is determined by considering the additional blockage resulting from the growth of the frost layer. Since the actual spacing between fins changes with the frost growth, thereby reducing the free flow area, this is incorporated into the model.

3.5 Governing Equation for Frost Growth

The physical model of frost layer growth is presented by utilizing the conservation equation of continuity, energy and mass diffusion of the frost-air boundary layer in a quasi-steady state approach. The iterative quasi-steady state approach adopted is used to compute the frost-air interface temperature, frost properties, the partial pressure of water vapor in the vicinity of the frost surface and the frost thickness.

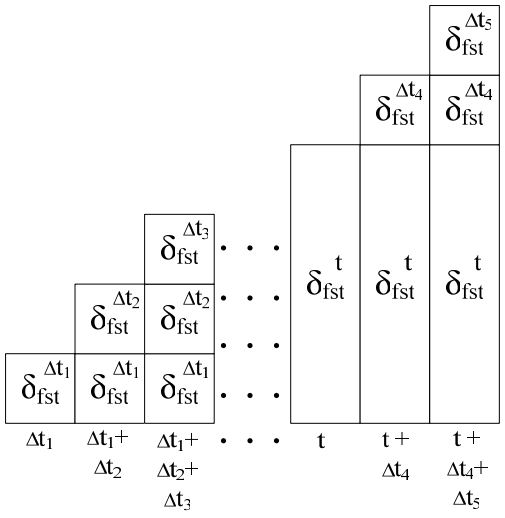

Figure 3.8: ***Schematic diagram for increment of frost thickness with time***

The iterative quasi-steady state can be described using the diagram shown in Fig. 3.8. For a given instant of time, t, the properties of the air stream across the heat exchanger and that of the frost layer are assumed to be constants. As such, it is possible to calculate the local rate of frost formation based on the resultant mass diffusion rates at that instant time of t. The calculated frost thickness of δ_{fst}^{t} and other frost properties will be recorded and stored. The solution proceeds with certain boundary and previous stored conditions, calls upon appropriate subroutines that provide solution to the boundary layer equations at a given instant of time t + Δt, calculates the rates of frost growth, and computes the new frost thickness $\delta_{fst}^{t} + \Delta\delta_{fst}^{\Delta t_1}$ and other frost properties. A forward progress in time results in the recalculation of these quantities based on the previous time steps.

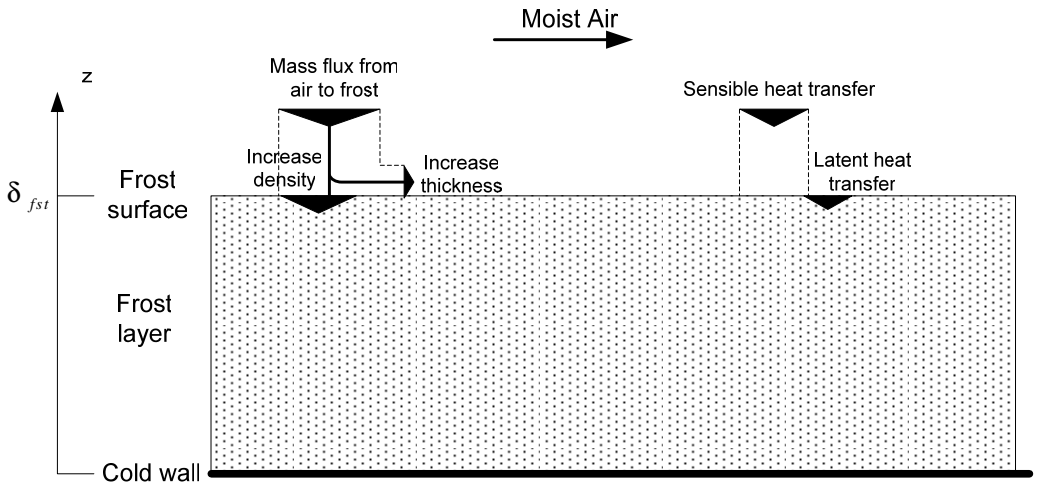

Figure 3.9: ***Combined heat and mass transfer during frost formation***

Figure 3.9 shows the physical model of the frost layer growth. Sensible heat is transferred from the air to the frost surface by temperature difference between the air stream and frost surface. Water vapor from the air is also transferred to the frost layer by concentration difference driving force. Some of the water vapor transferred becomes frost and deposit on the frost layer, causing the frost layer to grow. The remaining is diffused into the frost layer, causing the frost density to increase. The latent heat of sublimation caused by phase change of the water vapor is transferred through the frost layer by conduction. The mathematical formulations of model are explained in the following sections.

3.5.1 Mass transfer in the frost layer

The rate of mass transfer for deposition of frost can be expressed as the loss of humidity in the air as the water vapor is transferred to the cold surface of heat exchanger. The equation can be written as:

$$\dot{m}_v = U_m(\omega_a - \omega_{fst,s}), \tag{3.53}$$

where $\omega_{fst,s}$ is the absolute humidity at the frost surface.

The exit humidity is a function of the heat and mass transfer processes which occurred and are dealt with in the next section/row on the heat exchanger.

It is known that as the frost forms, it will continue to grow. As it grows, not only it increases in height, it also increase in density. Therefore, it can be assumed that the water vapor transferred to the frost, portion of it contributes to increase frost density and the rest to increases the frost height. The mass transfer from the air to the frost for this phenomenon can be expressed as

$$\dot{m}_v = \dot{m}_\delta + \dot{m}_\rho, \tag{3.54}$$

where $\dot{m}_\delta$ is the frost height component and

$\dot{m}_\rho$ is the density component.

The water vapor passes through the frost layer by diffusion and subsequently changes into ice by phase change. The densification rate is strongly related to the water vapor diffusion within the frost layer. The amount of water-vapor absorbed into the frost layer through diffusion and increase in density can be mathematically expressed as follows:

$$\dot{m}_\rho = D_{v,eff} \frac{d\rho}{dz} \tag{3.55}$$

The diffusion coefficient, D_v, is a function of temperature, pressure and composition. Sherwood and Pigford (ASHRAE Fundamentals, 2001) proposed an empirical equation for the diffusion coefficient of water vapor in the air up to 1100^{o}C as follows:

$$D_v = \frac{9.238E\text{-}7}{P_a}\left(\frac{T_a^{2.5}}{T_a + 245}\right) \tag{3.56}$$

where P_a is the atmospheric pressure (kPa)

The above equation for diffusion coefficient is only applicable to free air condition. The water vapor diffusion inside the frost should be smaller than that in the free air stream because of the increased path length in the frost layer. The frost layer is a porous structure of air and ice and therefore, the diffusion path is longer than that in free space. To account for these effects, the effective diffusion, $D_{v,eff}$, can be expressed as follows:

$$D_{v,eff} = \tau \varepsilon_{fst} D_v \tag{3.57}$$

where τ is the tortuosity factor

ε_{fst} is the porosity of frost layer is given by $\varepsilon_{fst} = \frac{\rho_{ice} - \rho_{fst}}{\rho_{ice} - \rho_a}$

The tortuosity factor is a measure of the mean free path of the water vapor molecules in the frost layer as compared to that in free space (without obstructions). There were several expressions to account for the tortuous diffusion path in porous media. Brian et al. (1969) used a fixed bed of glass particles and found the value of tortuosity factor was in the range from 0.769 to 0.909. They used the value of 0.909 in their study of water vapor diffusion in a frost layer. Jones and Parker (1975) and Samy and Duong (1989) adopted the same value as Brian et al. (1969) in their study.

Sanders (Kondepudi, 1988) used the following empirical equation in his research for frost formation and was also used by Kondepudi (1988):

$$\tau = 1 - \left(\frac{\rho_{fst}}{\rho_{ice}} \right)^{0.5} \tag{3.58}$$

The tortuosity factor is dependent on the shape of the particles of which the porous layer consists. The shape of the particles and arrangement of the porous structure must be known to calculate the exact tortuosity value. The precise value of the tortuosity of the porous media may be unknown for a frost layer. For this study, Sanders's expression is used.

The water vapor diffuses through the frost layer is absorbed into the frost layer. It is assumed that the amount of water vapor absorbed into the control volume is proportional to the water vapor density in the control volume. The water vapor diffusion equation in the frost layer can be written as follow:

$$D_{v,eff} \frac{d^2 \rho_v}{dz^2} = \Phi_{fst} \rho_v , \tag{3.59}$$

where Φ_{fst} is an absorption factor and can be determined by applying boundary condition which will be shown in initial and boundary conditions section.

The complete expression for the amount of water vapor diffusing into the frost layer has been developed. The quasi-steady state expression for increase of

frost height and frost density with time, the frost height component in Eq. (3.54) can be written as follows:

$$\dot{m}_{\delta} = \rho_{fst}\left(\frac{d\delta_{fst}}{dt}\right), \tag{3.60}$$

$$\dot{m}_{\rho} = \delta_{fst}\left(\frac{d\rho_{fst}}{dt}\right). \tag{3.61}$$

For each time step, the changes of frost density and thickness are the increment value added to previous time step value as follows:

$$\rho_{fst,t+\Delta t} = \rho_{fst,t} + \frac{\dot{m}_{\rho}}{\delta_{fst}}\Delta t \tag{3.62}$$

$$\delta_{fst,t+\Delta t} = \delta_{fst,t} + \frac{\dot{m}_{\delta}}{\rho_{fst}}\Delta t \tag{3.63}$$

3.5.2 Heat transfer in the frost layer

The total heat flux at frost air interface is given by:

$$\dot{q}_{a,fst} = U_a(T_a - T_{fst,s}) + U_m h_{sg}(\omega_a - \omega_{fst,s}). \tag{3.64}$$

The first term on the right hand side is the sensible heat transfer from the air stream to the frost surface while the second term is the latent heat released during the mass

transfer process caused by phase change from air to frost for frost growth and densification.

Considering energy conservation in the control volume, the energy transfer mechanism is the heat transferred from the air conducted through frost layer and the latent heat transfer due to phase change from water vapor to frost crystal. This can be written as follows

$$k_{fst}\frac{d^2T_{fst}}{dz^2} = -\Phi_{fst}h_{sg}\rho_{a,v}\,. \tag{3.65}$$

The average thermal conductivity of frost layer has been investigated by many researchers. Dietenberger's (1983) semi-empirical correlation is chosen because the correlation can apply to a wide range of frost density and temperature, i.e., $\rho_{air} < \rho_{fst} < \rho_{ice}$ and $80\ K < T_w < 273\ K$. According to Dietenberger, the structure of the frost is a random mixture of ice cylinder and ice sphere at low frost density while at high frost density, the total structure of frost is a random mixture of air bubbles and ice layers. Through a complex semi-empirical derivation, the final set of equations for calculating the air-ice thermal conductivity of frost is given as follows:

$$k_{fst} = ¼\ ((3B_c - 1)k_l + (3\Theta_c - 1)k_u + \{[(3B-1)k_l + (3\Theta_c - 1)k_u]^2 + 8k_lk_u\}^{1/2}) \tag{3.66}$$

where

$$\Theta_c = 1 - B_c$$

B_c is the proportion of the frost volume representing ice spheres and ice planes.

$$B_c = 13.6\,(B_2 - B_1)(B - B_1)^2 x\left[1 - \frac{2}{3}\left(\frac{B - B_1}{B_3 - B_1} + \frac{B - B_1}{B_2 - B_1}\right) + \frac{(B - B_1)^2}{2(B_3 - B_1)(B_2 - B_1)}\right]$$

for $B > B_1$

$B_c = 0$ for $B \leq B_1$

B is the porosity of frost, defined by the equation

$$B = \frac{\rho_{ice} - \rho_{fst}}{\rho_{ice} - \rho_a}$$

where

$B_1 = 0.1726(T_{fst}/273.16)1$

$B_2 = 0.751$

$B_3 = B_2 + 0.3$

k_u in Eq. (3.66) is the upper limit conductivity expression for air bubbles and ice cylinder

$$k_u = (1 - B)\,k_b + Bk_c$$

k_b is the thermal conductivity of air bubbles given by

$$k_b = k_{ice}\left[1 - 2B\left(\frac{1 - a}{2 + a}\right)\right] \div \left[1 + B\left(\frac{1 - a}{2 + a}\right)\right]$$

$a = k_a / k_{ice}$

k_c is the thermal conductivity of ice cylinder given by

$$k_c = (1 - B)\, k_{ice} + B\, k_a$$

k_l in Eq. (3.60) is the lower limit of thermal conductivity expressed as follow

$$k_l = (1 - B)\, k_p + B\, k_s$$

where the thermal conductivity of ice spheres is given by

$$k_s = k_{ice}\left[3 + 2B(a - 1)\right] \div \left[3 - B\left(\frac{a-1}{a}\right)\right]$$

and ice planes by

$$k_p = \frac{k_{ice} k_a}{(1 - B)\, k_a + k_{ice} B}$$

3.6 Initial and boundary conditions

3.6.1 Refrigerant, tube wall and air side

The initial conditions for air and refrigerant are assumed to be in the steady state. In steady state, the time derivatives in Eqs. (3.11), (3.20), (3.33), (3.37) and (3.40) are set to zero. The solutions of the basic governing equations in the steady state are used as the initial conditions to the time-dependent system.

The boundary conditions for refrigerant, tube wall and air onto the coil are, for inlet refrigerant conditions,

$$m_{r,}(x = 0) = m_{r,in}, \qquad p_r\,(x = 0) = p_{r,in}, \qquad \alpha\,(x = 0) = \alpha_{in}, \tag{3.67}$$

$$T_{fin}\,(r_{fin} = 0) = T_w \qquad \frac{\partial T_{fin}}{\partial r_{fin}}(r_{fin} = r_{fin,o}) = 0$$

and for inlet air conditions,

$$m_a(y = 0) = m_{a,\,in}, \qquad T_a\,(y = 0) = T_{a,in}, \qquad \omega_a\,(y = 0) = \omega_{a,in}. \tag{3.68}$$

3.6.2 Frost layer side

The water vapor diffusion equation in Eq. (3.59) has two boundary conditions and they are,

$$\text{at } z = 0, \qquad \frac{d\rho_v}{dz} = 0,\ \rho_v = \rho_{v,sat}(T_w)$$
$$\text{at } z = \delta_{fst}, \qquad \rho_{v,fst,s} = \rho_{v,sat}(T_{fst,s}) \tag{3.69}$$

Solving Eq. (3.59) with conditions of Eqs. (3.69), the water vapor and absorption factor in the frost layer can be shown to be

$$\Phi_{fst} = D_{v,eff}\left[\frac{1}{\delta_{fst}}\cosh^{-1}\left\{\frac{\rho_{v,sat}\left(T_{fst,s}\right)}{\rho_{v,sat}\left(T_w\right)}\right\}\right]^2, \tag{3.70}$$

$$\rho_v(z) = \rho_{v,sat}(T_w)\cosh\varphi z, \tag{3.71}$$

where

$$\varphi = \sqrt{\frac{\Phi_{fst}}{D_{v,eff}}}. \tag{3.72}$$

The equation for total heat flux at frost air interface in Eq. (3.65) has two boundary conditions and are given by,

$$\begin{aligned} &\text{at } z = 0, && T = T_w \\ &\text{at } z = \delta_{fst}, && k_{fst}\frac{dT}{dz} = \dot{q}_a \end{aligned} \tag{3.73}$$

Solving Eq. (3.65) using conditions of Eqs. (3.73) will result in temperature distribution inside frost layer as

$$T(z) = \frac{\Phi_{fst}}{k_{fst}\varphi^2} h_{sg}\rho_{v,sat}(T_w)\left[z\varphi\sinh\varphi\delta_{fst} - \cosh\varphi z + 1\right] + \frac{\dot{q}_a z}{k_{fst}} + T_w. \tag{3.74}$$

The initial temperature can be taken as the cold surface temperature if the initial frost thickness is so thin that the heat transfer resistance of the initial frost thickness is negligible compared to the air side heat transfer resistance.

The initial frost height and density ideally should be as close to zero as possible since there is no frost initially. Jones and Parker (1975) tested the initial conditions by changing the values of the initial frost thickness and found that the initial thickness can approach zero (~ 2 x 10^{-5} m) without causing significant problems in predicting the frost growth rate. As for the density, they evaluate the effect of the initial value by changing the value from 8 to 48 kg/m^3. They found that the frost density and thickness converged to the same value. They concluded that as long as the initial value of the frost density is significantly smaller than the expected frost, it will not affect the solution for the frost growth and densification. The lowest possible initial frost height and frost density that would lead to a numerical stable and convergent solution was found to be 2 x 10^{-2} mm and 30 kg/m^3. Therefore, the initial conditions for the frost temperature, thickness and density in the present work are fixed as follows:

Temperature: $T_{fst} = T_w$

Thickness: $\delta_{fst} = 2 \times 10^{-2}$ mm

Density: 30 kg/m^3

3.7 Permeation phenomena

Continuous deposition of frost will result in a continuous increase in the frost thickness, surface temperature, density and thermal conductivity. As the frost continues to grow, the frost surface temperature will gradually increase due to the insulation effect or low thermal conductivity of frost. When the frost surface temperature reaches the melting point, the frost surface may melt and some liquid

water soaks towards the surface. This thinning and densification phenomenon due to melting and refreezing, known as permeation accounting for the changes in the vapor density at frost surface.

Sherif et al. (1993) proposed a way to account for this changes by introducing the following equation to calculate the new frost density after one cycle of melting and refreezing has occurred:

$$\rho_{fst,new} = \frac{\delta_{fst}\rho_{fst} + C_{melt}\Delta\delta_{fst}\rho_{ice} + (1-C_{melt})\Delta\delta_{fst}\rho_{fst}}{\delta_{fst} + \Delta\delta_{fst}}. \tag{3.75}$$

where C_{melt} is the mass ratio of frost melted to total frost deposited. According to their assumption, the constant value for C_{melt} is between zero to 1 and this value should be determined using experimental data. They did not provide further explanation on the changes in frost height during this process and the boundary condition changes from this.

Le Gall et al. (1997) presented a model based on a local volume averaging technique that allows the computation of temperature and density distributions throughout the entire frost layer. In their model, they divided the frost into a number of continuous non-overlapping control volumes. They stated that in order to take into account of this permeation phenomenon, the control volumes on top of the frost layer, when reaches the melting point, the corresponding water mass is redistributed to the underlying elements as shown in Fig. 3.10.

The ice fractions, ε_α (volume fraction of ice to control volume), of the control volumes concerned are corrected according to their available porosity until the liquid film is totally consumed. The correction is as follows:

$$\varepsilon_\alpha^{'} = \varepsilon_\alpha + \zeta(1-\varepsilon_\alpha), \varepsilon_\alpha^{'} \geq \varepsilon_\alpha \text{ and } 0 \leq \zeta \leq 1 \tag{3.76}$$

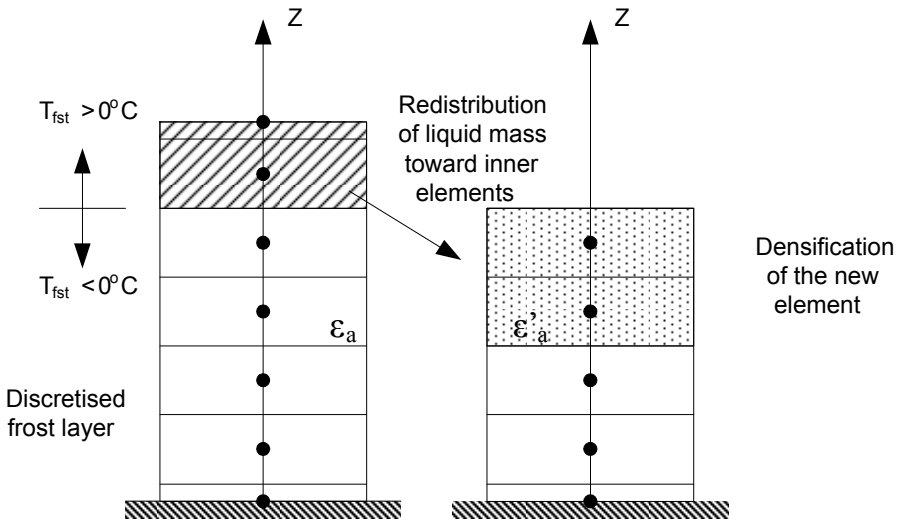

Figure 3.10: ***Schematic diagram for Le Gall et al. (1997) model to the permeation process***

The volumetric fraction, ζ, allows a choice between a more or less important infiltration depth for the liquid film. This technique is applicable to the frost analysis using local averaging technique.

This permeation process can be adopted in this mathematical modeling by assuming that the excess saturated vapor density is redistributed inside frost layer as shown in Fig. 3.11.

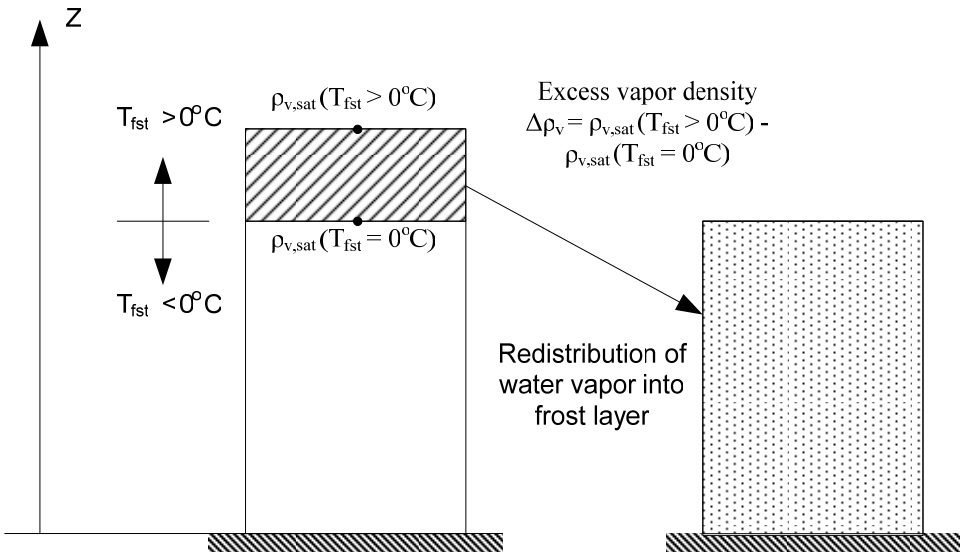

Figure 3.11: ***Schematic diagram for adaptation of frost model to the permeation process***

To account for this change, boundary condition for vapor density at frost surface in Eq. (3.69) is modified to

$$\rho_{v,fst,s} = (1 + E)\, \rho_{v,sat}(T_{fst,s}) \tag{3.77}$$

where E is the factor for excess vapor density due to melting. The excess vapor density $\Delta\rho_v = \rho_{v,fs}\ (T_{fst} > 0\ ^oC) - \rho_{v,sat}\ (T_{fst} = 0\ ^oC)$ is redistributed inside the frost layer. The value of E can be determined by being integrated into the frost model and iterated until the frost surface temperature is below the melting point.

3.8 Numerical Solution

The evaporator is assumed to be in the steady state initially, thus the steady-state initial conditions are applied. In the steady state, all terms associated with time derivative in the governing equations are eliminated, and the solution of the governing equations in the steady state will be used as the initial conditions of the dynamic system.

The coil is divided into a number of continuous non-overlapping cells as indicated by the indented lines shown in Fig. 3.12. The variables of the refrigerant and the tube, i.e., refrigerant vapor void fraction, refrigerant velocity, temperatures of refrigerant and wall are specified at the cell center, while the air temperature and humidity are specified at the cell walls, as displayed in Fig. 3.12 (b). For each cell, the 6 governing differential equations, i.e., Eqs. (3.11), (3.20), (3.33), (3.37), (3.46) and (3.48), for the above 6 variables, can be discretized into the finite difference forms as follows:

$$\frac{(\tilde{\rho}_r)_m^n-(\tilde{\rho}_r)_m^{n-1}}{\Delta t}+\frac{(\tilde{\rho}_r u_r)_m^n-(\tilde{\rho}_r u_r)_{m-1}^n}{\Delta x}=0 \tag{3.78}$$

$$\frac{(\tilde{\rho}_r u_r)_m^n-(\tilde{\rho}_r u_r)_m^{n-1}}{\Delta t}+\frac{(\beta\tilde{\rho}_r u_r^2)_m^n-(\beta\tilde{\rho}_r u_r^2)_{m-1}^n}{\Delta x}+\frac{(p_r)_m^n-(p_r)_{m-1}^n}{\Delta x}+(f_x)_m^n=0 \tag{3.79}$$

$$\frac{(\tilde{h}_r)_m^n-(\tilde{h}_r)_m^{n-1}}{\Delta t}+\frac{(h_r\tilde{\rho}_r u_r)_m^n-(h_r\tilde{\rho}_r u_r)_{m-1}^n}{\Delta x}-\frac{2r_o}{r_i}U_{t,r}[(T_{w,o})_m^n-(T_r)_m^n]=0 \tag{3.80}$$

$$c_{p,w}M_w\frac{(T_w)_m^n-(T_w)_m^{n-1}}{\Delta t}-\frac{U_o A_{o,t}}{c_{p,a}}[(h_a)_m^n-(h_w)_m^n]+U_{t,r}A_{i,t}[(T_w)_m^n-(T_r)_m^n]=0 \tag{3.81}$$

$$(h_a)_i^{j+1}-(h_a)_i^j-\frac{U_o A_o}{c_{p,a}m_a}[(h_a)_i^{j+1}-(h_w)_i^j]=0 \tag{3.82}$$

$$(\omega_a)_i^{j+1} - (\omega_a)_i^j - \frac{U_m A_o}{m_a}[(\omega_a)_i^{j+1} - (\omega_w)_i^j] = 0 \qquad (3.83)$$

where n is the time step, m is the cell number, i is the distance step in the refrigerant flow direction, and j is the distance step in the airflow direction and M_t is the total number of cells.

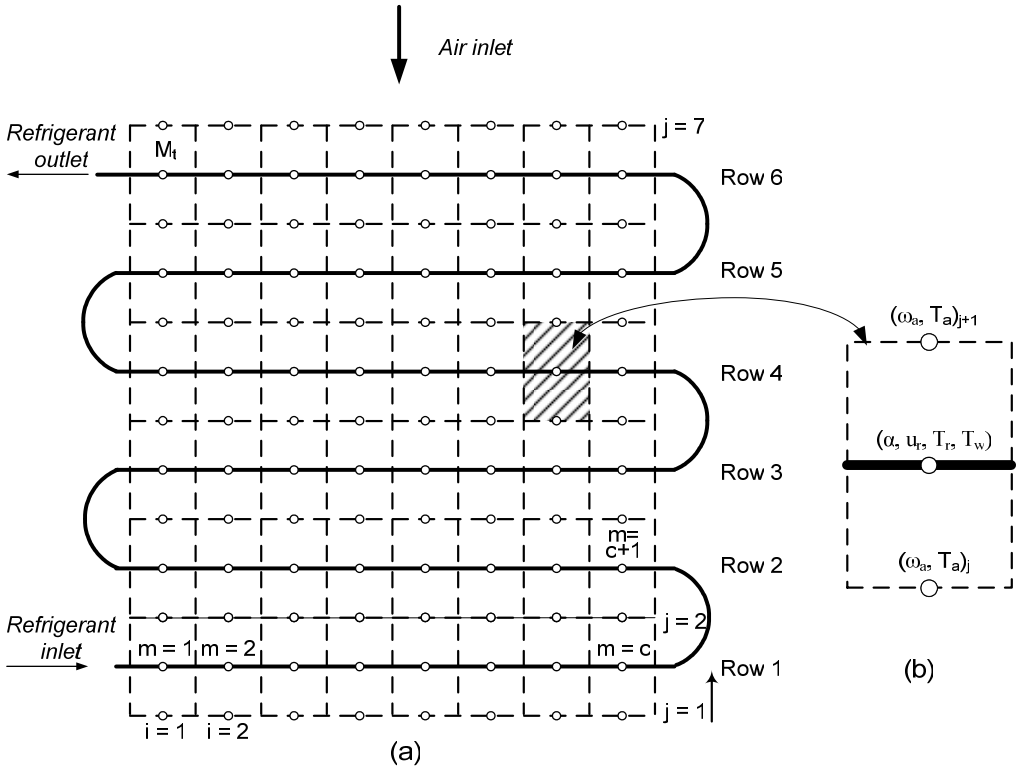

Figure 3.12*: Division of coil for numerical solution*

In the case of two-phase flow region, there are six unknown variables to be solved (α, u_r, T_r, T_w, T_a, ω_a). If a cell is in the single-phase flow region, the vapor void fraction will be unity and the system will be simplified to solving for four unknowns (T_r, T_w, T_a, ω_a). Therefore, the position of liquid dry-out-position is critical in determining the selection of solution methodology. However, the liquid dry-out position is unknown beforehand and varies with time. To overcome this

problem, a two-level iteration method is used, which solves for the unknowns at the refrigerant side and air side at two different levels. The flow chart of the numerical algorithm is shown in Fig. 3.13.

The first level is to solve the variables at refrigerant and tube wall side. When solving for unknowns at the refrigerant and tube wall side, the air conditions (T_a, ω_a) of each cell are assumed to be known and a cell-by-cell method is used to solve for α, u_r, T_r, T_w for two-phase region using Eqs. (3.11), (3.20), (3.33) and (3.37) or T_r, T_w for the single-phase region using Eqs. (3.33) and (3.37). The calculation begins from the refrigerant inlet, i.e., m = 1, in the two-phase region and proceeds cell-by-cell. At χ = 0.99, the liquid dry-out is assumed to occur and the calculation reaches the single-phase region. Therefore, only four equations (for two-phase) or two equations (for single-phase) are required to be solved simultaneously. The Newton-Raphson iteration algorithm (William et al. 1986) is employed to solve this set of equations for its high stability and efficiency.

The second level is to solve the variables at air side. Air temperature and humidity are calculated using equations (3.46) and (3.48). Once the solution is obtained, the leaving air temperature and humidity will be the inlet air condition for the subsequent row in the direction of air flow. Newton-Raphson iteration algorithm is used to solve the equations.

When the wall temperature reaches below the freezing point, the governing equations for frost have to be engaged. The effect of frost growth and accumulation is taken into account in solving the set of equations for refrigerant and air side, by solving Eqs. (3.11), (3.20), (3.33), (3.37), (3.47) and (3.49) with frost equations.

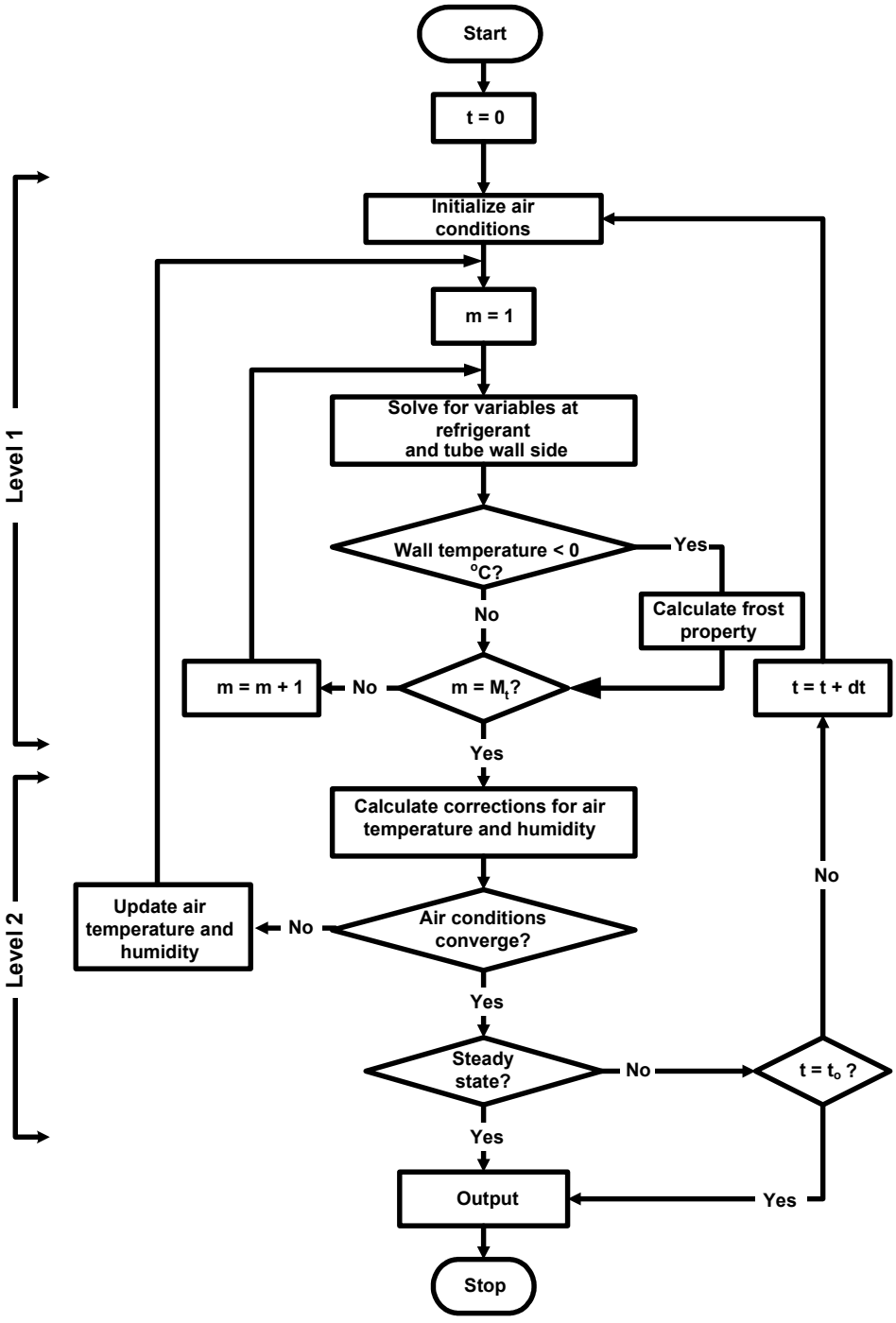

Figure 3.13*: Flowchart of the numerical algorithm*

3.9 Single-phase fluid type refrigerant

In some systems, the working fluid inside the finned tube air cooler is single-phase fluid type refrigerant such as brine or water/glycol instead of volatile refrigerant. For such system, the mathematical model is different from the previous sections and will be shown in this section.

3.9.1 Energy equation for single-phase fluid (brine/water glycol)

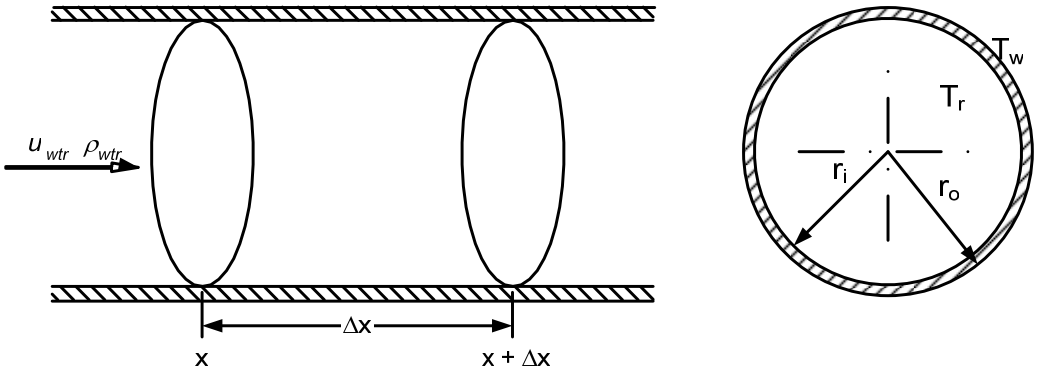

Figure 3.14*: Control volume for derive energy equation.*

The energy conservation equation applied to the control volume in Figure 3.14 is expressed as follows:

Energy into element	-	*Energy out of element*	+	*Energy generated inside element*	=	*Energy stored in element*

The energy into the element, including internal energy of flow in and heat transferred through wall, is the same as shown in Eq. 3.25

The energy out of the element is

$$E_{OUT} = \left[(\rho_r u_r A_r c_{p,r} T_r) \right]_{x+\Delta x}, \tag{3.84}$$

The energy stored in the element is

$$E_{STO} = \rho_r c_{p,r} \frac{\partial T_r}{\partial t} . A_r . \Delta x . \tag{3.85}$$

Therefore, the energy equation is written in the form of

$$2\pi r_o . \Delta x . \dot{q}_{tr} - \left[(\rho_r u_r A_r c_{p,r} T_r) \right]_{x+\Delta x} = \frac{\partial}{\partial t} (\rho_r T_r A_r c_{p,r}) \Delta x. \tag{3.86}$$

Taking the limit of Eq. (3.86) as Δx approaches zero,

$$\frac{2\pi r_o}{A_i} \dot{q}_{tr} - \frac{\partial}{\partial x} (\rho_r u_r c_{p,r} T_r) = \frac{\partial}{\partial t} (\rho_r c_{p,r} T_r). \tag{3.87}$$

The final form of energy equation for single-phase fluid refrigerant,

$$\rho_r c_{p,r} \frac{\partial T_r}{\partial t} + (\rho_r c_{p,r} u_r) \frac{\partial T_r}{\partial x} = \frac{2 r_o}{r_i^2} U_{t,r} (T_{w,o} - T_r) . \tag{3.88}$$

The heat transfer coefficient, U_r can be determined from internal flow condition (Incropera and Dewitt, 2001)

3.9.2 Numerical solution for single-phase fluid type refrigerant

The numerical solution for single-phase fluid type refrigerant is quite similar to the numerical solution presented in Section 3.8. The variables of the refrigerant and the tube, i.e., temperatures of refrigerant and wall are specified at the cell center, while the air temperature and humidity are specified at the cell walls, as displayed in Fig. 3.15 (b). For each cell, 4 governing differential equations, i.e., Eqs. (3.37), (3.46), (3.48) and (3.88), for the above variables, can be discretized into the finite difference form and solved using Newton-Raphson iteration algorithm. The flow chart of the numerical algorithm is Fig. 3.13.

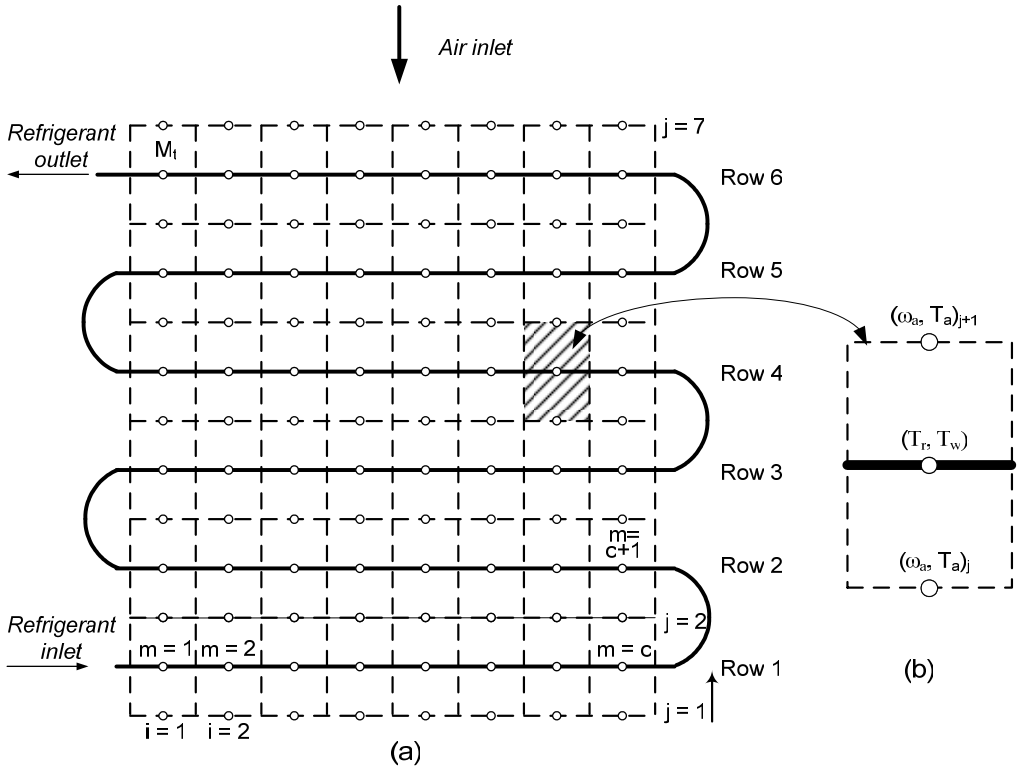

Figure 3.15*: Division of coil for numerical solution for single-phase fluid*

Again, when the wall temperature reaches below the freezing point, the governing equations for frost have to be engaged. The effect of frost growth and accumulation is taken into account in solving the set of equations for refrigerant and air side, by solving Eqs. (3.37), (3.47), (3.49) and (3.88) with frost equations.

3.10 Conclusion

A general distributed model with two-phase flow for refrigerant coupled with a frost model for non-steady performance of finned-tube evaporator under frosting and non-frosting conditions has been presented. The governing equations for refrigerant are derived from conservation of mass, momentum and energy in one-dimensional time-dependent state. The refrigerant flow inside the tube is modeled by a two-phase drift flux model. For tube wall side, the governing equation is derived using conservation of energy in time-dependent state. The equations for air side derived using conservation of mass and energy are solved. The model for single-phase fluid such as brine or glycol/water mixture is also presented in time-dependent state.

When the wall temperature is below the freezing point, the governing equations for mass and energy of frost have to be engaged. For each time step, the changes in frost properties are added to those of the previous time step. The presented model includes the permeation process where the frost surface melt and

some liquid soak into the frost layer when frost surface temperature reaches the melting point.

In the subsequent chapter, numerical simulation will be carried out to predict the performance of the evaporator by varying the parameter which will affect the frost growth. Comparison will also be made with existing experimental data reported by other researchers.

CHAPTER 4

Numerical Simulation, Results and Discussion

A simulation program was written using FORTRAN programming language. The computer code was an extension from in house previous code. Substantial modifications on code were performed in order to incorporate the air cooler under frost condition. The modifications involved developing a new subroutine for calculation of frost properties which includes the frost thermal conductivity, frost thickness, frost density and heat and mass transfer in frost layer. Extensive modifications of subroutines include solving the equations when the frost forms on the cells (Eqs. 3.11, 3.20, 3.33, 3.37, 3.47 and 3.49). The modifications also include changes of air side heat transfer coefficient and pressure drop when frost occurs. The algorithm of the numerical simulation is based on the flowchart as described in Figure 3.13. The description for solving the mathematical model, which includes the frost condition, is descried in Section 3.8. A commercial available container air cooled evaporator was selected for geometrical data and performance prediction. The predicted results could be compared with published data.

Sensitivity studies on the mathematical model were carried out first as they would affect the numerical results. This was done by selecting the suitable number of nodes for fin, number of cells, convergence criterion and time steps for simulation. The results from the sensitivity studies will be used for the subsequence simulations.

4.1 Selection of Number of Nodes for fin, Convergence Criterion, Number of Cells and Time Steps for Simulation

4.1.1 Selection of number of nodes for fin

Selection of number of nodes for fin can be done by comparing the analytical solution and finite difference solution for steady state. The general steady state equation for heat transfer in extended surface for an annular fin is given as follows (Incropera and DeWitt (2002):

$$\frac{d^2T_{fin}}{dr_{fin}^2}+\frac{1}{r_{fin}}\frac{dT_{fin}}{dr_{fin}}+M(T_a-T_{fin})=0, \tag{4.1}$$

where $M \equiv \frac{2U_o}{k_{fin}\delta_{fin}}$ and the boundary conditions are stated as

$$T_{fin}\,(r_{fin}=0)=T_w \qquad \frac{\partial T_{fin}}{\partial r_{fin}}(r_{fin}=r_{fin,o})=0 \tag{4.2}$$

By applying the boundary condition, Eq. (4.2), the analytical solution for Eq. (4.1) where the temperature distribution along the fin can be given as follows:

$$T_{fin}=T_a-\frac{(T_a-T_w)\left[K_1(Mr_{fin,o})I_0(Mr_{fin})+I_1(Mr_{fin,o})K_0(Mr_{fin})\right]}{K_0(Mr_{fin,i})I_1(Mr_{fin,o})+K_1(Mr_{fin,o})I_0(Mr_{fin,i})}, \tag{4.3}$$

where *K* and *I* are modified Bessel functions.

In selecting number of nodes for fin, simulations were carried out based on a selected input as follows:

Table 4.1*: Input parameter for selecting number of nodes for fin*

Fin thickness (mm)	0.19
Conductivity of fin (W/m K)	204
Fin base temperature (^{o}C)	15
Fin inner radius (mm)	6.35
Fin outer radius (mm)	16.68
Air Temperature (^{o}C)	30
Heat transfer coefficient (W/m K)	50

The analytical result is compared with the simulation result based on Eq. (3.40) for several different numbers of nodes. The results are shown in Fig. 4.1.

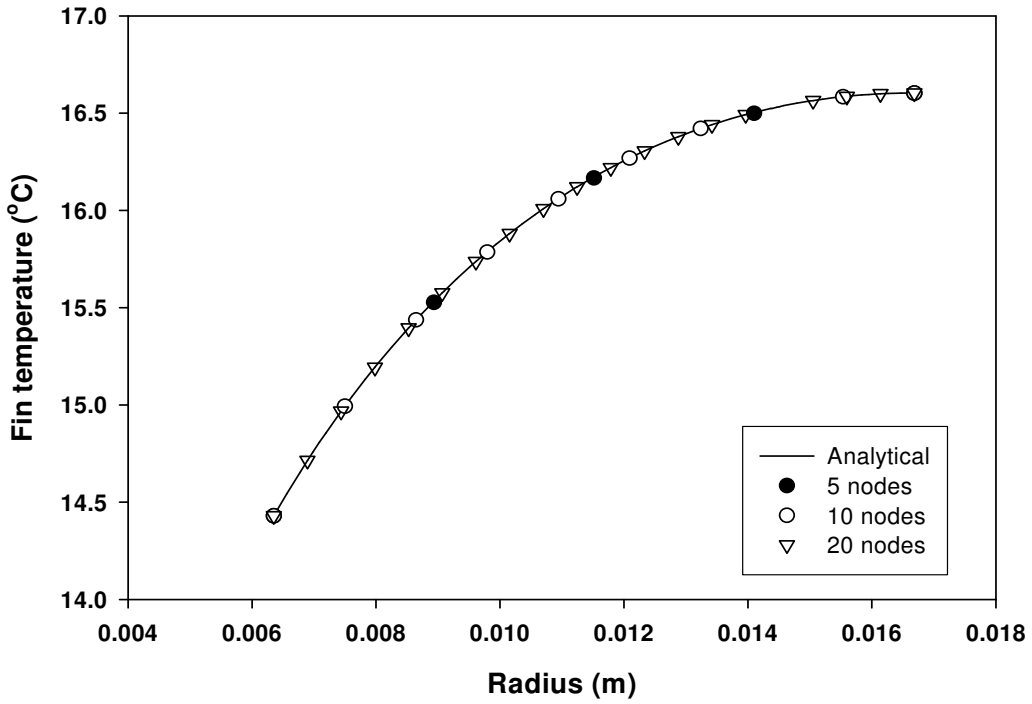

Figure 4.1*: Temperature distribution of analytical solution compared to various finite difference nodes sizes*

From Figure 4.1, it can be seen that the solution using finite difference compared well with the analytical solution. Finite difference method using 5, 10 and 20 nodes does not make much different. By considering the computational time and visualization of frost on fin, finite difference method with 10 nodes was used for simulation.

4.1.2 Selection of convergence criterion

In selecting the convergence criterion, simulations were carried out based on a selected input as shown in Table 4.2. The coil specification is based on actual commercial container refrigeration unit.

Table 4.2*: Input parameter for simulation*

Refrigerant type	R12
Inlet air temperature (^{o}C)	14.5
Inlet air relative humidity (%)	55.0
Total air flow rate (kg/s)	1.14
Refrigerant flow rate (kg/s)	0.079
Inlet refrigerant vapor quality	0.25
Inlet refrigerant pressure (kPa)	300.0
Coil length (mm)	1632.0
Number of fins per inch (mm/fin)	8 (3.18)
Number of circuits	9
Number of rows	6
Inner diameter of tube (mm)	12.27
Outer diameter of tube (mm)	12.70
Tube spacing in air flow direction (mm)	27.5
Tube spacing perpendicular to air flow direction (mm)	31.8
Fin thickness (mm)	0.19
Conductivity of fin (kW/m K)	0.204
Conductivity of tube (kW/m K)	0.398
Fin specific heat (kJ/kg K)	0.384
Tube specific heat (kJ/kg K)	0.896
Density of fin (kg/m^3)	2707.0
Density of tube (kg/m^3)	8954.0
Time step (s)	To be selected
Divided section numbers each row	To be selected
Convergence criterion	To be selected

Selection of convergence criterion was carried out first. The convergence criterion of 10^{-3}, 10^{-4} and 10^{-5} were evaluated on 40 cells per row for refrigerant temperature and velocity. Figure 4.2 shows the results of the simulation. It can be seen that the results for the convergence criterion of 10^{-4} and 10^{-5} are much closed to each other. Therefore, based on the results of the last row refrigerant temperature and velocity, convergence criterion of 10^{-4} was used for simulations.

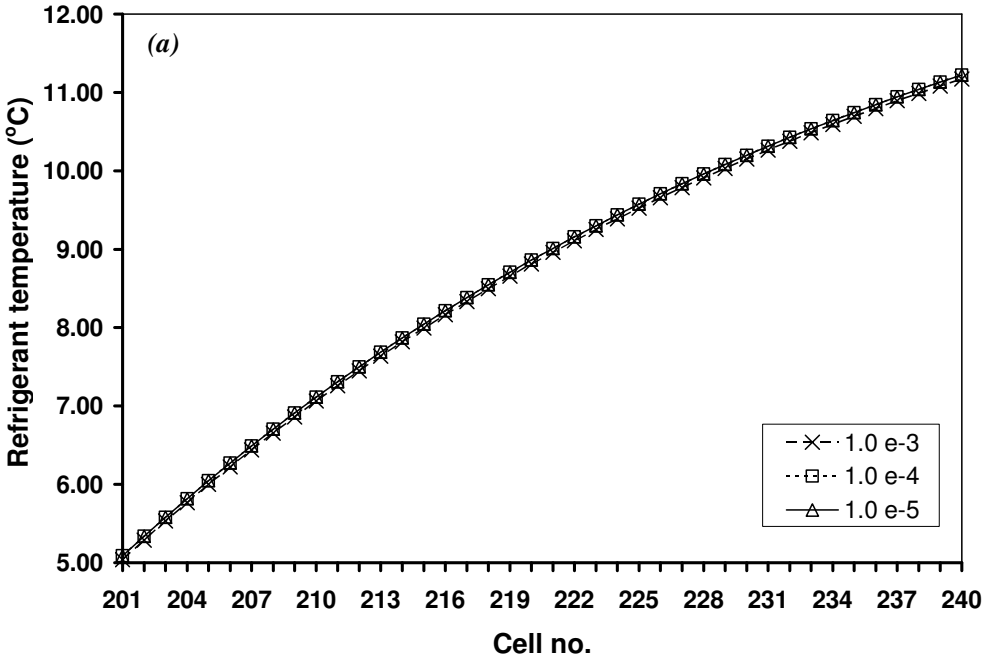

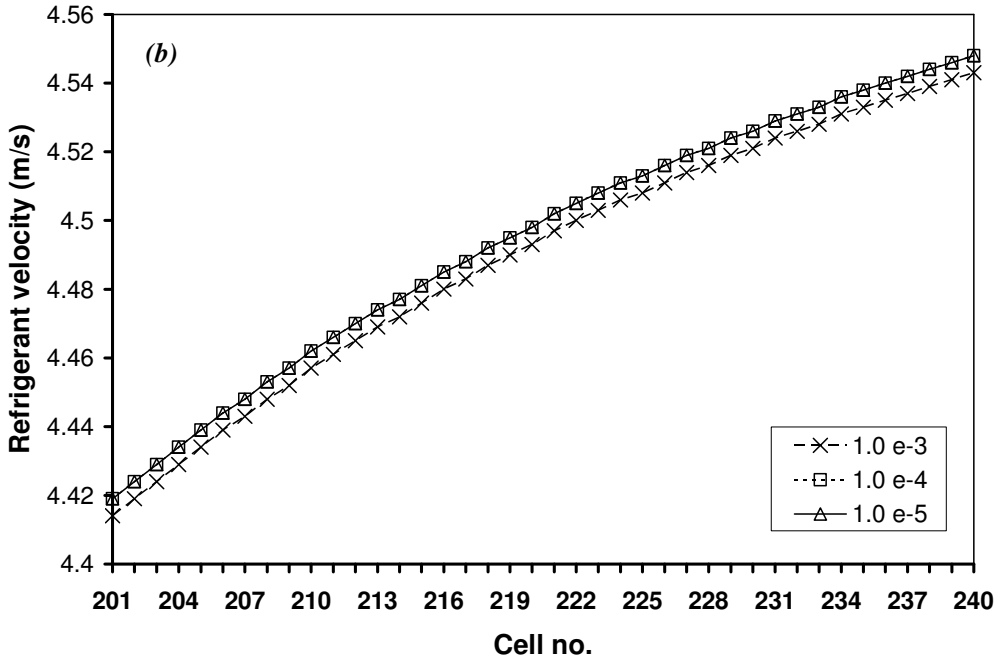

Figure 4.2*: Selection of* **convergence criterion** *for simulation by comparing (a) refrigerant temperature; (b) refrigerant velocity for last row of coil (40 cells/row)*

4.1.3 Selection of number of cells

After determining what the convergence criterion to be used, selection of cells per row was carried out. Cells of 10, 20, 40 and 80 per row were chose to determine the best cells per row. Fig. 4.3 (a) shows the results for refrigerant temperature and Fig. 4.3 (b) shows refrigerant velocity at the last row of the coil. The values above 40 cells per row, i.e. 80 cells per row are same as 40 cells per row. Therefore, 40 cells per row was selected for all subsequence simulations. For a 6 row coil, there are a total of 240 cells to analyses.

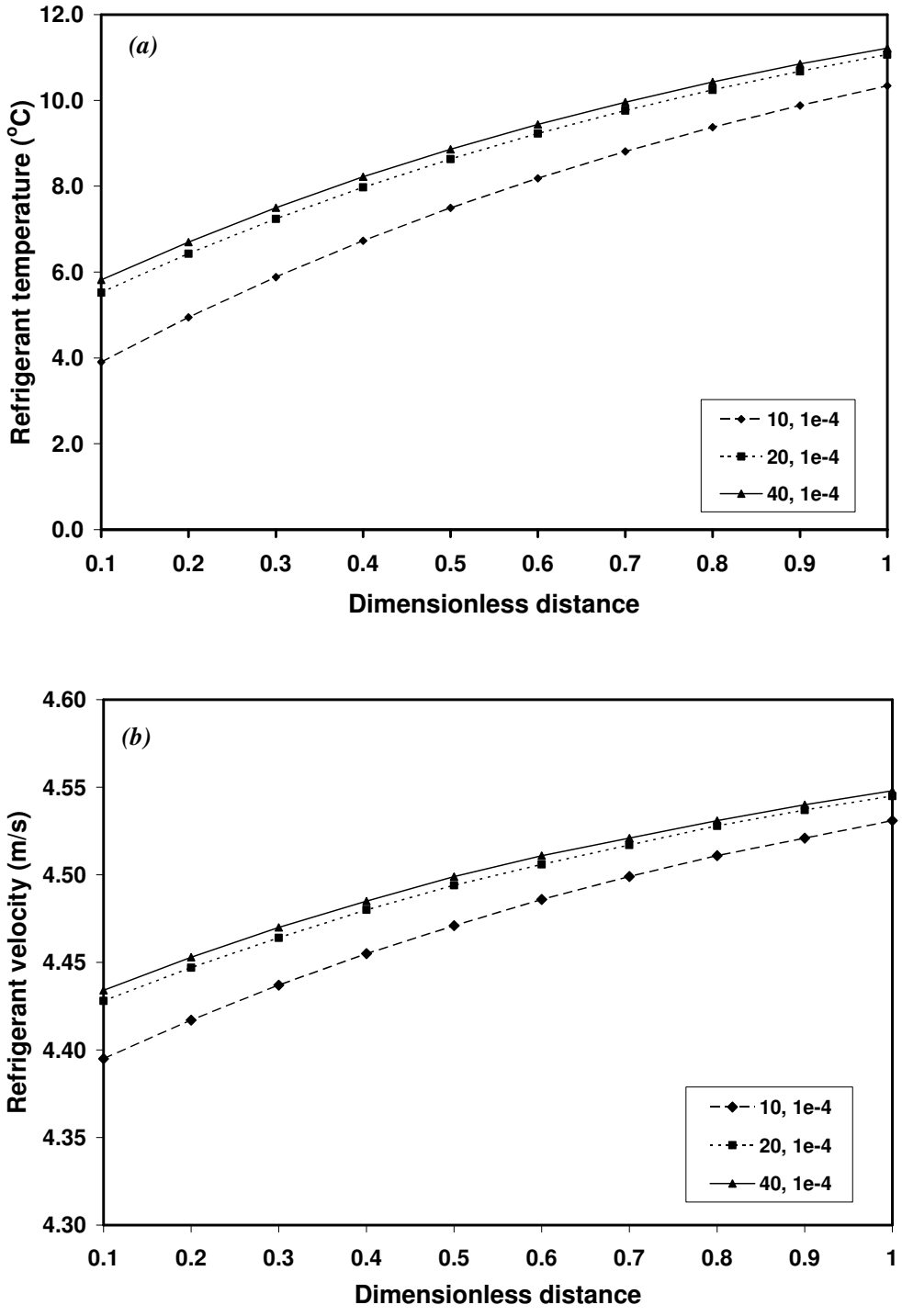

Figure 4.3*: Selection of cells per row by comparing the (a) refrigerant temperature; (b) refrigerant velocity, at the last row of coil*

4.1.4 Selection of time step

The program was written in a way that the time step can be varied depending on the user's preferences. The smaller the time step, the better the result but at the same time, the computational time is also relatively increased. The selection of time step must base on the condition where the frost formed and grown on the evaporator. The frost formation and growth is an unsteady process and will affect the system performance. Therefore, the conditions stated in Table 4.2 remain the same except the following:

Table 4.3*: Input parameter for simulation to determine time step*

Inlet air temperature (^{o}C)	5
Inlet air relative humidity (%)	60.0
Refrigerant flow rate (kg/s)	0.079
Inlet refrigerant vapor quality	0.2
Inlet refrigerant pressure (kPa)	200.0

Several runs were carried out based on time step of 10 s, 20 s, 30 s, 50 s and 60 s for a total simulation period of 300 s. The results were compared in term of refrigerant velocity and temperature at 300 s. Fig. 4.4 (a) shows the results of the refrigerant temperature and Fig. 4.4 (b) shows the refrigerant velocity for time step of 10 s, 20 s, 30 s, 50 s and 60 s at the time of 300 s. From both figures, the results show that the temperature and velocity of the refrigerant for time step of 20 s and below are almost the same. Therefore, a time step of 20 s is selected for simulations.

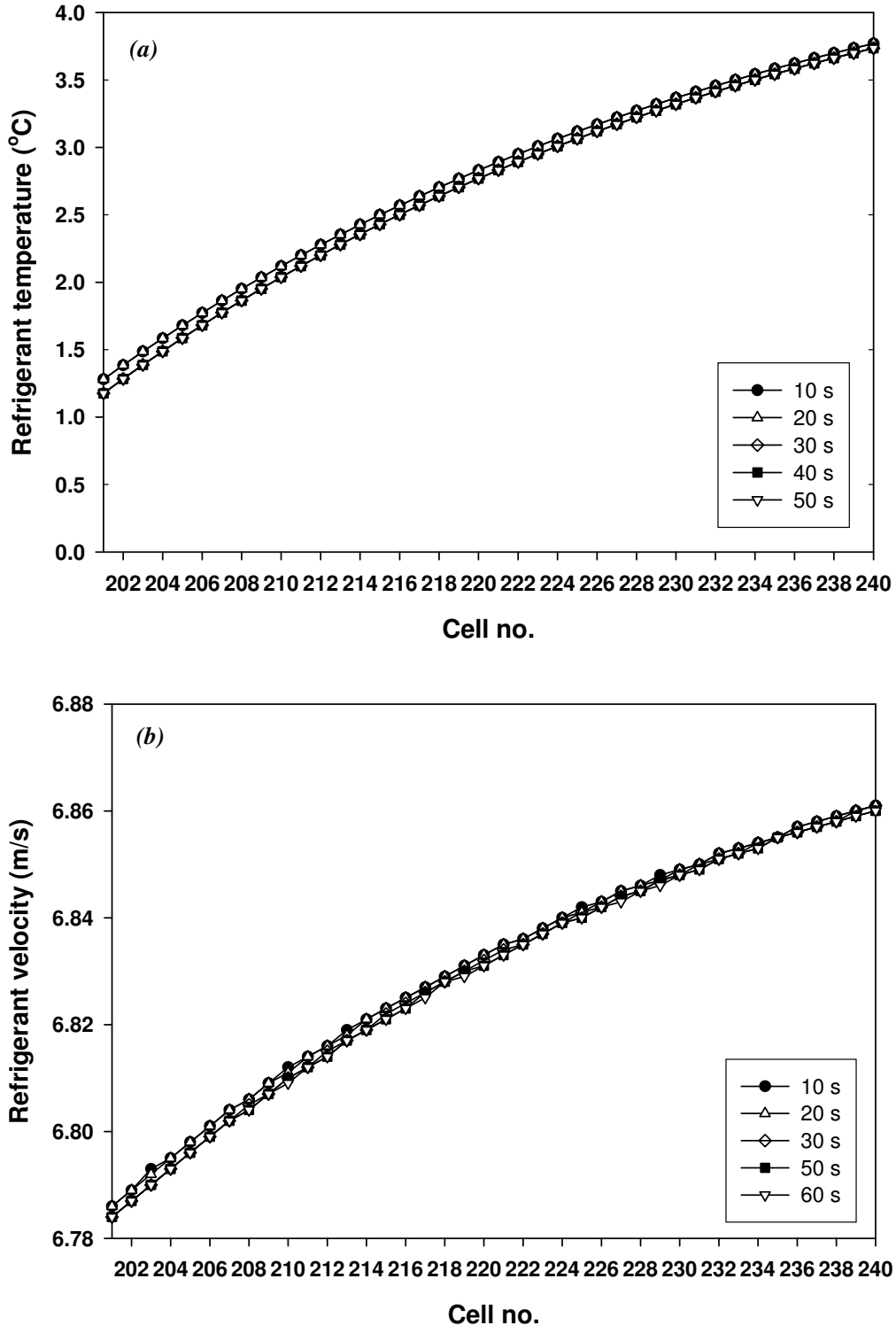

Figure 4.4*: Time steps selection: (a) Refrigerant temperature at T=300 s; (b) Refrigerant velocity at T=300 s*

4.2 Simulation Results for Non-Frosted Evaporator

4.2.1 Various flux models

In two-phase refrigerant flow, the velocity of refrigerant liquid and vapor is assumed to be the same in homogeneous flow model. But in reality, the flow of refrigerant liquid and vapor are not and various drift flux model have been presented in Section 3.2.1. In this section, simulation of the drift flux models are presented and compared with other researcher's result.

The simulation input is based on the experimental condition of Jia et al. (1995). The evaporator is a finned-tube type heat exchanger consisting of nine circuits, six rows and 514 aluminum fins. The outer diameter of the copper tube is 12.7 mm with a wall thickness of 0.432 mm. The evaporator has external dimensions of 1632 mm long, 286 mm wide and 165 mm high with a total air side surface area of 44.8 m^2. The air and refrigerant flows are arranged as a counterflow configuration. In their experiment, the system was allowed to reach steady state with the help of electric heater. The air mass flow rate and temperature at the inlet temperature were 1.14 kg/s and 14.5 ^oC. Once the system reached steady state, a change in the refrigerant flow rate was initiated by opening or closing a step of the electronic expansion valve. The step increase was about 9.5 % in the refrigerant mass flow rate from 73 g/s. When the step change was introduced, both evaporating and condensing pressure increased. The changes of evaporating pressure and refrigerant vapor quality were represented by straight-line interpolation of the experimental results presented.

The simulation calculates the steady state condition based on the input condition from the experiment data given as a start. At simulation time of 30 s, a step

increase in refrigerant flow rate from 73 g/s to 80 g/s was introduced with the evaporating temperature and refrigerant vapor quality changed according to the experimental results. The result is compared with experimental data from Jia et al. (1995). Figure 4.5 shows the simulated result for different flux models and experimental data.

Figure 4.5 (a) shows a prediction of degree of superheat using four different flux models namely homogeneous, Chisholm, CISE and Smith models with same input parameters. The graph shows decreasing trend of superheat when the refrigerant mass flow increases. From this figure, it can be seen that the results of drift flux models, namely Chisholm, CISE and Smith model, are close to each other and experimental data as compared with the homogeneous model. The drift flux models reach a steady state at 180 s. The homogeneous model gives a shorter transient response period because it assumes equal velocity for both liquid and vapor. This assumption oversimplifies the interaction between liquid and vapor in the two-phase flow region, which results in a lower pressure loss and a faster transient response. Comparing with the three drift flux models, the homogeneous model underestimates the degree of superheat up to about 1 ^{o}C.

Figure 4.5 (b) shows a prediction of air temperature outlet at the left hand side with uniform input parameters. The air temperature shows decrease of air temperature and eventually reaches a steady state. The drift flux models predict the result close to the experimental data but the experimental data shows continuous decrease trend. The discrepancy is because the input air temperature was kept at constant 14.5 ^{o}C while in actual experimental, the input temperature gradually decreased. Homogeneous model again shows a shorter transient response time.

The calculated refrigerant liquid dry-out position is shown in Figure 4.5 (c). The graph shows that with a step increase in the refrigerant flow rate, the predicted liquid dry-out position moves towards the evaporator outlet. From the graph, it can be shown that the three drift flux models give almost the same predictions while homogeneous flow model predicts a larger two-phase flow region than the drift flux models. The homogeneous model gives a prediction of 20 s shorter transient period of the evaporator compared with predictions of three drift flux models.

From the comparison of different flux model and experimental results, a conclusion can be made that drift flux models are capable to predict the actual performance of the evaporator. Among the three drift flux models presented, the Chisholm model is preferred due to its simplicity of the correlation. Therefore, the simulation will base on the Chisholm model for two-phase refrigerant flow.

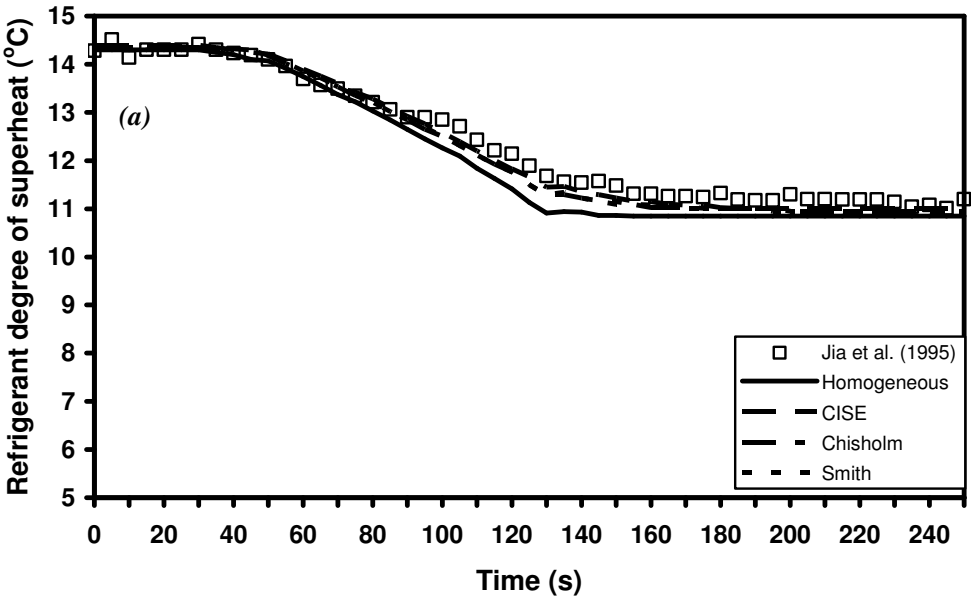

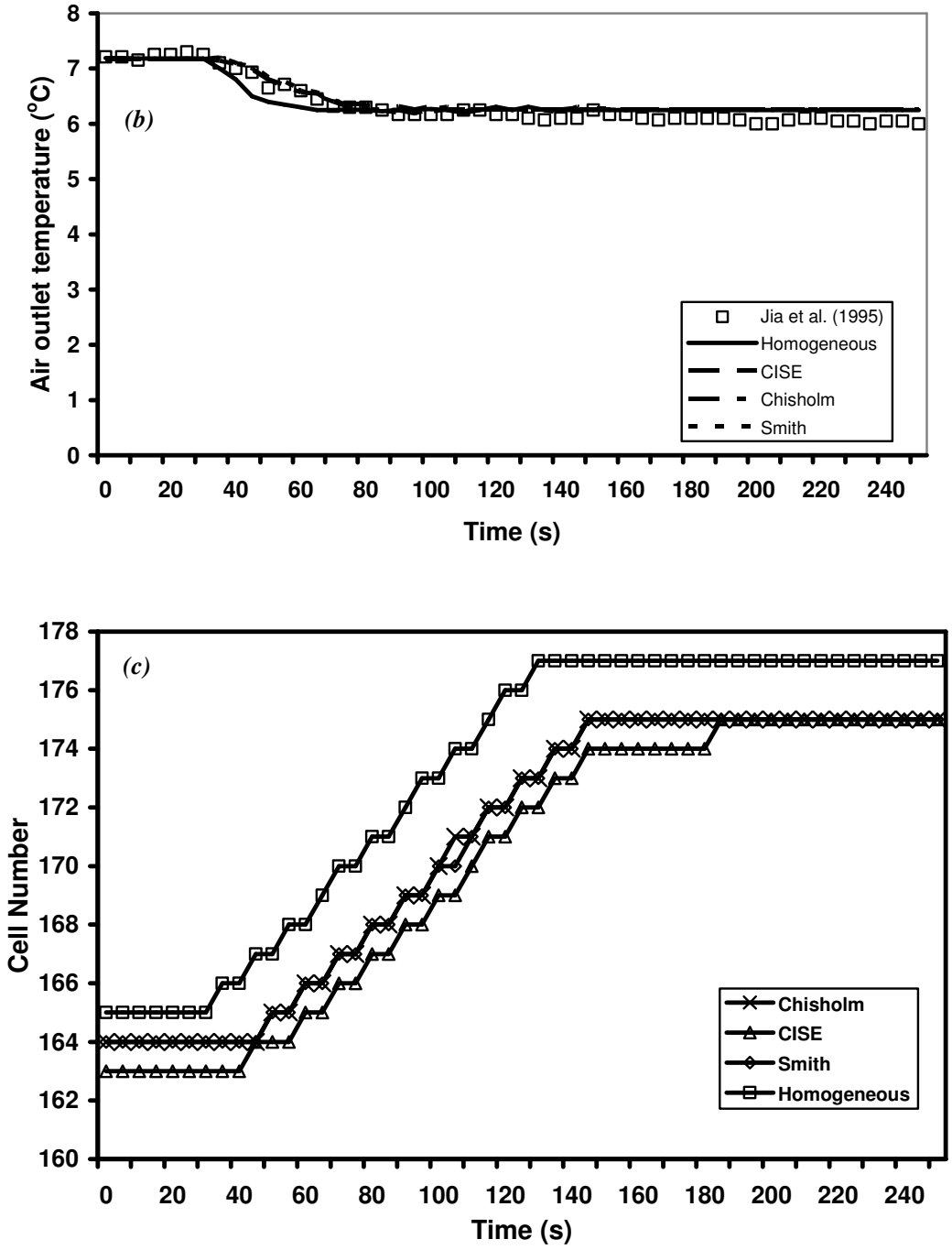

Figure 4.5*: Comparison of simulation results using four different flux models (a) Degree of superheat (b) Air temperature outlet at left hand side, and (c) Refrigerant liquid dry-out position*

4.2.2 Effect of refrigerant liquid dry-out position and air temperature distribution inside the evaporator

The temperature inside the evaporator coil varies greatly caused by the two-phase flow of refrigerant. Figure 4.6 shows a contour plot of air temperature variation inside the evaporator with a uniform inlet air temperature of 14.5 ^{o}C based on the calculated value of Jia et al. (1995) input condition at the end of the simulation. From this figure, it can be seen that the air temperature is colder at the left hand side of the coil from cell 1 to around cell 16 and cells parallel to them in the direction of air flow as compared to the other cells at the same rows.

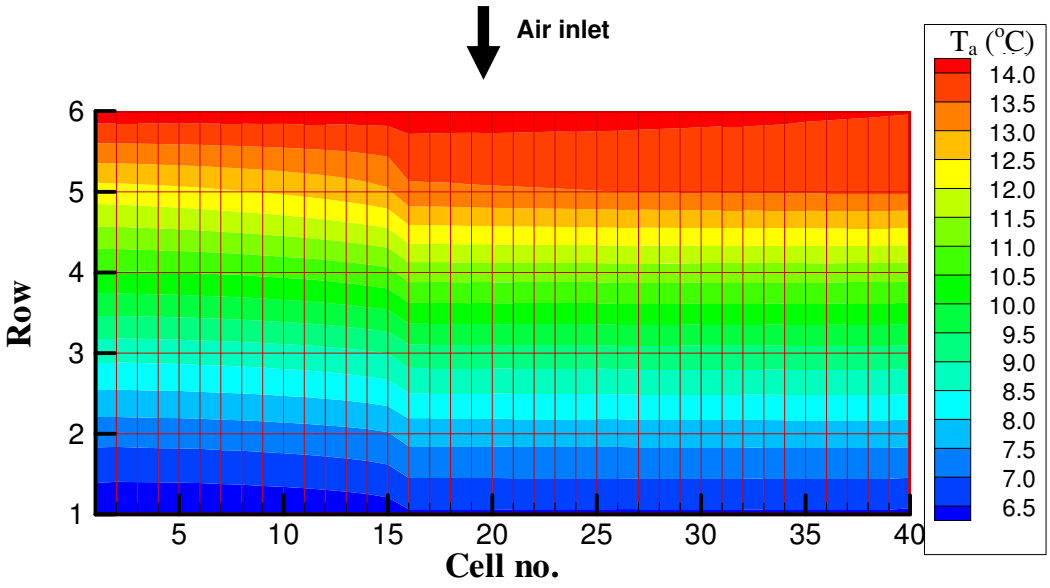

Figure 4.6*: Calculated air temperature distribution inside the evaporator coil.*

Figure 4.7 shows the refrigerant vapor quality, χ, along the coil from inlet to outlet. The refrigerant liquid dry out position can be noticed to occur at fifth row, cell no. 175. This implies that the cell no 161 to 175 on the fifth row are in two-phase

while the rest of the cells on fifth row are in single-phase. Realizing that two-phase refrigerant can absorb more heat compared to its single-phase state, therefore, it is logical to observe that the temperature for air passing through the tubes which refrigerant is in the two-phase section is colder than the air passing through the tube which refrigerant is in the single-phase section.

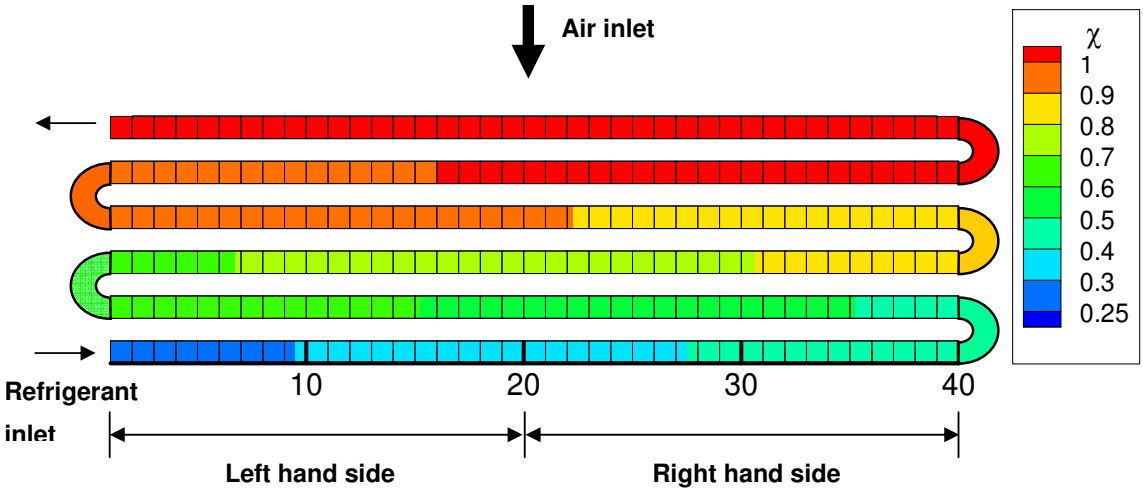

Figure 4.7*: Calculated refrigerant vapor quality along the coil.*

Since phase change has influence on the air temperature distribution inside evaporator, it is useful to understand the changes when refrigerant liquid dry-out occurs at different positions. The evaporator is partitioned as left and right hand side as shown in Fig. 4.7. The liquid dry-out position is defined as a non-dimensional position in which zero corresponds to the left end of the coil and unity to the right end of the coil, and the air temperature difference is defined as the difference between averaging air temperatures of the right and the left side hand side ($T_{air, right}$ - $T_{air, left}$).

The air inlet temperature maintains constant and uniform at 14.5 °C. By changing the refrigerant flow rate, the refrigerant liquid dry-out position can be controlled to occur at different positions. To observe the effect of refrigerant liquid dry-out position to the air temperature, the positions are set to occur at both end of row 3, 4, 5, 6 and three evenly distributed points on each row. Figure 4.8 shows the predicted influence of the liquid dry-out position on the air off the evaporator.

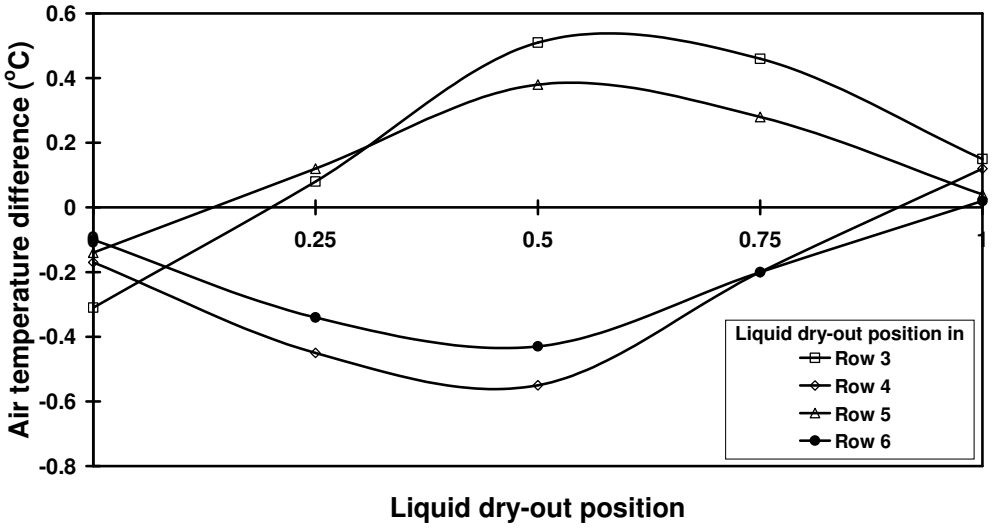

Figure 4.8*: Influence of liquid dry-out position on evaporator air outlet temperature*

As can be seen from the above figure, the air temperature difference is lowest when the liquid dry-out position happen at the two ends of the coil for any given row. The air temperature difference is highest when it happens in the middle of the coil. It is also observed that the more rows flooded by the two-phase flow, the lower the air temperature difference would be resulted, i.e., the lower the superheat, the more uniform air temperature off the coil may be obtained. This phenomenon is agreed

with control laboratory test where the location of superheat region had the most effect on uniformity (ASHRAE 2002).

4.3 Simulation Results on Frosted Evaporator

When the evaporator surface temperature falls below the freezing point, frost forms and continues to grow. The present of frost has impact on the evaporator performance. In this section, the effect of frost formation and growth to the evaporator is studied. Simulation was carried out based on the coil geometry and other parameters shown in Table 4.2 and input air and refrigerant conditions shown in Table 4.3.

In practical condition, the evaporator operates in transient manner. The refrigerant and air inlet condition change based on space cooling load and the regulating of expansion valve. In order to understand the changes of evaporator performance due to frost growth alone, the simulation will keep the input parameter for air and refrigerant constant through the simulation period. The total simulation time is 3600 s with 30 s time step.

As the properties of air and refrigerant vary due to the phase change, the frost growth on the coil is examined at 30 selected cells and 5 groups or positions as shown in Fig. 4.9. To visualize the variations along a row, 5 cells are selected for each of the 6 rows, with 2 cells at both ends and 3 cells equally spaced in between. The selected cells at each row are grouped into 5 typical groups in the air flow direction for studying the changes between rows for the 5 selected positions.

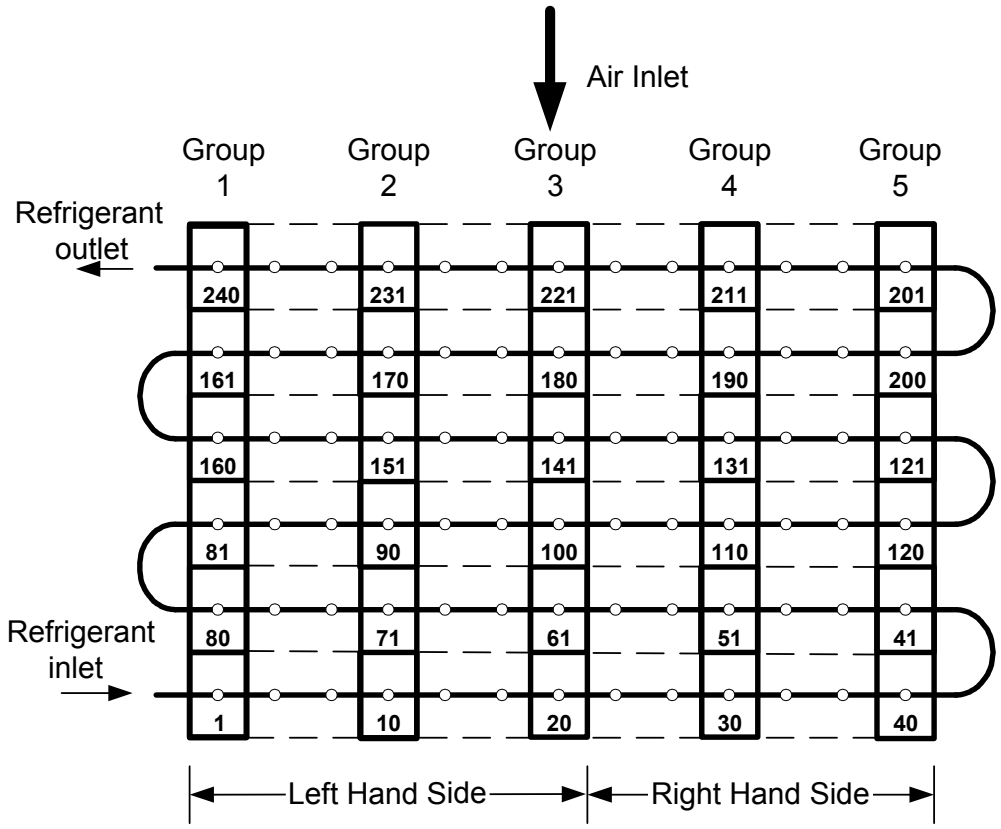

Figure 4.9*: Selected cells and groups for examination.*

4.3.1 Effect of frost on air outlet, refrigerant liquid dry-out position and total energy transfer rate

Frost deposition and accumulation on evaporator surface act as a thermal insulator between the surface and the humid ambient air. As the surface area coverage increases with frost accumulation, less heat exchange occurs between air and cold surface and hence the air outlet temperature increases. As shown in Fig. 4.10, the average air outlet temperature increases from -2.76 ^{o}C to -2.56 ^{o}C at the end of simulation. The refrigerant liquid dry-out position has also shifted from the initial position of cell 148 to cell 180, due to the insulation effect caused by the frost. The

degree of superheated refrigerant at exit reduces from 16.12 ^{o}C to 14.07 ^{o}C, as less refrigerant boils off in the initial two-phase region.

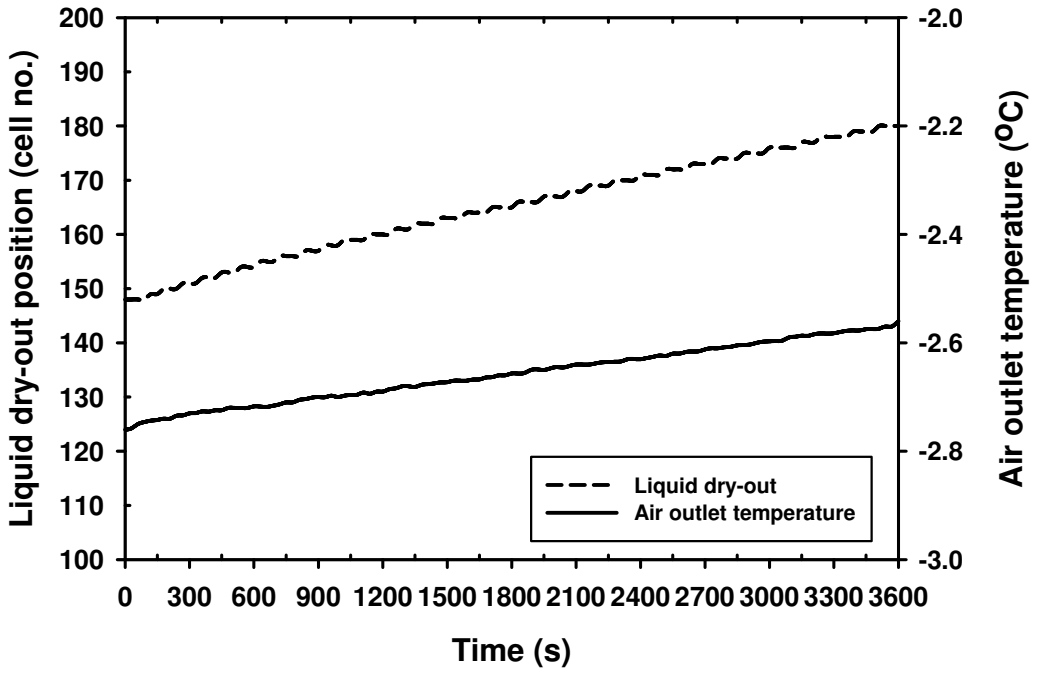

Figure 4.10*: Effect of frost on air outlet temperature and refrigerant liquid dry-out position.*

The air outlet temperature on the right hand side and left hand side varies as the refrigerant liquid dry-out position shift from cell no. 148 to 180. As can be seen from Fig. 4.10, the initial refrigerant liquid dry out position is at position 148, which is around the middle of forth row. Four rows on the right hand side were still in two-phase refrigerant flow as compare with three rows on the left. This causes the air outlet temperature on the right hand side is colder than that on the left hand as shown in Fig. 4.11. The difference in air temperature on the right and left hand side gradually decrease and eventually reached the same temperature at around 1600 s. At

this time, the first four rows were in two-phase refrigerant and the liquid dry out position is on cell no. 163. As the less liquid refrigerant boil-off due to insulation effect caused by frost, the refrigerant liquid dry-out position shifts to the middle of the fifth rows. During this period, the air outlet temperature on the left hand side is colder than the right hand side. Such variation will have influence on the frost growth along the evaporator coil as the air and wall temperature are part of the influential parameter.

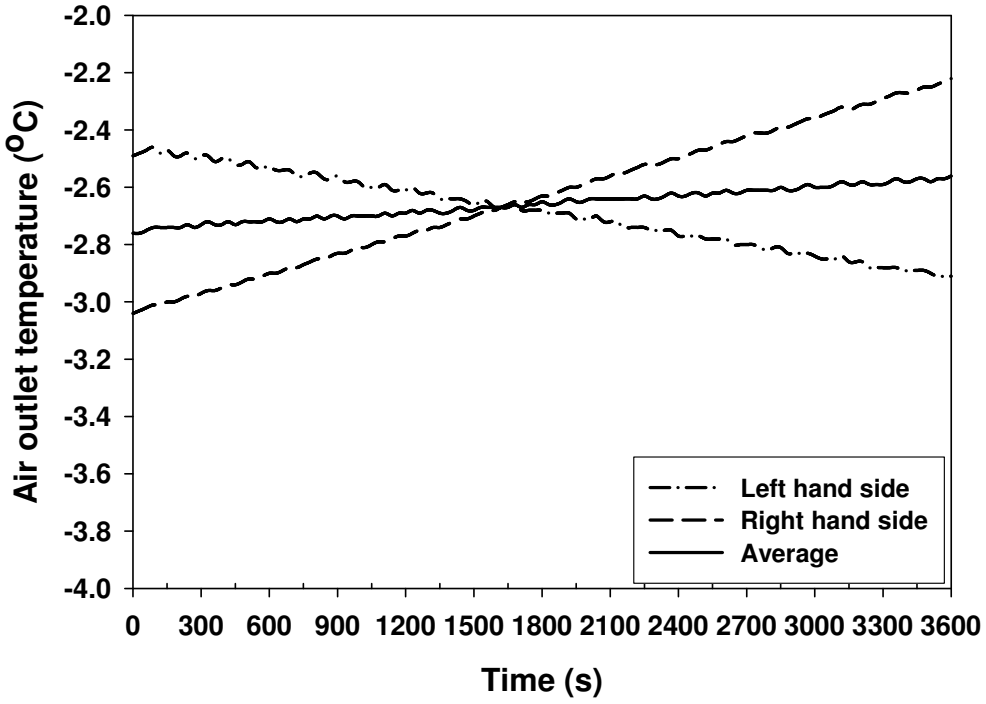

Figure 4.11*: Effect of frost on air outlet temperature on left and right hand side.*

The growth of heat transfer resistance by frost lead to the deterioration of evaporator performance. The total energy transfer rate from air to refrigerant reduces by nearly 1 % in one hour, from initial value of 10.75 kW to 10.65 kW, due to the frost effect as shown in Fig. 4.12.

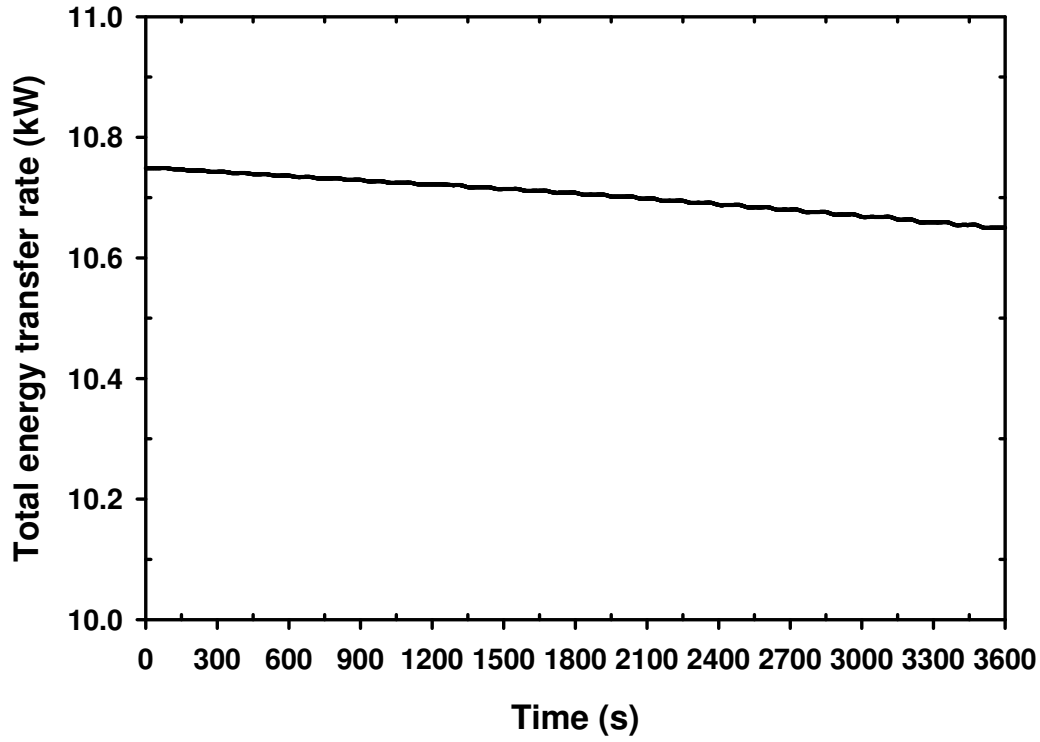

Figure 4.12*: Effect of frost on total energy transfer rate.*

4.3.2 Frost growth and mass accumulation

The frost continues to grow in height and increase in density with time. Figure 4.13 shows the frost growth and densification of frost for cell no. 30. The trend of change shown is consistent with existing experimental data (Chen et al. 1999, Lee et al. 2003). The growth and densification of frost act as an insulation that reduces the heat transfer between air and refrigerant. As less heat is being transferred to the refrigerant, the cold refrigerant that passes through the next cell propagating the frost formation along the coil, resulting in the increase of frost mass accumulation with time.

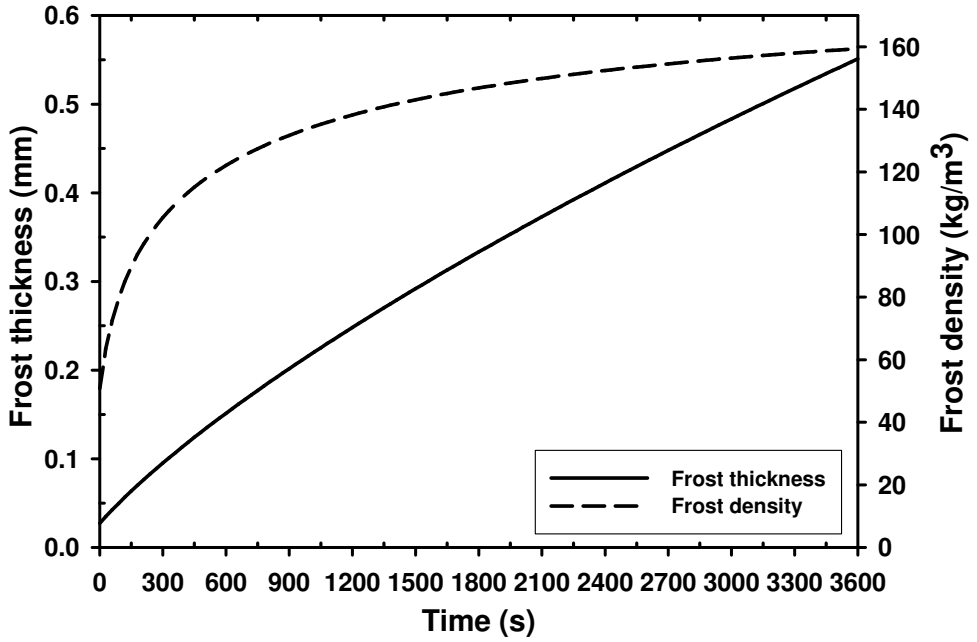

Figure 4.13*: Frost height and density against time for cell no. 30.*

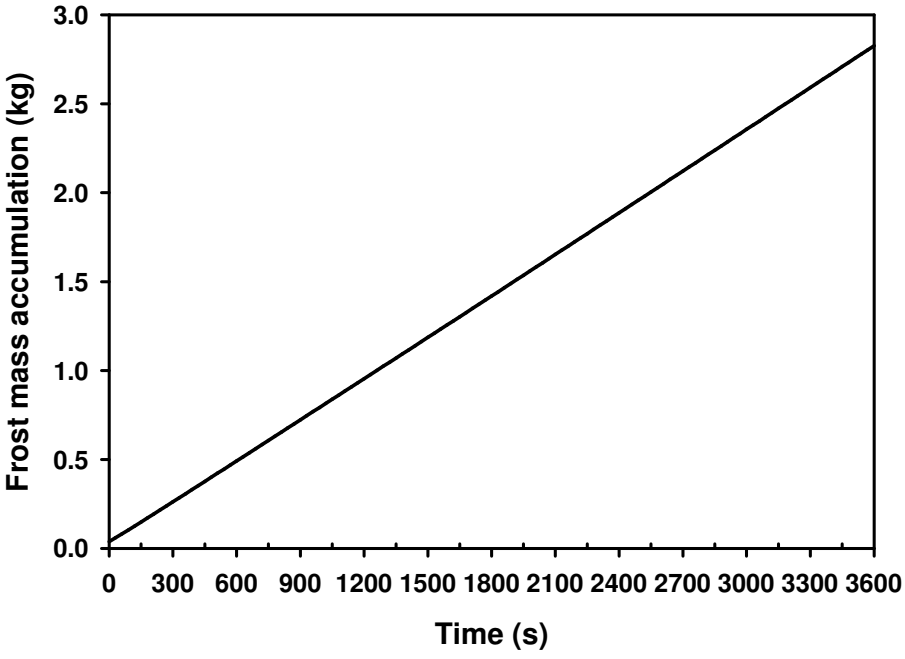

Figure 4.14*: Frost mass accumulation against time.*

Figure 4.14 shows the total mass accumulation against time with a total of 2.82 kg accumulated over a period of 3600 s. The trend of change is agreed well with the existing experimental data. (Senshu et al. (1990), Kondepudi and O'Neal 1993(b))

4.3.3 Variation of frost, air and wall temperature inside coil

The air and wall temperature inside the coil vary and they are due to the phase change of the refrigerant as shown in Section 4.2.2. The influence of the variation of air and wall temperature to the frost growth will be shown in this section. Figure 4.15 shows the variation of air temperature inside the coil at 3600 s. The variation of wall temperature along the tube for the selected groups at 3600 s is shown in Fig.4.16 and from Fig. 4.10, the liquid dry out position occurs at cell 180.

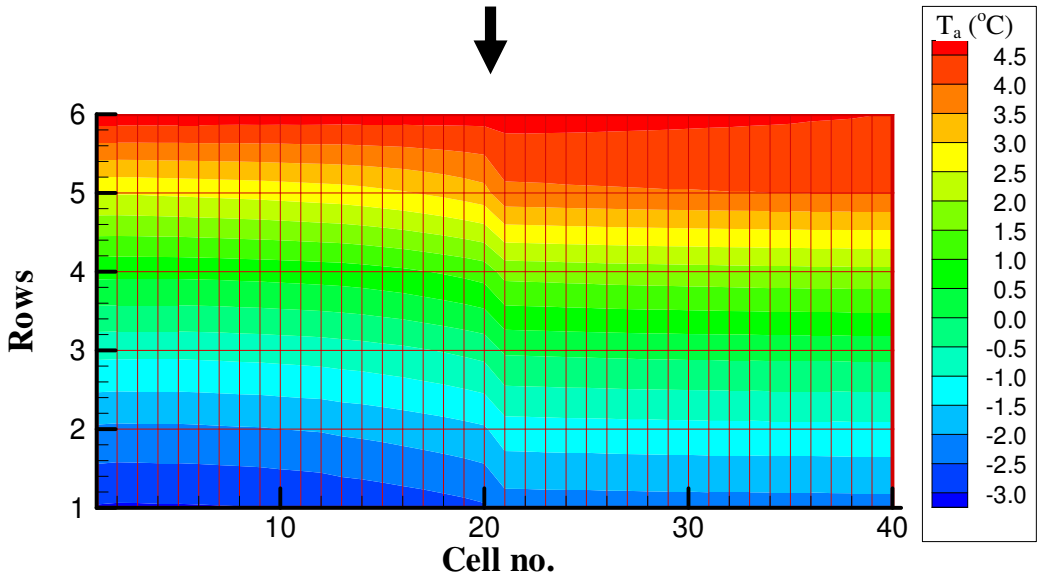

Figure 4.15*: Variation of air temperature inside the coil for frosted condition***.**

The air entering at 5 °C at the 6th row and exiting with air temperature on the right hand side is slightly colder than that at the left hand side. This is due to the wall

temperature being colder or the refrigerant at the right hand side being less superheated as compare to that at the left hand side. When the air passes through the 5th row where the refrigerant liquid dry out position occurs, the air temperature differs greatly, with the air temperature on the left being much colder, due to the phase change in the refrigerant. The wall temperature on 5th row, from Fig. 4.16, shows that the temperature increases from around -2 °C to 2 °C in the transition from two-phase to single-phase zone.

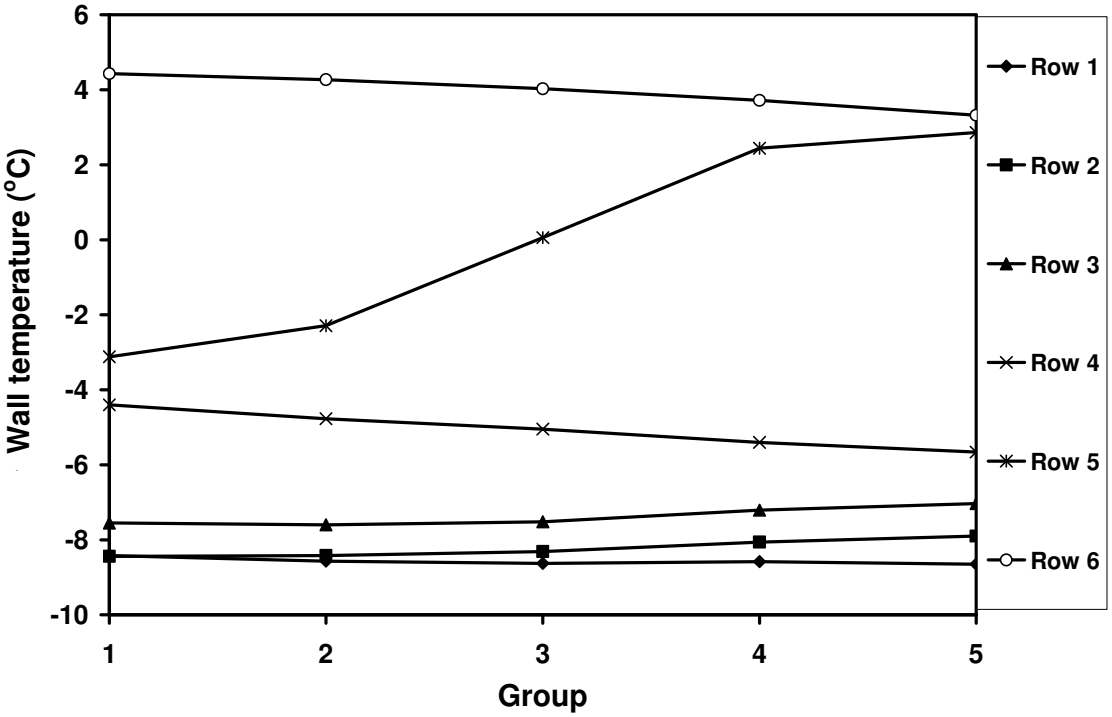

Figure 4.16*: Variation of wall temperature along the tube for frosted condition at 3600 s***.**

Figure 4.17 shows the variation of frost height and wall temperature for the selected cells in the first row, i.e., cells 1, 10, 20, 30 and 40, against time. It is observed that at the early stage, the wall temperature is slightly lower at the right side cells. This is due to the friction pressure drop of refrigerant in the tube and the colder air temperature caused by the phase change effect at the early stage. The frost layer is

slightly thicker on the right as compared with the left. As the frost continues to grow, the wall temperature decreases as less heat is being transferred due to the insulation effect.

From Fig. 4.17, it is noted that there is a sudden drop of wall temperature at time around 1140 to 1230 s for cell 1. This effect is caused by phase change where the refrigerant liquid dry-out position occurs in the same group, i.e., cell 160 and 161. Similar trend is also noted for cell 10 at time 270 s and 2280 s where the refrigerant liquid dry-out position is at cells 151 and 170. Cell 20 shows this trend at around 3510 s when the dry-out position is at cell 180.

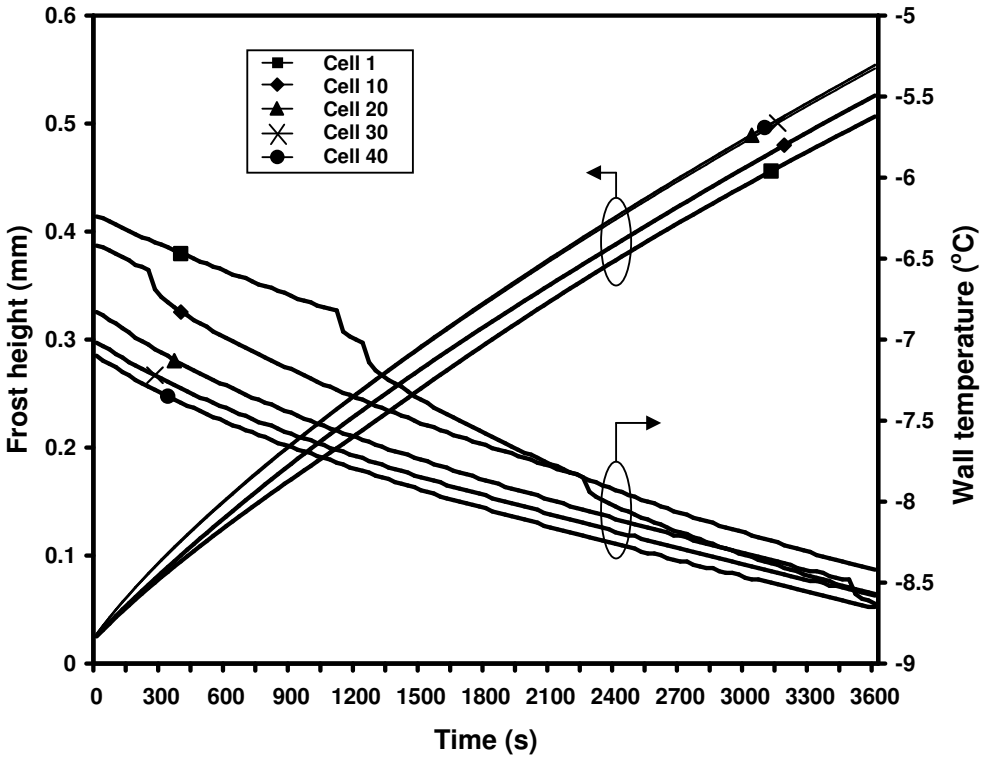

Figure 4.17*: Frost height and wall temperature against time for cells 1, 10, 20, 30 and 40.*

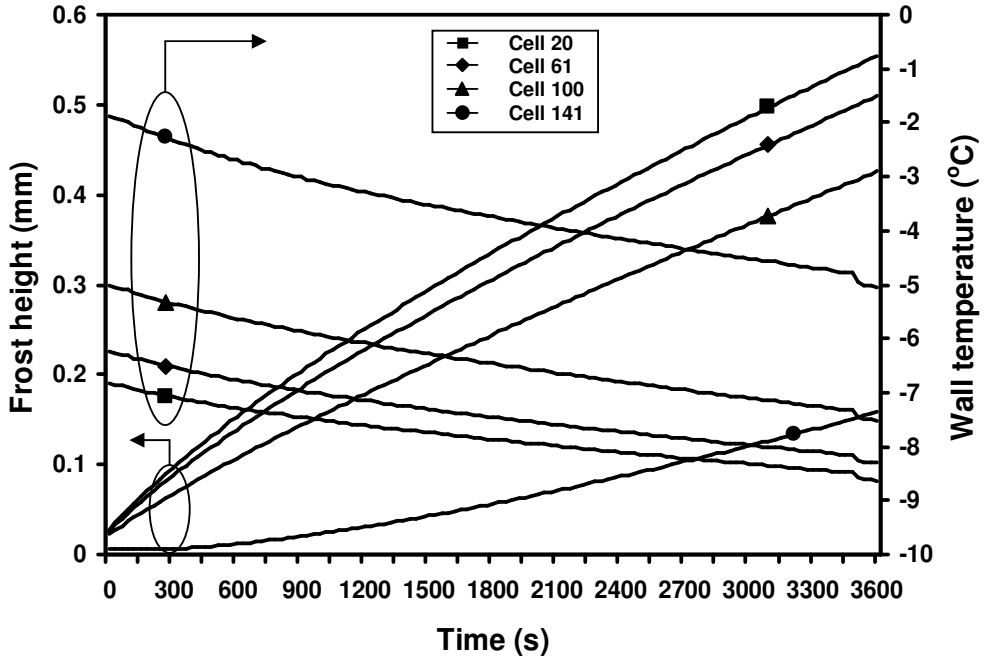

Figure 4.18*: Frost height and wall temperature against time for group 3, i.e. cells 20, 61, 100 and 141 against time***.**

Figure 4.18 shows the variation of frost height and wall temperature at different rows for Group 3 along the coil depth. Note that cells 180 and 221 are not represented, because the wall temperatures of these cells are above the freezing point and hence no frost is formed. The wall temperature at the first row where the refrigerant enters is the lowest and it increases in the following rows. Lower wall temperature increases frost growth and therefore, the first row has the highest frost height, and the lowest at the coil closer to exit. This trend is in agreement with reported experimental data of Aoki et al. (1991), for a heat exchanger with four rows using brine as the working fluid. They reported that the formation of frost layer depends on the cold surface temperature and the air absolute humidity. For parallel flow, where both air and coolant flow in the same direction, the frost is thicker at the

first row, where else in the counter flow both surface temperature and air absolute humidity decrease along the direction of the air flow. The frost thickness at the fourth row, at the coolant inlet, is thicker as compared to the first row, but the difference is not as great as the parallel flow case. In both cases, the row where the coolant entered has the thicker frost layer. However, this is contrary to simulation results in Yao et al. (2004), where, for counter flow, the row with the coolant outlet has more frost.

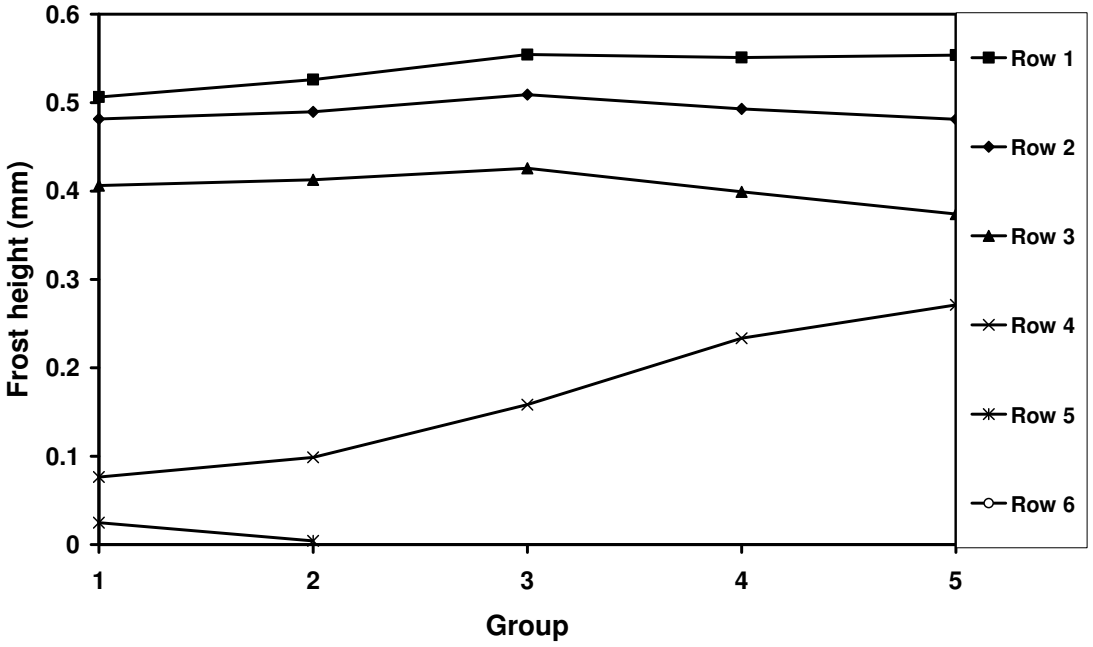

Figure 4.19*: Frost height for selected groups at 3600 s***.**

The frost height at 3600 s for each row for the selected groups can be seen in Fig. 4.19, which shows that the frost height varies within a row and also within a group for different rows. The frost for the first row at the refrigerant inlet is the highest, followed by the second and third row. At the fourth row, the frost height is greater on the right as compared to the left. This is because the frost begins to form first at the right end of the fourth row when the surface temperature reaches freezing

point and continues to grow then, showing the frost propagation along the serpentine coil towards the exit.

4.4 Comparison of Parameter that Affect Frost Growth and Evaporator Performance

Four parameters that affect the frost growth and evaporator performance are selected and varied to study the frost growth and to compare the evaporator performance. The four parameters are air inlet temperature, air humidity, air mass flow rate and fin pitch. The operating conditions are listed in Table 4.4. Refrigerant flow rate, inlet refrigerant vapor quality and pressure are set to be 0.01 kg/s, 0.2 and 200.0 kPa respectively. Other parameters are as given in Table 4.1 unless otherwise stated. The operating condition discussed in Section 4.3 is used as the based condition.

Table 4.4: ***Selected parameter that affect frost growth.***

Condition	Parameter change	Air inlet temperature (^{o}C)	Air humidity (% RH)	Air mass flow rate (kg/s)	Fin Pitch (mm/fin (fpi))
1	Air inlet temperature	3	60	1.14	3.18 (8)
		5			
		7			
2	Air humidity	5	50	1.14	3.18 (8)
			60		
			70		
3	Air mass flow rate	5	60	0.75	3.18 (8)
				1.14	
				1.50	
4	Fin pitch	5	60	1.14	4.23 (6)
					3.18 (8)
					2.54 (10)

4.4.1 Effect of air inlet temperature on frosted evaporator

Three sets of condition are simulated based on inlet air temperature of 3 ^{o}C, 5 ^{o}C and 7 ^{o}C. The effect of air inlet temperature on air outlet temperature, total energy transfer rate, frost accumulation and air pressure drop are compared. The number of cells covered with frost increased from 175 to 207 cells for 3 ^{o}C, from 147 to 180 cells for 5 ^{o}C and from 122 to 156 cells for 7 ^{o}C as shown in Fig. 4.20.

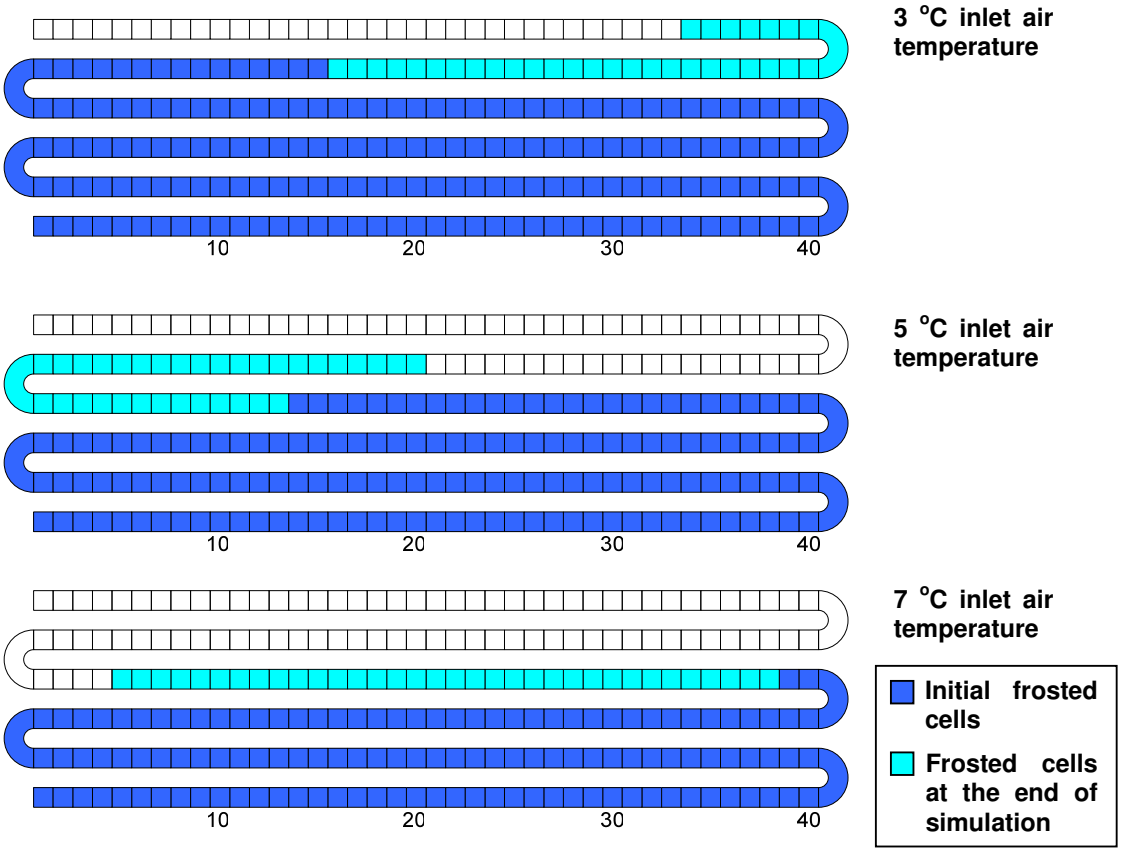

Figure 4.20*: Effect of air temperature on frost distribution.*

Higher air inlet temperature results in higher temperature difference between the air and refrigerant. This also implies that higher air inlet temperature has less frosted area (Fig. 4.20) and higher total energy transfer rate (Fig. 4.21). As time progressed, the formation of frost propagates to the subsequent cells toward the exit of the evaporator due to the insulation effect of frost. This insulation effect reduces the total energy transfer rate. From Fig. 4.21, the total energy transfer rate for inlet temperature of 3 ^{o}C decreases more from 10.59 kW to 10.40 kW as compared to 5 ^{o}C, from 10.75 kW to 10.65 kW, and 7 ^{o}C, from 10.87 kW to 10.81 kW. The reason is because as more area covered with frost, the rate of degradation becomes more severe.

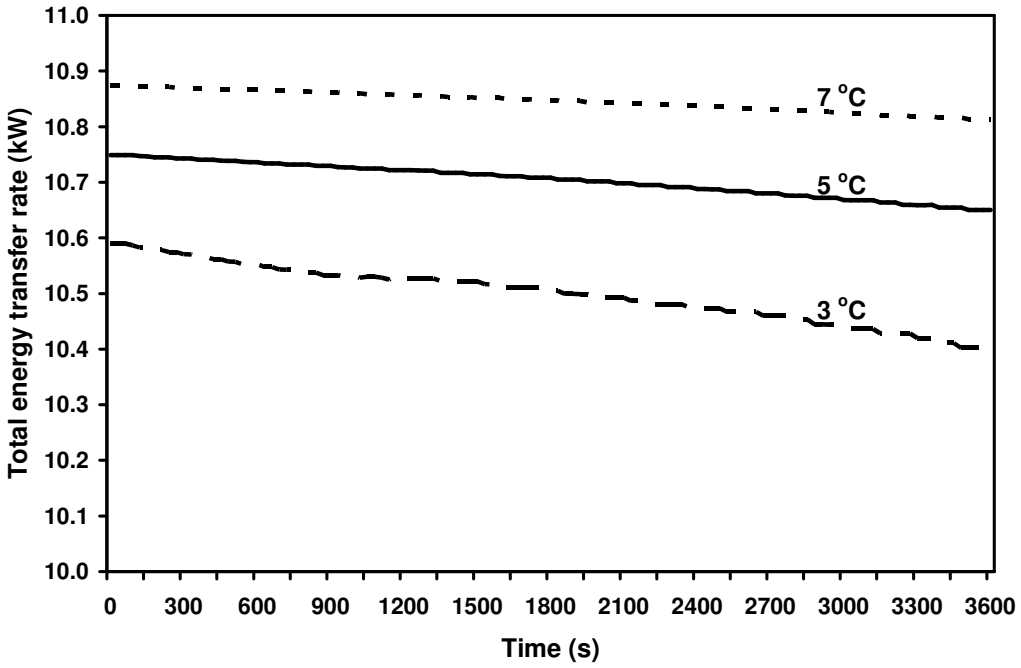

Figure 4.21*: Effect of air temperature on total energy transfer rate.*

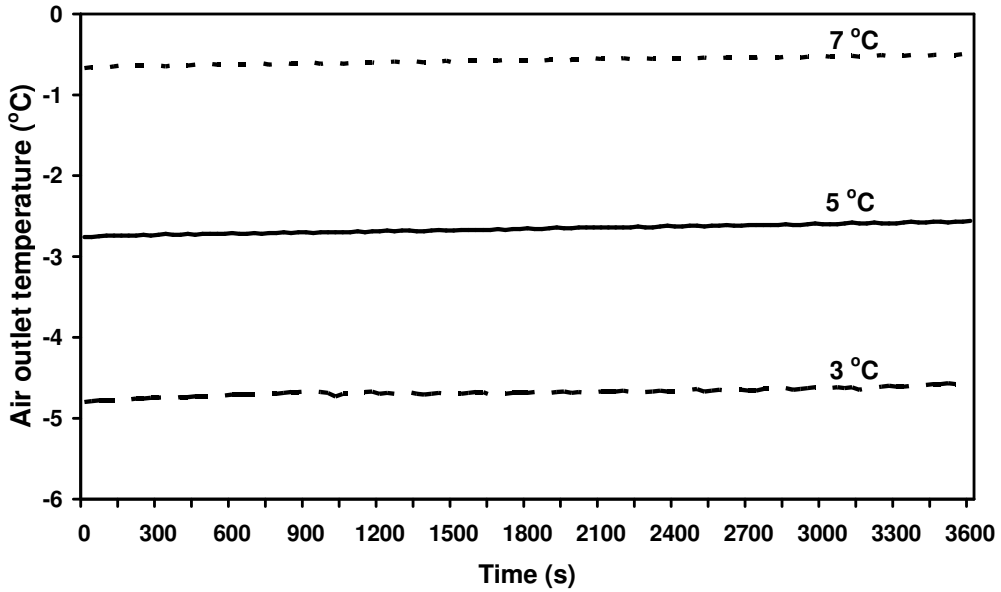

Figure 4.22*: Effect of air temperature on air outlet temperature.*

Evaporator air outlet temperature depends on the condition of the air inlet. The evaporator air outlet temperature gets higher when the air inlet temperature is

high. When frost starts to form and grow on the evaporator, the air outlet temperature tends to increase as shown in Fig. 4.22. The frost acts as an insulation to reduce the heat transfer between the air and refrigerant. All the three conditions show an increase trend with an average temperature of 0.2 ^{o}C by the end of the simulation.

The humidity ratio is higher for a higher air temperature with the same relative humidity. This denotes that the air has higher moisture content for higher air temperature with same relative humidity. Higher air moisture content is favorable for frost growth. From Fig. 4.23, the frost accumulation is highest for inlet air condition of 7 ^{o}C with 3.15 kg of frost accumulated, followed by 5 ^{o}C with 2.83 kg and 3 ^{o}C with 2.36 kg of frost accumulated. This phenomenon is consistent with Tantakitti and Howell (1986) and Rite and Crawford (1991b).

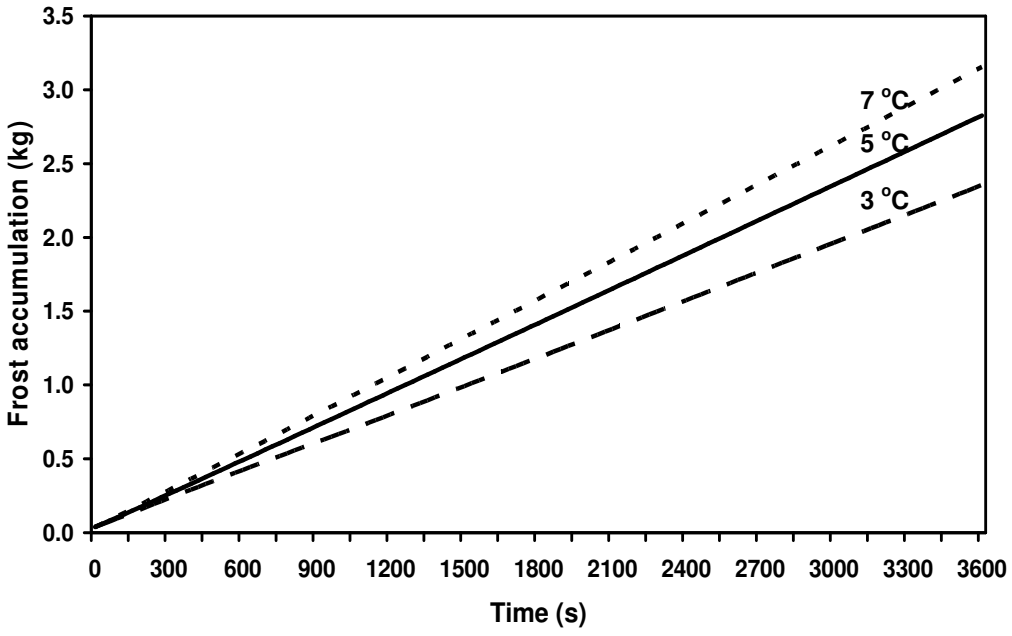

Figure 4.23*: Effect of air temperature on frost accumulation.*

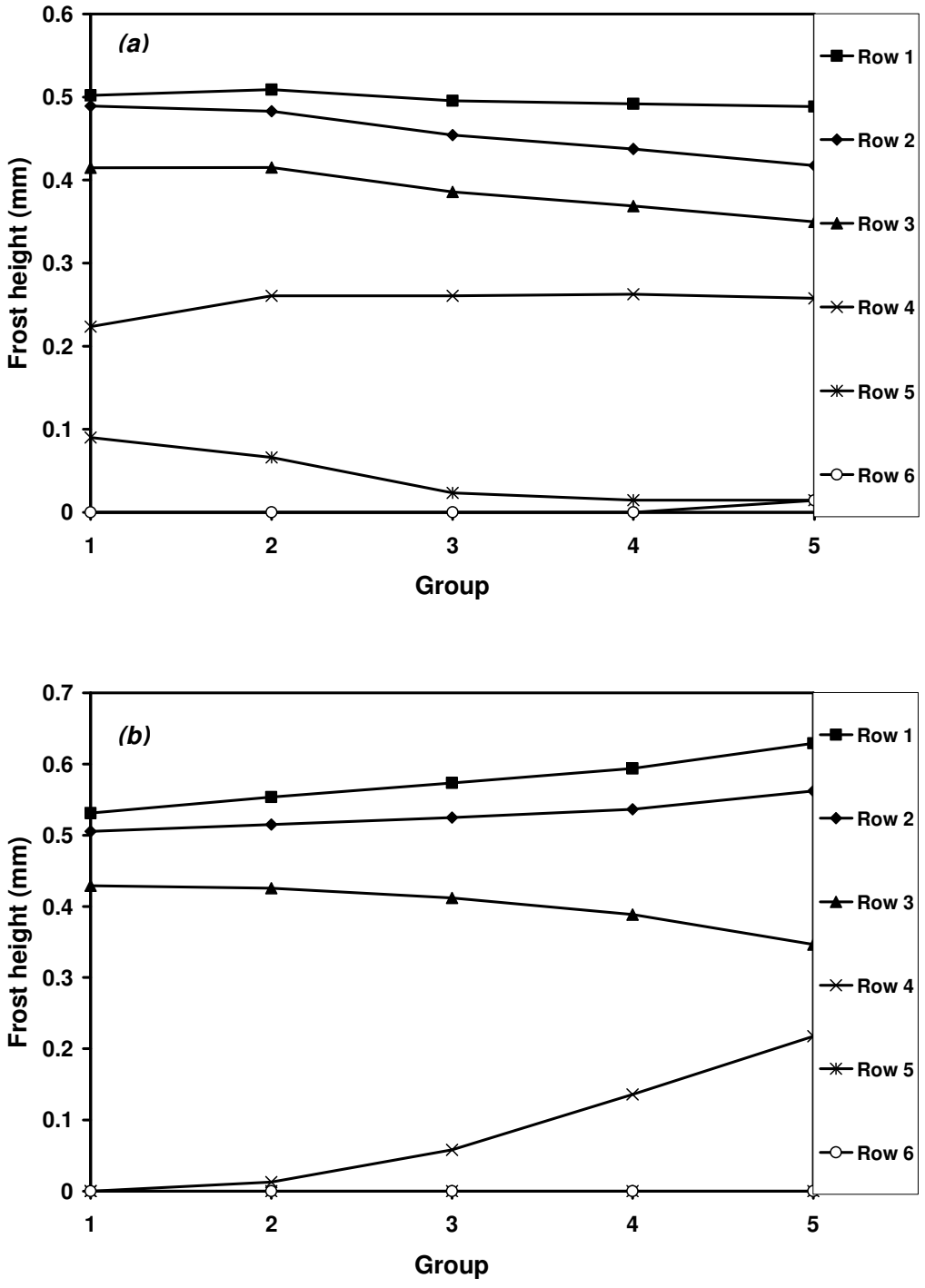

Figure 4.24*: Effect of air temperature on frost height for condition a) 3 °C and b) 7 °C at 3600 s.*

The simulated results for frost height are presented in Fig. 4.24 for condition where inlet air temperature is 3 °C and 7 °C and Fig. 4.19 for 5 °C conditions. The inlet air condition of 3 °C and 5 °C, although have more rows covered with frost as compared with 7 °C condition, the frost height is lower than that of 7 °C condition. The higher the frost height, the less air flow area allows for the air to pass through the evaporator coil. This will also lead to the increase in air pressure drop. From Fig 4.25, it can be seen that the air pressure drop is highest for 7 °C condition with pressure drop of 9 Pa, followed by 5 °C of 6.8 Pa and 3 °C of 5.8 Pa.

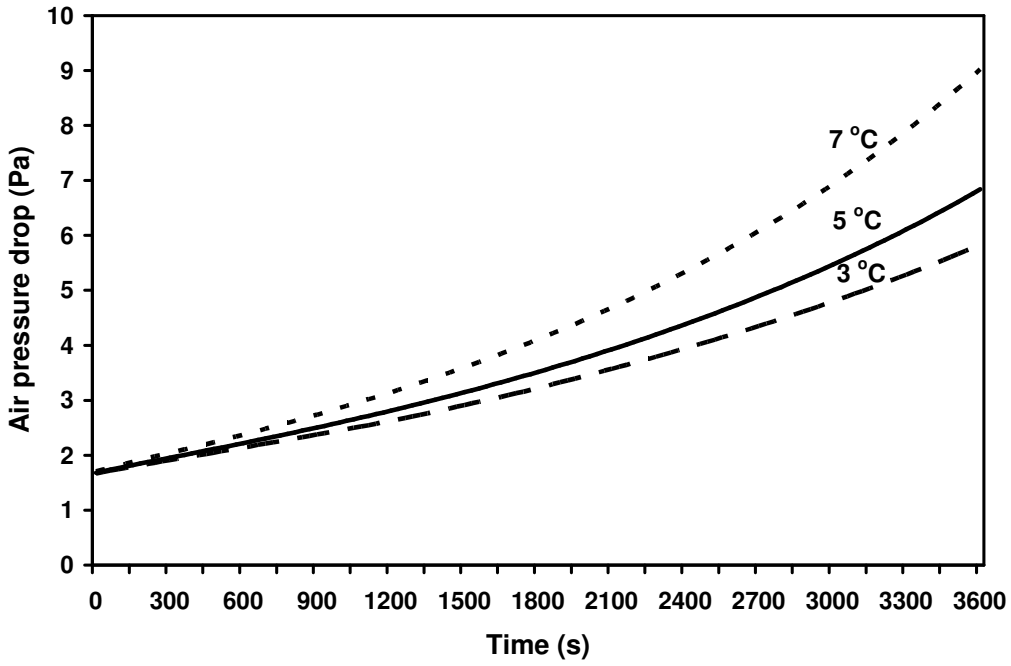

Figure 4.25*: Effect of air temperature on air pressure drop across frosted evaporator.*

4.4.2 Effect of air relative humidity on frosted evaporator

In comparing the effect of air relative humidity (RH) on frosted evaporator, three sets of condition are simulated. The selected conditions are 50 %, 60 % and 70 % with other parameters remained the same as listed in Table 4.4. Fig. 4.26 showed the formation and propagation of frost for different inlet air relative humidity conditions. For condition of 50 % RH, the frost covers 157 cells and increases to 179 cells, for 60 % RH, increases from 147 cells to 180 cells and for 70 % RH, the frost covers from 138 cells and increases to 191 cells by the end of the 3600 s.

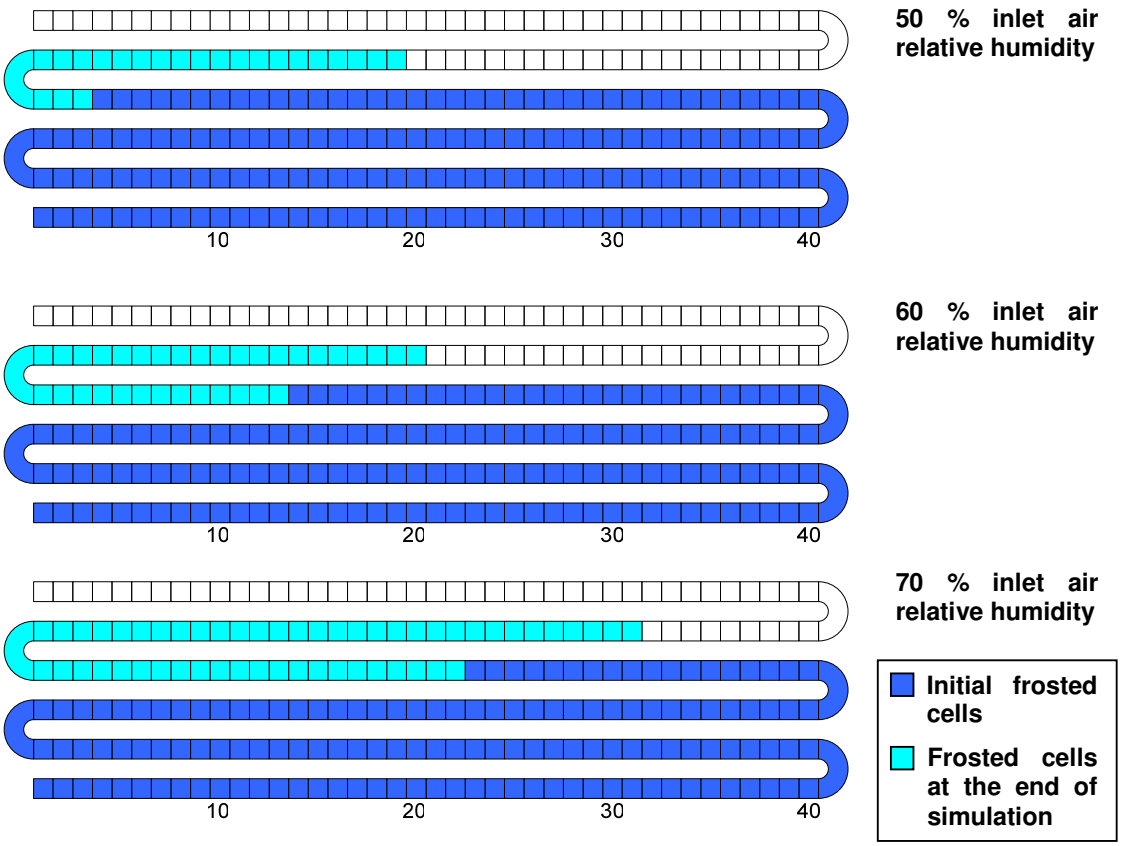

Figure 4.26*: Effect of air relative humidity on frost distribution.*

The higher the air humidity, the more moisture content the air has. Higher humidity leads to more frost formation and growth and consequently a higher frost height and density is formed. As a result, the insulation effect is more serious for higher humidity condition. This causes the rate of frost growth and propagation along the coil is higher for air humidity condition as shown in Fig. 4.26.

Higher air humidity translates into higher latent energy transfer. Therefore the total energy transfer rate across the coil increases. As expected, with the onset of frost growth, the frost forms an insulating layer and the overall energy transfer rate decreases with time more rapidly at higher humidity as shown in Fig. 4.27. The total energy transfer rate for 70 % RH decreases more from 10.76 kW to 10.59 kW as compare to 60 % RH, from 10.75 kW to 10.65 kW, and 50 % RH, from 10.73 kW to 10.65 kW. This decreasing trend agrees with all the results reported by researchers such as Kondepudi and O'Neal (1989) and Ameen (1993).

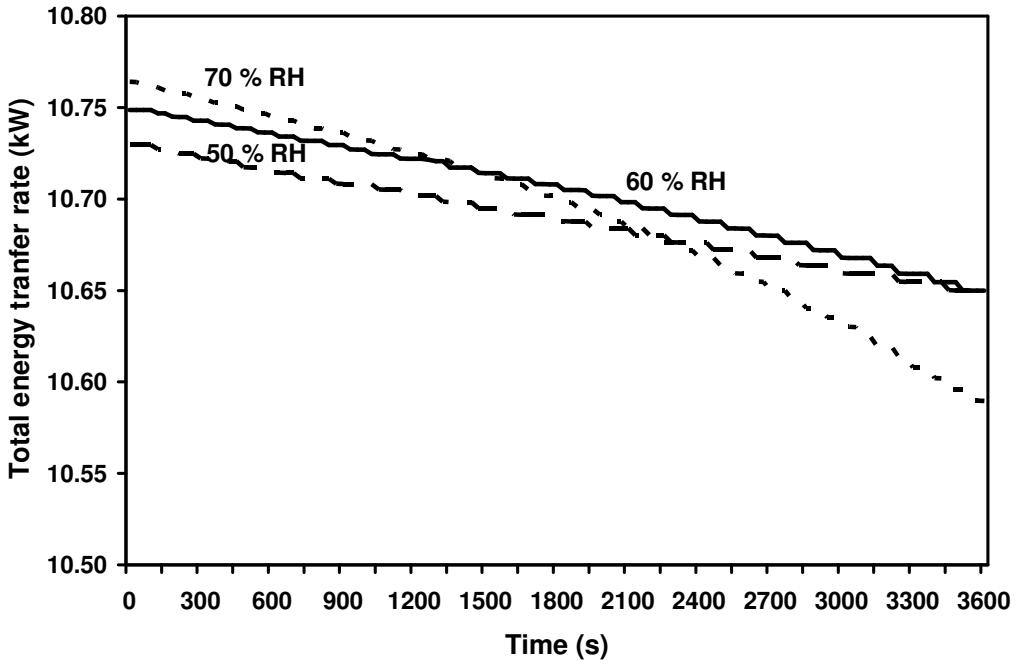

Figure 4.27*: Effect of air relative humidity on total energy transfer rate.*

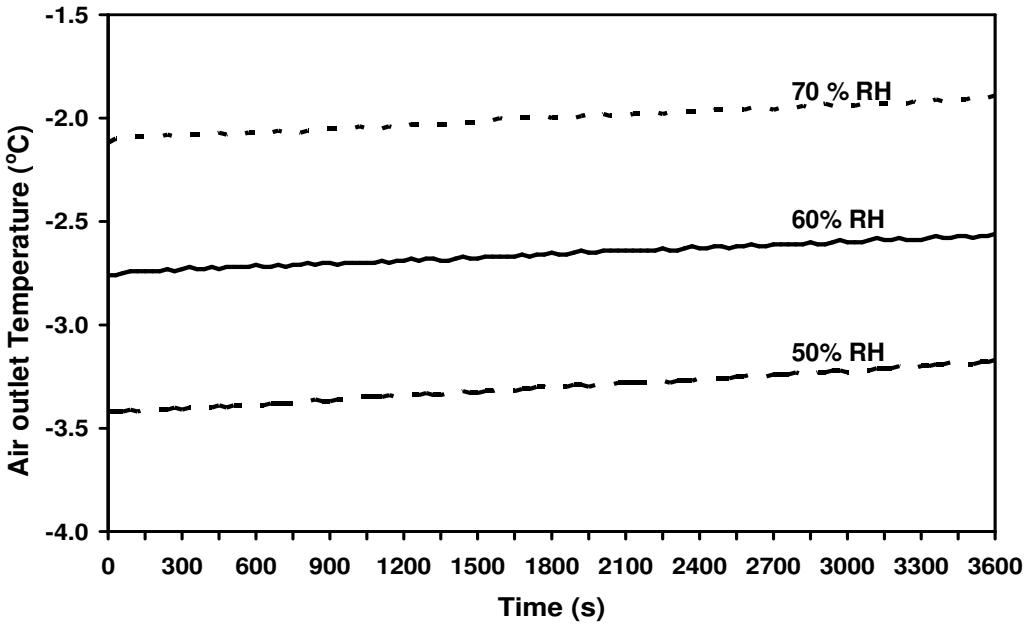

Figure 4.28*: Effect of air relative humidity on air outlet temperature.*

Higher latent energy transfer caused by higher air humidity leads to higher air outlet temperature. The air outlet temperature tends to increase when frost starts to form and grow on the evaporator as shown in Fig. 4.28. The three conditions on the effect of air humidity show an increase trend. The air outlet temperature for 50 % RH increases from -3.42 ^{o}C to -3.17 ^{o}C, for 60 % RH, from -2.76 ^{o}C to -2.56 ^{o}C and for 70 % RH, increases from -2.12 ^{o}C to -1.89 ^{o}C.

The effect of air humidity on the frost accumulation is shown in Fig. 4.29. The frost accumulation is highest for air humidity condition of 70 % RH with 3.93 kg of frost, followed by 60 % RH with 2.83 kg and 50 % RH with 1.35 kg of frost accumulated.

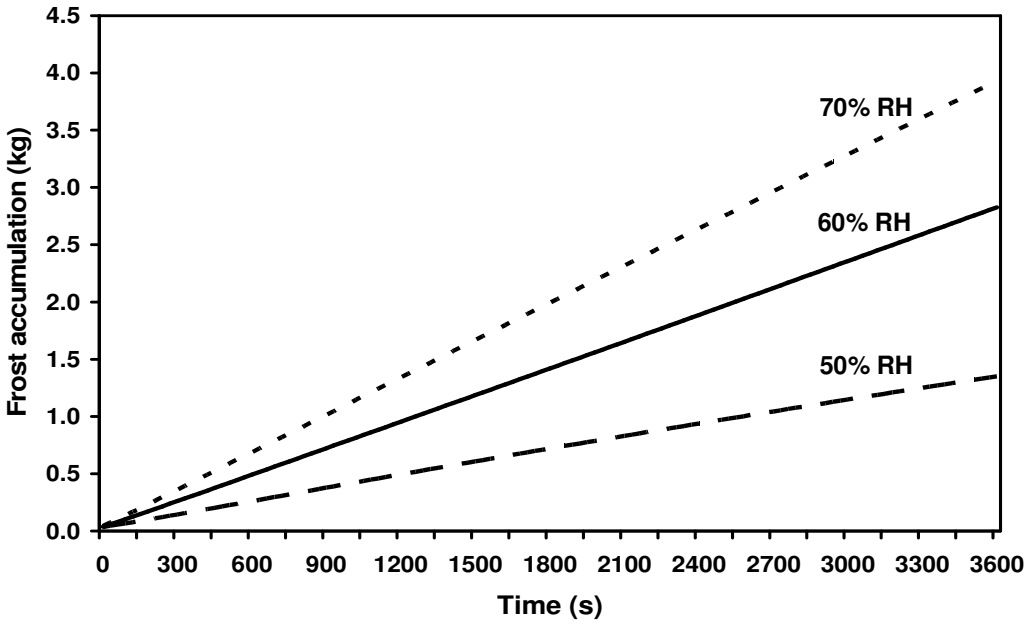

Figure 4.29*: Effect of air relative humidity on frost accumulation.*

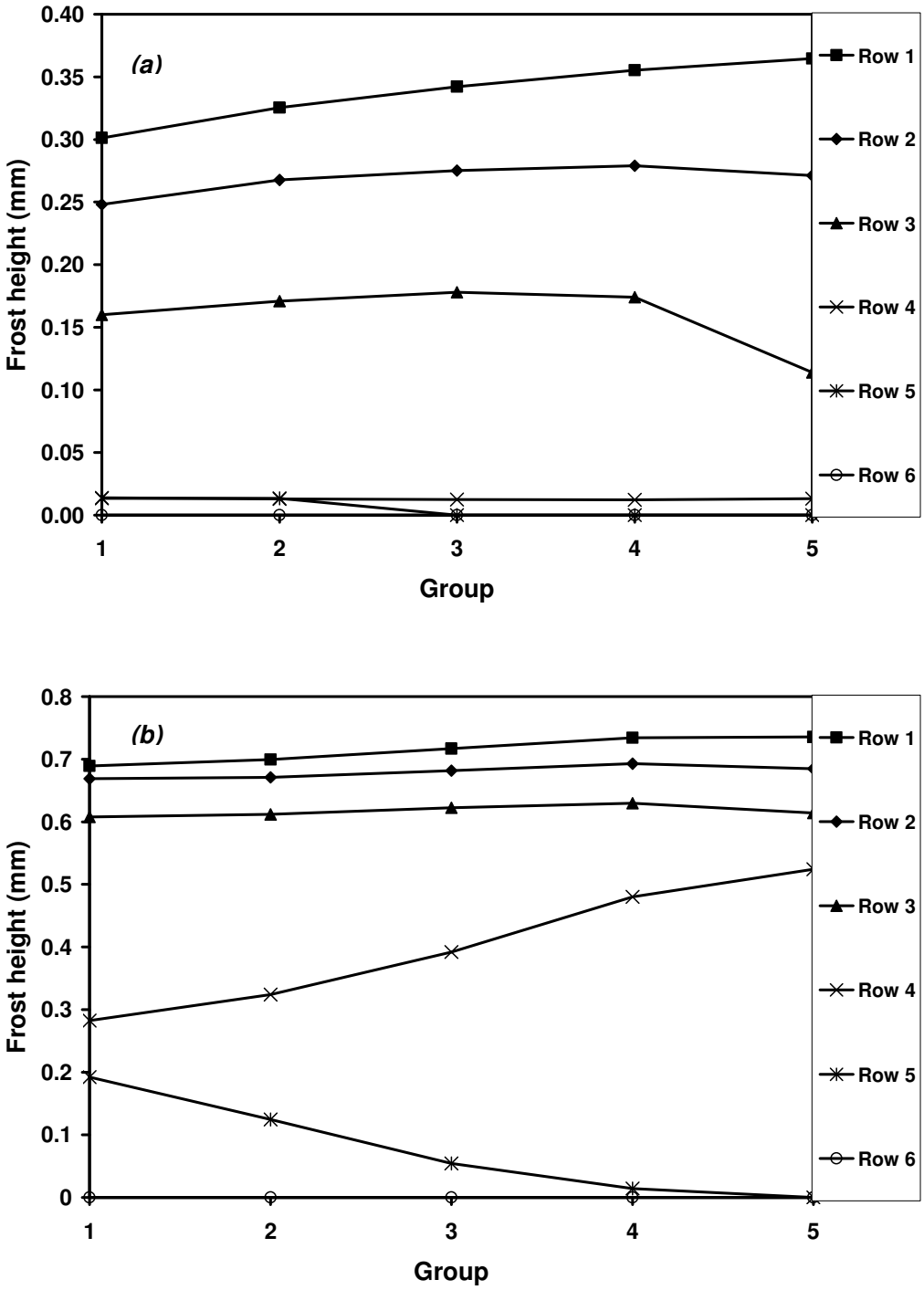

Figure 4.30*: Effect of air humidity on frost height for condition a) 50 % RH and b) 70 % RH at 3600 s.*

The calculated frost height for selected group under air humidity conditions of 50 % and 70 % RH are presented in Fig. 4.30 and for 60 % RH is presented in Fig. 4.19. From the figures shown, it is clear that the frost height is higher when the air relative humidity is high. As the frost height gets higher, the air flow area through the evaporator coil get smaller. It is obvious that the air pressure drop across the coil is highest for 70 % RH condition, followed by 60 % RH and 50 % RH. From Fig 4.31, it can be seen that the air pressure drop for 70 % RH is 13.7 Pa, for 60 % RH is 6.8 Pa and for 50 % RH, the air pressure drop is 3.8 Pa.

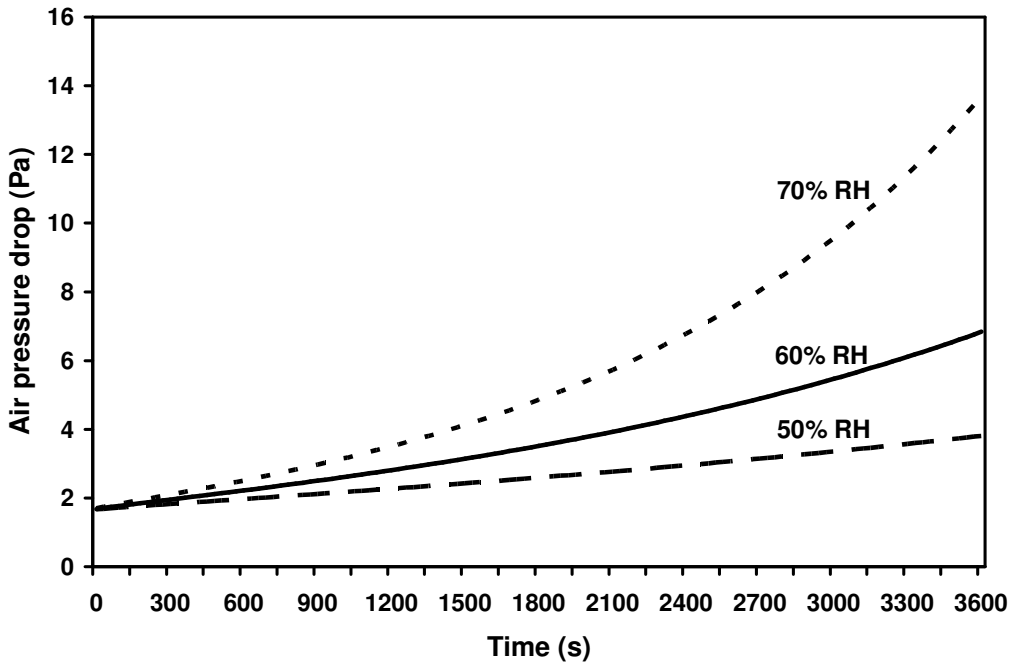

Figure 4.31*: Effect of air humidity on air pressure drop across frosted evaporator.*

4.4.3 Effect of air mass flow rate on evaporator

The baseline condition is compared with the condition where the inlet air mass flow rate decreases to 0.75 kg/s and increases to 1.5 kg/s with other parameters remaining the same as baseline condition. Higher air mass flow rate increase the heat transfer coefficient which will also increase the wall surface temperature. In such condition, the frost formation and propagation is lower for higher air mass flow rate.

As can be seen from Fig. 4.32, the frost formation covers 190 cells initially and propagates to 231 cells by the end of 3600 s for lower air mass flow rate of 0.75 kg/s. For the condition where the air mass flow rate is 1.14 kg/s, the frost increases from 147 cells to 180 cells and for higher air mass flow rate of 1.5 kg/s, the frost covers least cell where it increases from 129 to 155 cells by the end of 3600 s.

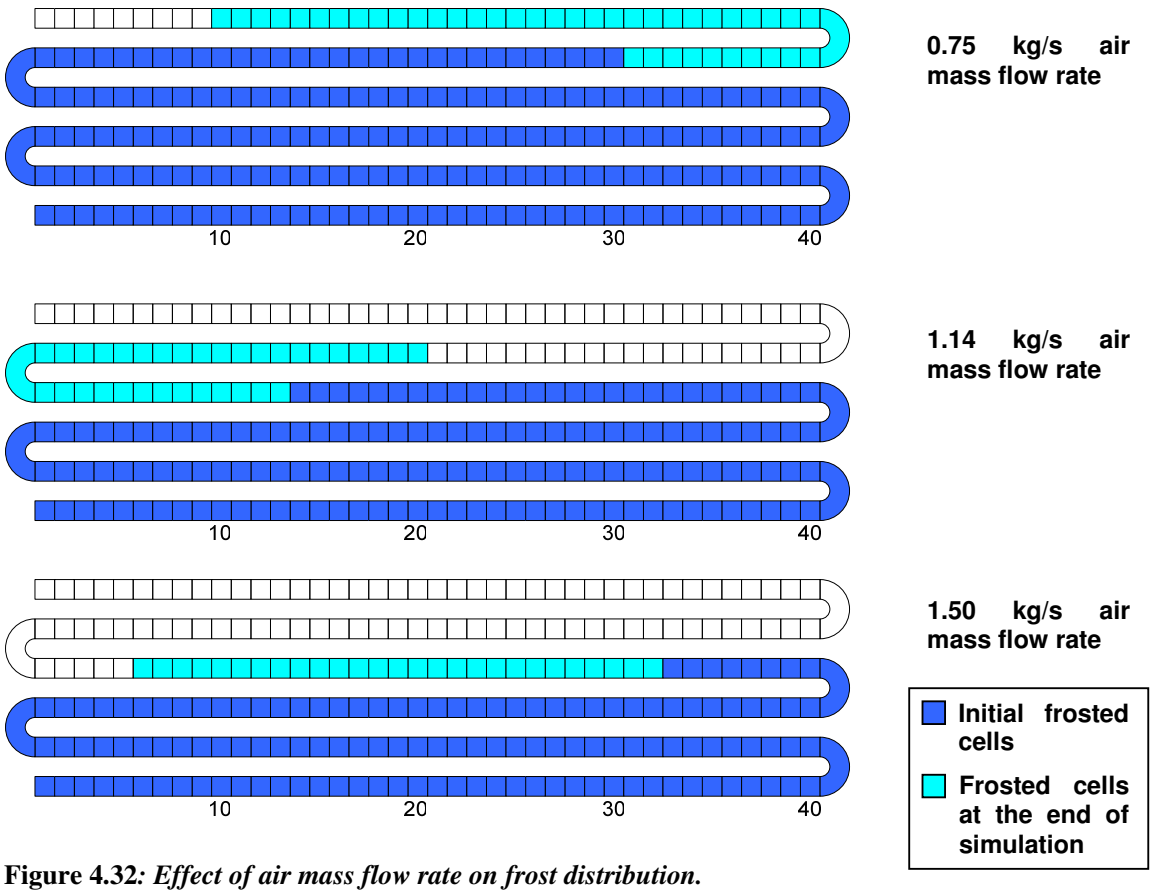

Figure 4.32*: Effect of air mass flow rate on frost distribution.*

Figure 4.33 reflects the effect of air mass flow rate on the total energy transfer rate. A higher air mass flow rate leads to a higher Reynolds Number and hence an increases in the rate of energy transfer. This trend is similar to the trends which can be observed with a dry, unfrosted coil. Such trends have also been reported by Senshu et al. (1990) and Yan et al. (2003). The total energy transfer rate, however, starts to decrease as frost continue to build up and propagate.

From Figure 4.33, the rate of decrease in total energy transfer rate is highest for lower air mass flow rate, 0.75 kg/s, which decreases from 10.58 kW to 10.11 kW. Because of a larger frost accumulation, the frost layer insulates the evaporator quicker and causes the energy transfer rate degraded faster. The total energy transfer

rate for 1.14 kg/s decreases from 10.75 kW to 10.65 kW while for 1.5 kg/s condition, the total energy transfer rate does not degrade much from 10.78 kW to 10.73 kW.

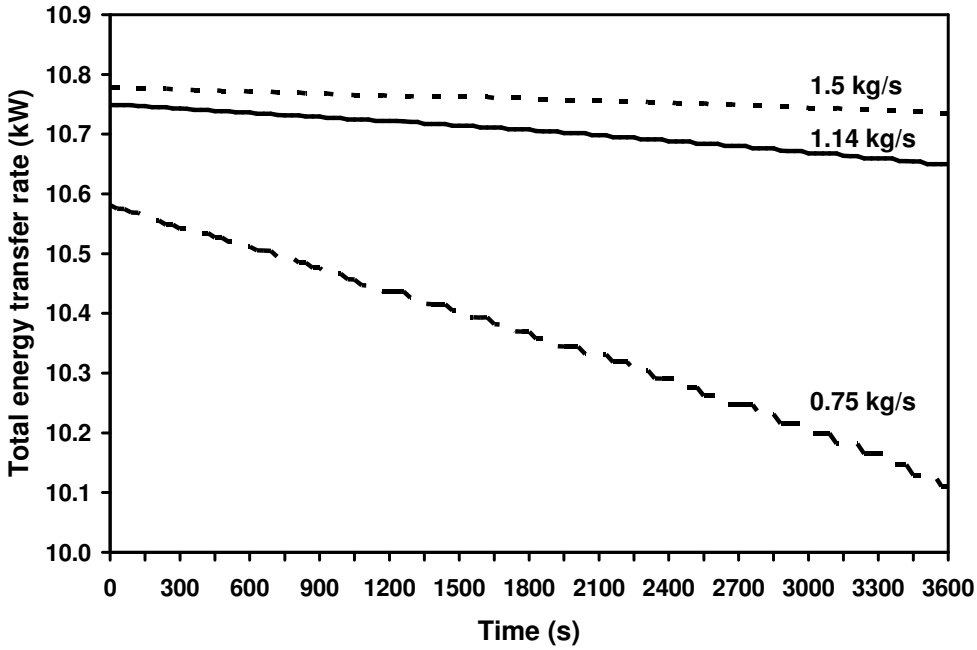

Figure 4.33*: Effect of air mass flow rate on total energy transfer rate.*

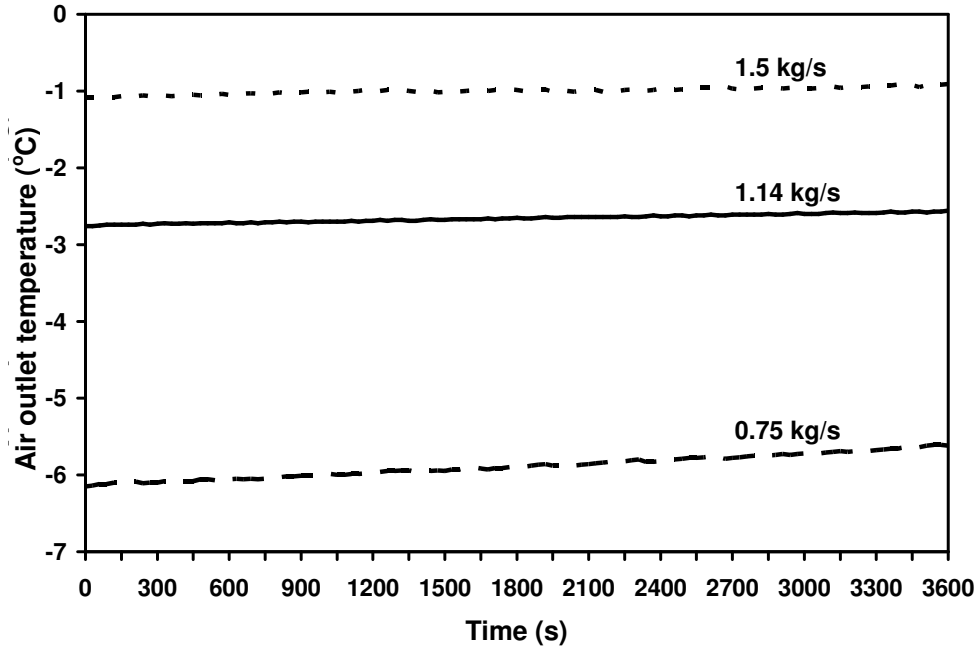

Figure 4.34*: Effect of air mass flow rate on air outlet temperature.*

The effect of air mass flow rate on the air outlet temperature is reflected in Fig. 4.34. As mentioned, higher air mass flow rate has higher heat transfer coefficient and therefore, it has higher air outlet temperature. Due to the insulation effect, the air outlet temperature increases. The condition where lower air mass flow rate, 0.75 kg/s, increases most from -6.15 ^{o}C to -5.62 ^{o}C while for higher air mass flow rate, 1.5 kg/s, increases 0.2 ^{o}C from -1.08 ^{o}C.

The effect of air mass flow rate on the frost accumulation is depicted in Fig. 4.35. The surface of the evaporator, due to lower heat transfer rate, becomes colder for a lower air mass flow rate. A decrease in air mass flow rate results in an increase in the frosting rate. From Fig. 4.35, the frost accumulation is highest for condition 0.75 kg/s with 3.07 kg of frost, followed by 1.14 kg/s with 2.83 kg and 1.5 kg/s with 2.41 kg of frost accumulated.

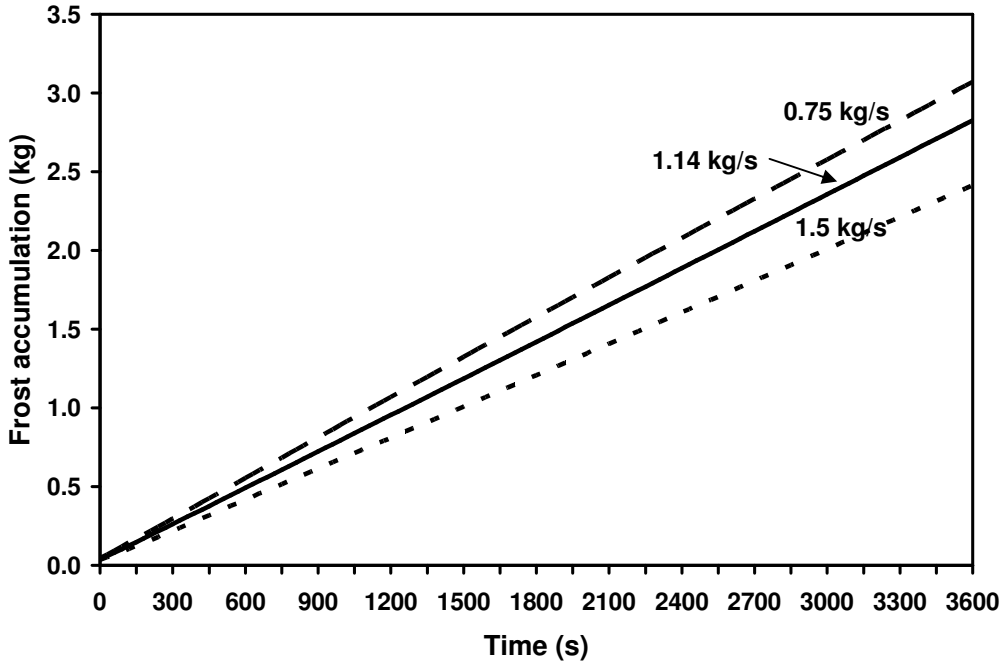

Figure 4.35*: Effect of air mass flow rate on frost accumulation.*

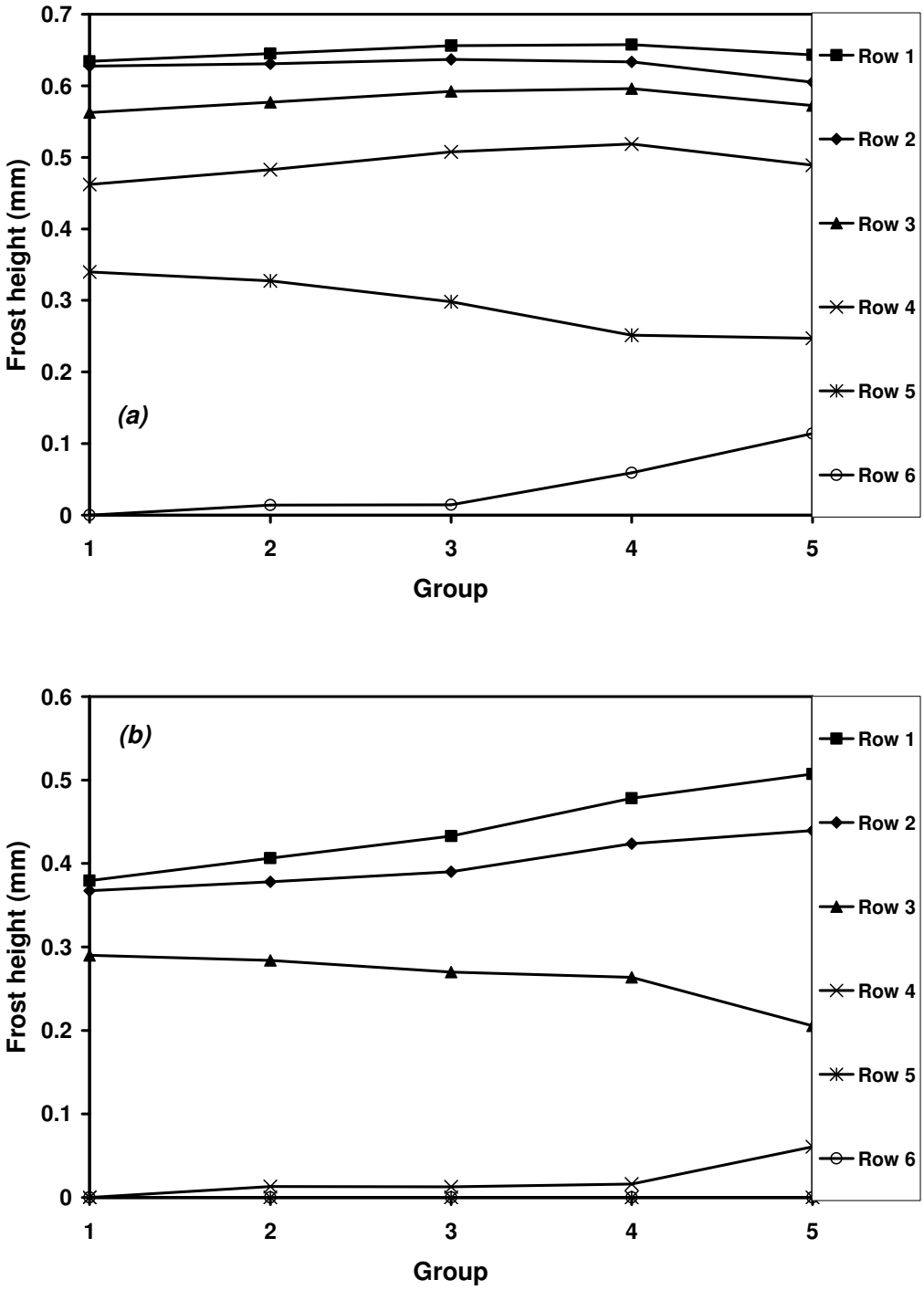

Figure 4.36*: Effect of air mass flow rate on frost height for condition a) 0.75 kg/s and b) 1.5 kg/s at 3600 s.*

In comparing to the frost height for the three air mass flow rate condition, Figure 4.36 shows the condition for 0.75 kg/s and 1.5 kg/s as compared with the base condition of 1.14 kg/s shown in Fig. 4.19. Lower air mass flow rate leads to lower heat transfer rate causing the evaporator coil surface temperature to decrease. The lower surface temperature is favorable to frost growth. As can be seen from the three figures, the frost height is highest for low air mass flow of 0.75 kg/s with average on the first row is 0.65 mm and for 1.5 kg/s, the average height is 0.44 mm on the first row.

The airside pressure drop across coil is related to the air mass flow rate. The higher the face velocity, the higher pressure drop is observed. Although the decrease in air flow passage is higher for low mass flow rate, the pressure drop is dominant by the higher air mass flow rate which is similar to the trend of dry evaporator. The pressure drop, as expected, increases with time as the frost continues to grow. The air pressure drop as shown in Fig. 4.37 for the three conditions are 5.58 Pa, 6.84 Pa and 8.99 Pa for 0.75 kg/s, 1.14 kg/s and 1.5 kg/s respectively at the end of 3600 s.

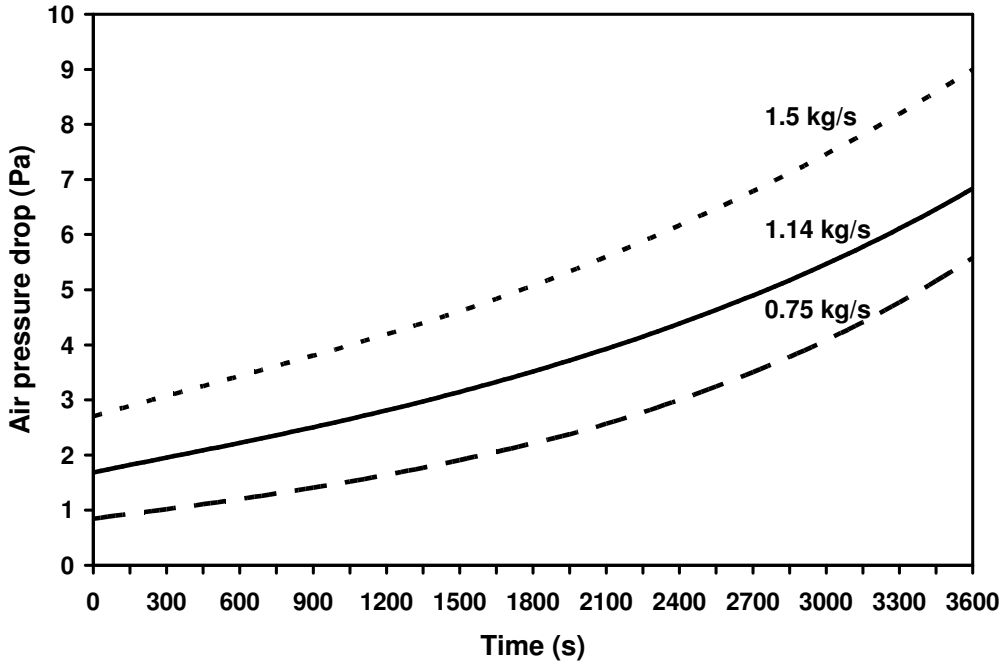

Figure 4.37*: Effect of air mass flow rate on air pressure drop across frosted evaporator.*

4.4.4 Effect of fin pitch on evaporator

Fin pitch on evaporator has influence on the frosting rate of the evaporator. Two different fin pitches are selected and compared with the base condition to study the effect of fin pitch on frosting on an evaporator. The selected fin pitches are 4.23 mm/fin (6 fpi) and 2.54 mm/fin (10 fpi) as compared to the based condition of 3.18 mm/fin (8 fpi).

The greater the fin pitch, the lesser the heat transfer area and less heat transfer rate is resulted. Lower heat transfer rate results in lower surface temperature which encourages the frost to form and grow. Figure 4.38 shows the frost distribution and propagation on the evaporator for different fin pitch. For higher fin pitch of 4.23 mm/fin (6 fpi), the frost covers 169 cells and propagate to cell 205. The lower fin pitch of 2.54 mm/fin (10 fpi) has lowest frost coverage among the three where the frost covers only 132 cells and progress to cell 163.

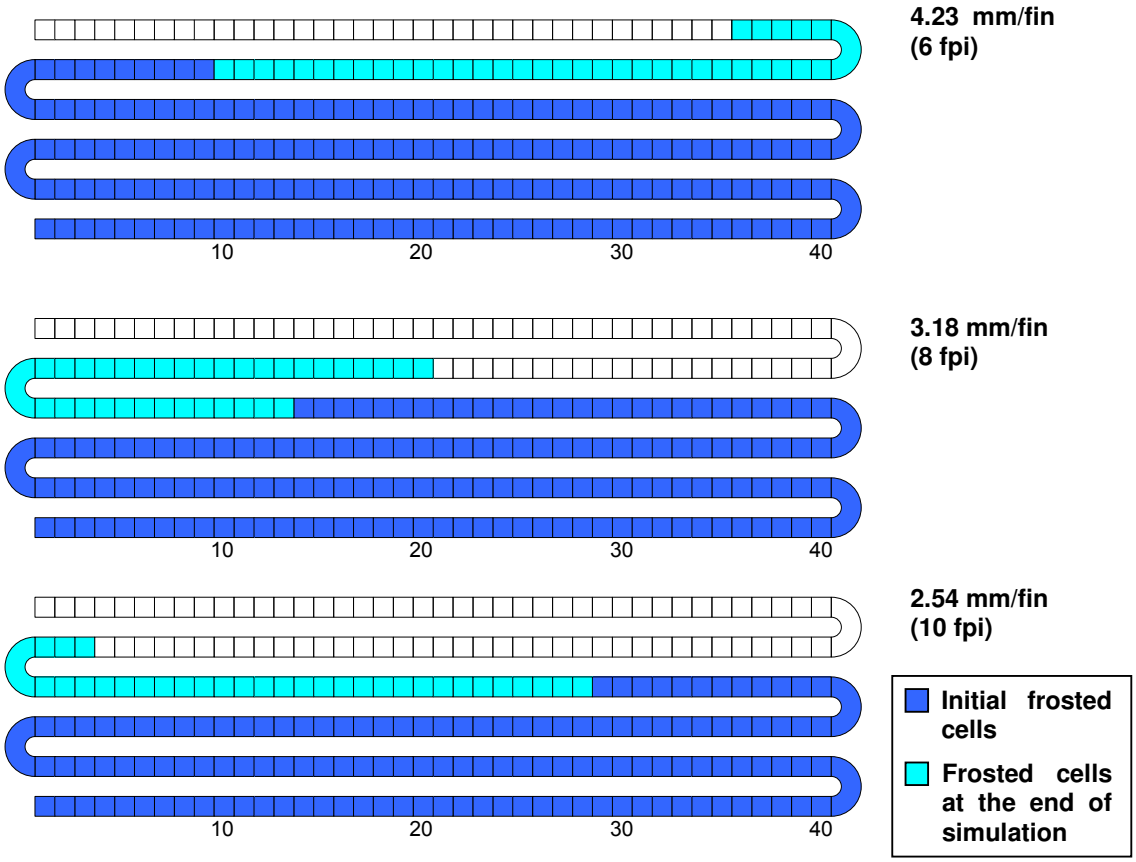

Figure 4.38*: Effect of fin pitch on frost distribution.*

Higher fin pitch has lower overall heat exchange surface area. Less heat exchange surface area leads to lower total energy transfer rate. Lower energy transfer rate causes the wall surface temperature to be lower as compared to higher fin density. As such, more frost grow and propagate faster on higher fin pitch which affect the total energy transfer rate to decrease faster than other.

Figure 4.39 shows the total energy transfer rate for the three different fin pitches. The higher the fin pitch, the lower the energy transfer rate would be. The energy transfer rate for all three conditions degrades with time. The energy transfer rate for 4.23 mm/fin (6 fpi) drops from 10.68 kW to 10.46 kW, from 10.75 kW to 10.65 kW for 3.18 mm/fin (8 fpi) and from 10.77 kW to 10.71 kW for 2.54 mm/fin (10 fpi) at the end of 3600 s.

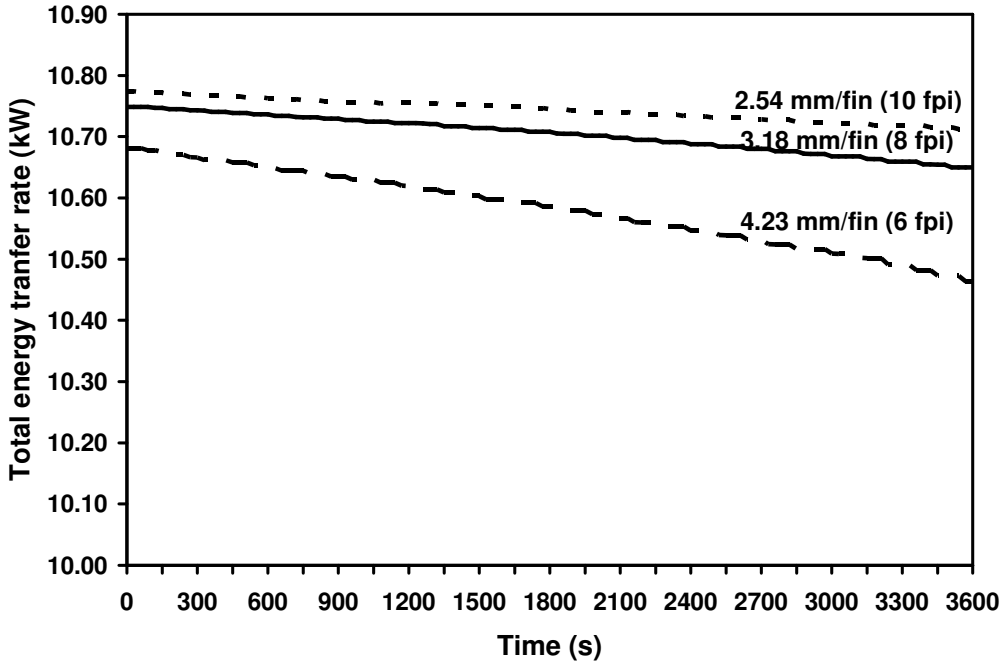

Figure 4.39*: Effect of fin pitch on total energy transfer rate.*

The effect of fin pitch on the air outlet temperature of a frosted evaporator is presented in Fig. 4.40. The overall heat transfer coefficient is higher for an evaporator with a larger fin pitch. This is a consequence of the decrease of the heat exchange area. This is also agreeable with Gatchilov and Ivanova (1979) and Yan et al. (2003). As a result, the air outlet temperature for larger fin pitch has higher air outlet temperature than that of the lower fin pitch condition.

The air outlet temperature increases with time due to the insulation effect. The fin pitch of 4.23 mm/fin increases from -2.58 ^{o}C to -2.35 ^{o}C while for 2.54 mm/fin, the air outlet temperature increases from -2.87 ^{o}C to -2.69 ^{o}C.

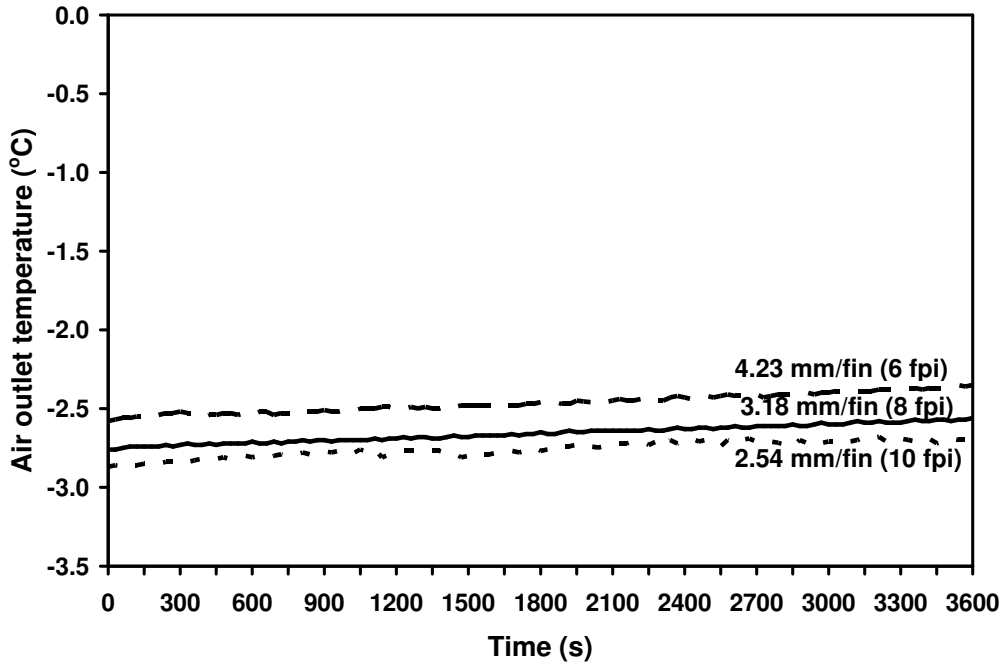

Figure 4.40*: Effect of fin pitch on air outlet temperature.*

The frost accumulation on the effect of fin pitch is shown in Fig. 4.41. The frost accumulation is highest for larger fin pitch condition. This is due to lower energy transfer rate which causes the surface temperature to be lower than the other two conditions. The total frost mass accumulated for condition of 4.23 mm/fin (6 fpi) is 2.93 kg while for lower fin pitch of 2.54 mm/fin (10 fpi), the total frost accumulated is 2.57 kg. The base condition of 3.18 mm/fin (8 fpi) has a total frost accumulated of 2.83 kg.

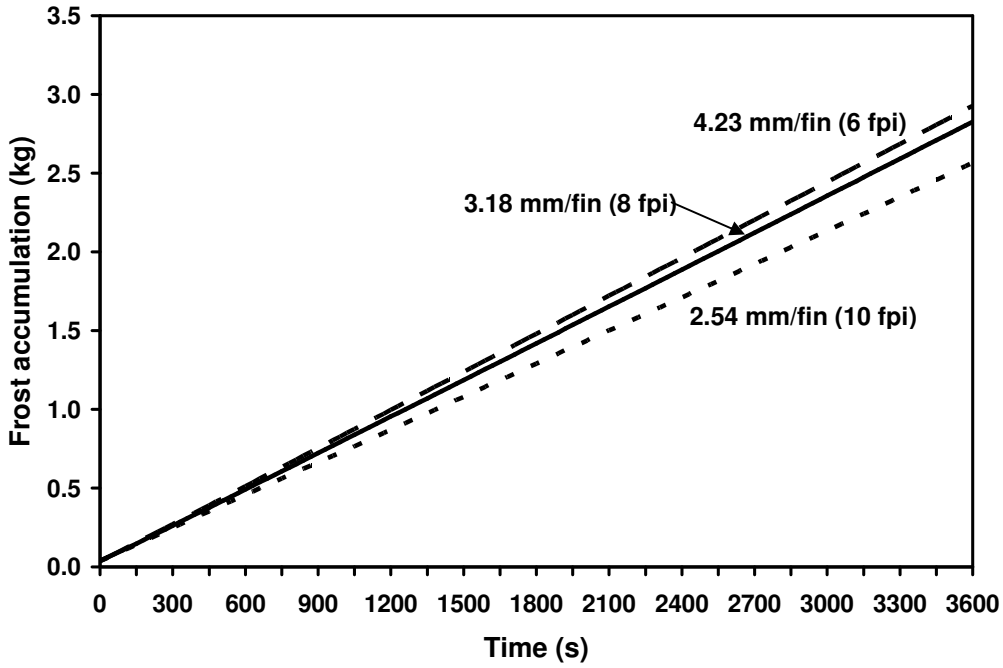

Figure 4.41*: Effect of fin pitch on frost accumulation.*

The predicted frost height for selected groups under fin pitch of 4.23 mm/fin (6 fpi) and 2.54 mm/fin (10 fpi) are presented in Fig. 4.42 and for base condition of 3.18 mm/fin (8 fpi) is presented in Fig. 4.19. From the figure shown, it can be seen that the average frost height for the first row is slightly higher and more rows are covered with frost for condition with larger fin pitch. This is caused by less heat being transferred from the air to the refrigerant and further worsens by the insulation effect of frost.

Although the frost height for larger fin pitch is higher, the air flow area is still larger for larger fin pitch. Figure 4.43 shows the effect of fin pitch on the air pressure drop across frosted evaporator. The air pressure drop for the fin pitch of 2.54 mm/fin (10 fpi) is highest among the three conditions and deteriorates faster than others. The air pressure drop for larger fin pitch of 4.23 mm/fin (6 fpi) increases gradually. From Fig 4.43, it can be seen that the air pressure drop for 4.23 mm/fin (6 fpi) is 3.2 Pa, for 3.18 mm/fin (8 fpi) is 6.8 Pa and for 2.54 mm/fin (10 fpi), the air pressure drop is 20.8 Pa at 3600 s.

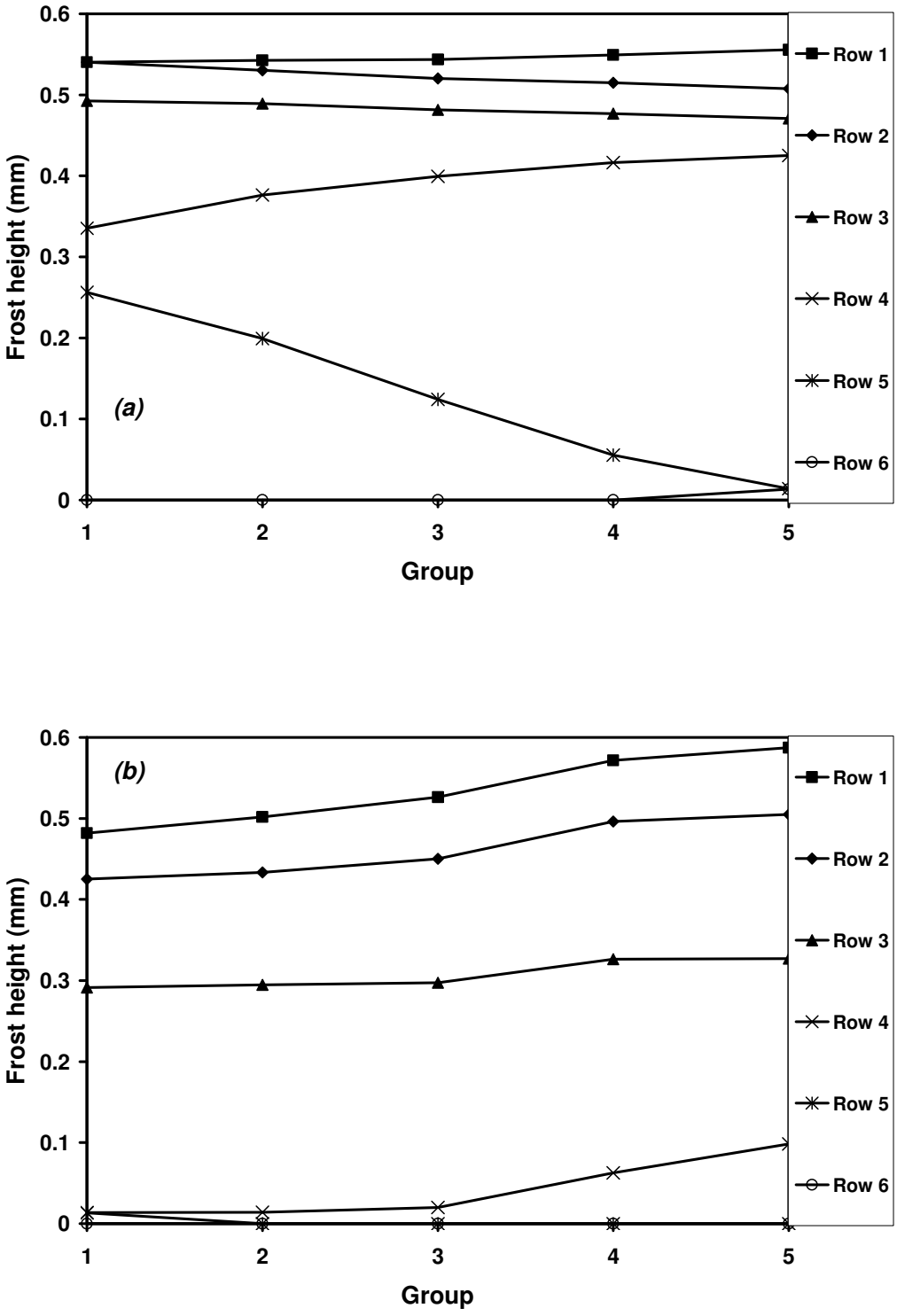

Figure 4.42*: Effect of fin pitch on frost height for condition a) 4.23 mm/fin (6 fpi) and b) 2.54 mm/fin (10 fpi).*

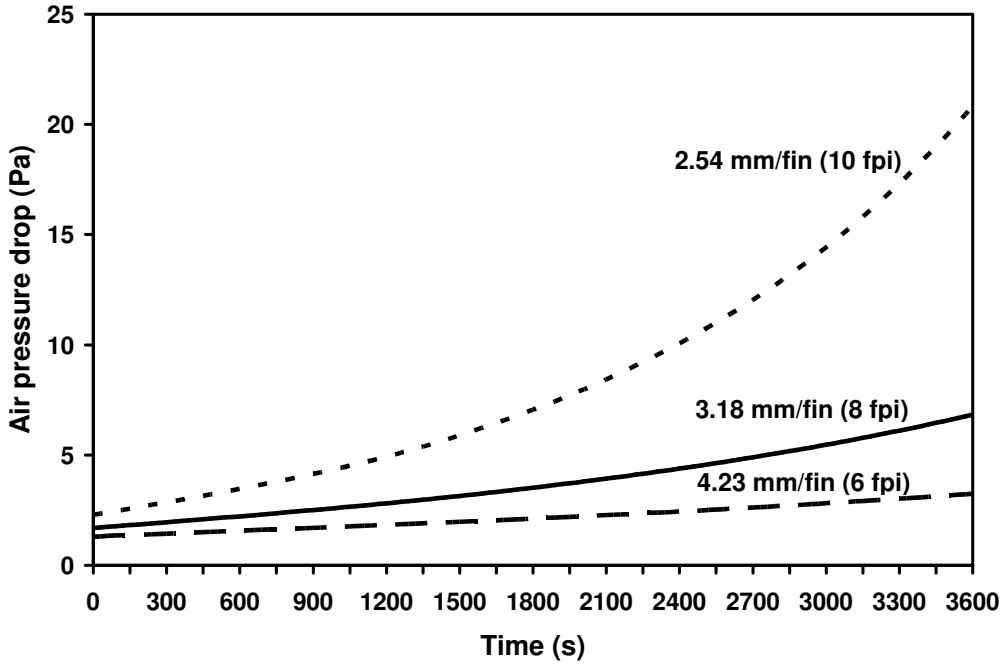

Figure 4.43*: Effect of fin pitch on air pressure drop across frosted evaporator.*

4.5 Comparison of Existing Experimental Data with Model

Kondepudi and O'Neal (1990) reported their experimental data based on single-phase working fluid. Therefore, simulation will be based on their test conditions. The test coil was a single row flat finned-tube heat exchanger as shown in Fig. 4.44. The coil specification is shown in Table 4.5. The working refrigerant was 50% ethylene glycol/water mixture. The operating condition is shown in Table 4.6.

The simulation was performed for the finned tube heat exchanger which was divided into 40 cells per coil numerically using a time-step of 10 s. Parameters

selected for comparison were frost mass accumulation, pressure drop and energy transfer coefficient.

Table 4.5: ***Coil specification (Kondepudi and O'Neal, 1990).***

Description	**Value**
Coil geometry (m)	0.4572 (w) x 0.4572(h) x 0.22 (d)
Fin density (fin per meter)	710
Tubes diameter (mm)	9.525 (OD), 9.195 (ID)
Number of rows	1
Fin type	Flat

Table 4.6: ***Test condition (Kondepudi and O'Neal, 1990).***

Description	**Value**
Inlet air temperature (^{o}C)	0.0
Inlet air relative humidity (%)	80.0
Face velocity (m/s)	0.762
Refrigerant flow rate (liter/min)	24.61
Refrigerant type	50% ethylene glycol/water
Refrigerant inlet temperature (^{o}C)	-15.0

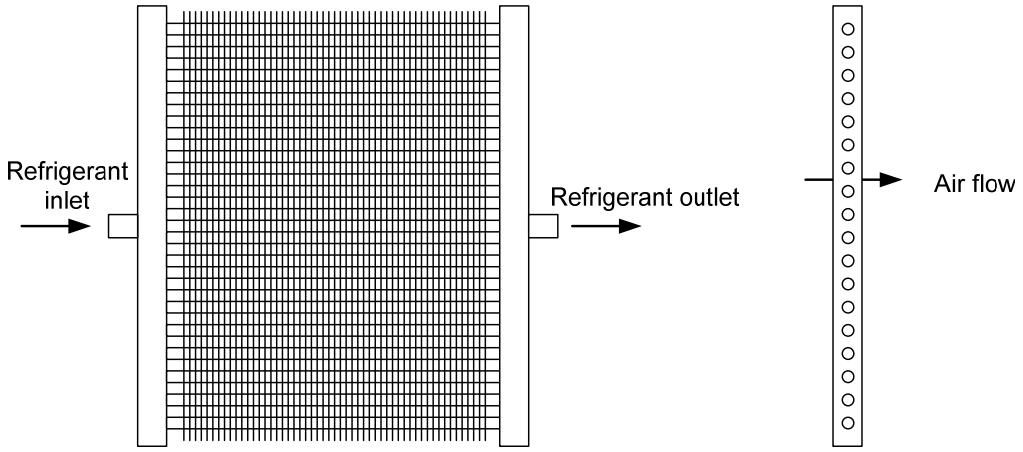

a) Front view of heat exchanger b) Side view of heat exchanger

Figure 4.44*: Schematic diagram of heat exchanger (Kondepudi and O'Neal, 1990).*

4.5.1 Frost growth

The experimental result shows that the mass of frost increases with time. From Fig. 4.45, it can be seen that the mass increases almost linearly with time. Higher value of air humidity, air temperature and lower refrigerant temperature boost the frost growth. For the experiment, the total mass accumulated after 50 min was 0.43 kg. The model predicts similar trend. The predicted mass accumulated at the end of the experiment was 0.46 kg. A total of approximately 7 % discrepancy is found. The present model predicts results closer to experimental results than the simulation results of Kondepudi and O'Neal (1993b).

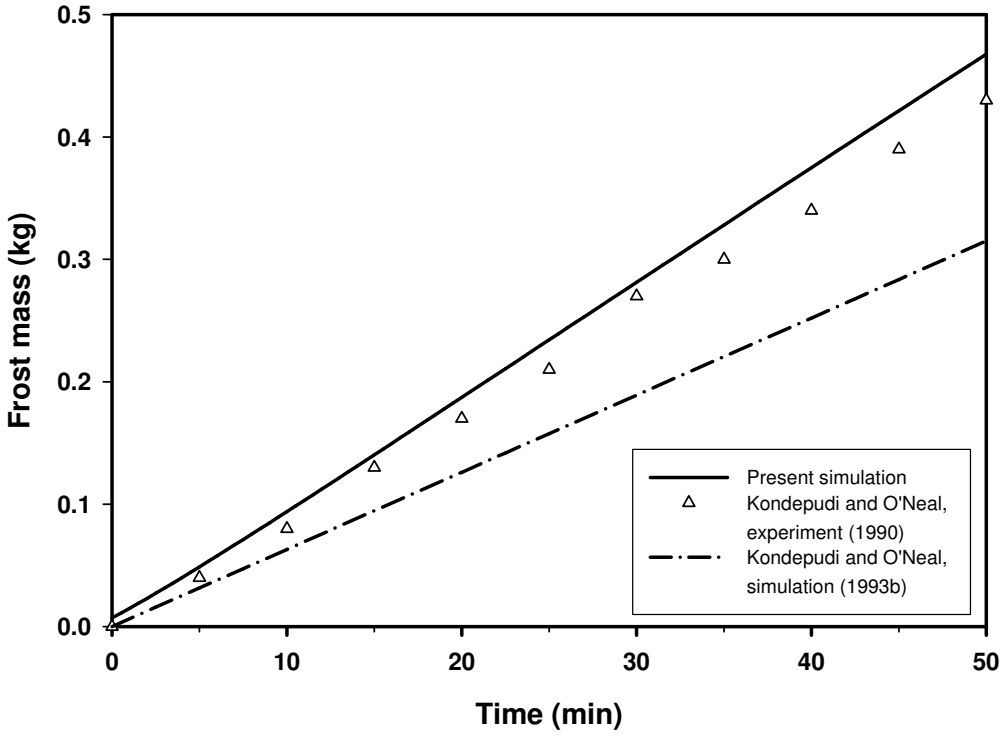

Figure 4.45*: Frost mass accumulation comparison.*

The simulated result reveals that the frost is thicker as it gets closer to the refrigerant inlet point. Fig. 4.46 shows the variation of frost height on tube in the direction of refrigerant flow at 50 min. The calculated frost height at cell 1 is 0.315 mm and at cell 40, it is 0.29 mm. It is found that the difference is about 7.9 %. The wall temperature is colder at the refrigerant inlet and increases as it moves toward the outlet point. The calculated wall temperature at cell 1 is -8.38 ^{o}C and at exit cell 40 is -8 ^{o}C. This phenomenon is agreed with other researchers' findings that frost growth is more rapid with a decrease in the temperature of the heat transfer surface.

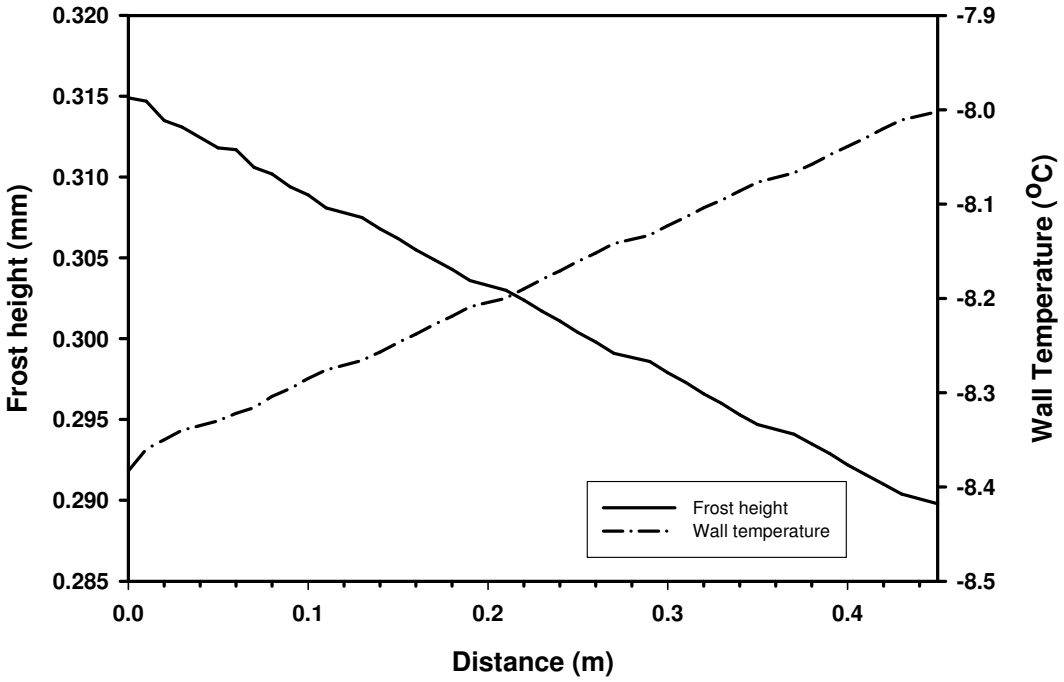

Figure 4.46*: Variation of frost height and wall temperature on tube in the refrigerant flow direction at 50 min.*

The frost height varies along the fin due to the different in fin surface temperature. Table 4.7 shows the variation of fin surface temperature and frost height along the fin. The fin surface temperature is colder at base with temperature of -8.38 ^{o}C and -7.27 ^{o}C at fin tip. The difference between the fin base and tip is about 1.11 ^{o}C. Owing to the difference in wall temperature, the frost height decreases toward the fin tip. The frost height at fin base is 0.315 mm and frost height is 0.239 mm at fin tip.

Table 4.7: ***Frost height variation along fin at time = 50min for Cell 1.***

Node	Distance from base of fin (mm)	Fin temperature (°C)	Frost height (mm)
10	8.57	-7.27	0.2387
9	7.62	-7.28	0.2393
8	6.67	-7.31	0.2412
7	5.72	-7.37	0.2447
6	4.76	-7.44	0.2500
5	3.81	-7.55	0.2571
4	2.86	-7.69	0.2667
3	1.91	-7.86	0.2789
2	0.95	-8.09	0.2945
1	0	-8.38	0.3149

4.5.2 Airside pressure drop across heat exchanger coil

The deposition and growth of frost on the surface of heat exchanger leads to a narrower fin pitch and a smaller air flow passage area. Lower air flow area directly affects the airside condition by increasing the pressure drop across the coil. Variables that affect the frost growth such as refrigerant temperature, humidity and air temperature have influences on the airside pressure drop across the coil. The higher the frost growth rate, the higher the airside pressure drop. Other factors that affect the pressure drop are the fin pitch and face velocity. In the experimental result shown in Fig. 4.47, the airside pressure drop increases with time. The increasing trend is due to the frost height continuing to grow and reduces the air flow passage area. The experimental value for pressure drop increases from 4.9 Pa to 10.77 Pa at

the end of the experiment. The model predicts the same trend. The values are within 8 % between the experimental and model. The present model predicts closer results with experiment, as compared with the model in Kondepudi and O'Neal (1993b).

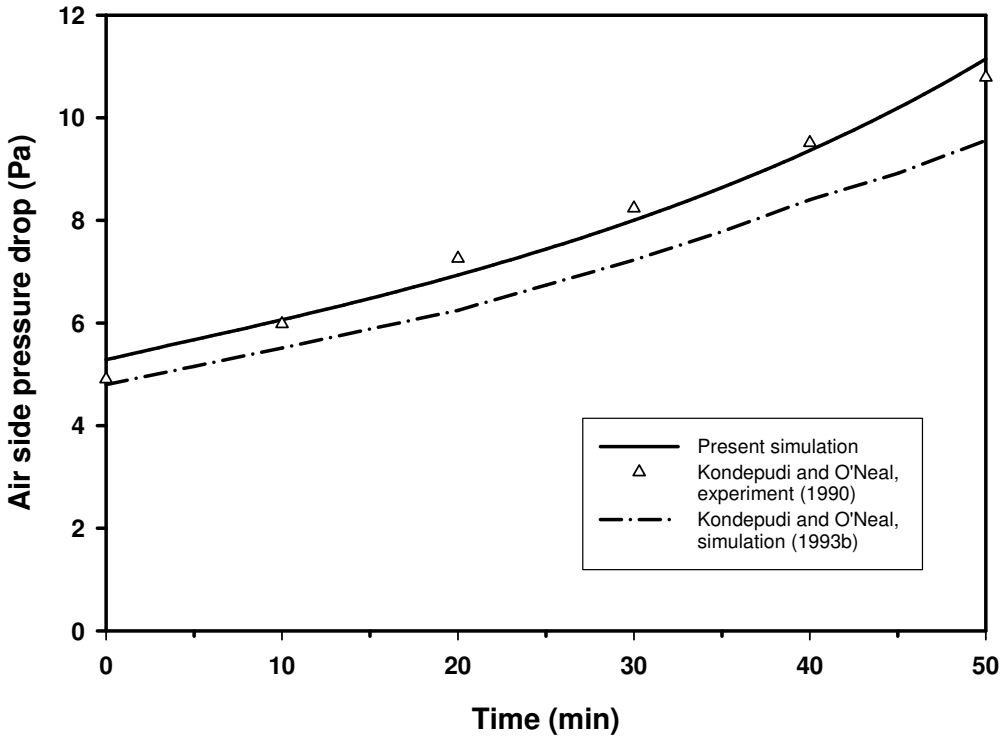

Figure 4.47*: Airside pressure drop across coil comparison.*

4.5.3 Energy transfer coefficient

Kondepudi and O'Neal (1989) in their paper proposed that the energy transfer coefficient, E_o, can be expressed as follow:

$$E_o = \frac{Q.C_{p,a}}{LMED.A} \tag{4.4}$$

where Q is the total energy transferred (W), LMED is the logarithmic mean enthalpy difference (J/kg) and A is the heat transfer surface area (m^2).

The logarithmic mean enthalpy difference (LMED) is defined as follows:

$$LMED = \frac{\Delta h_1 - \Delta h_2}{\ln\left(\frac{\Delta h_1}{\Delta h_2}\right)} \tag{4.5}$$

where $\Delta h_1 = h_{air,in} - h_{ref,out}$

$\Delta h_2 = h_{air,out} - h_{ref,in}$

The proposed energy transfer coefficient is a primary measure of the heat exchanger thermal performance which is similar to the concept of heat transfer coefficient, but it includes the latent component of the energy transfer which occurs between air and heat exchanger. The energy transfer coefficient can be influence by variables that affect frost growth such as humidity, air velocity, refrigerant temperature and air temperature. Other factor such as fin spacing can also affect the energy transfer coefficient. High air humidity, air temperature and low refrigerant temperature will increase the energy transfer coefficient.

The variation of energy transfer coefficient with time for the experimental result is shown in Fig. 4.48. From the graph presented, the model predicts similar

trend as the experimental result and model results of Kondepudi and O'Neal (1993b), which also shows a decreasing trend. The decrease is due to the insulating layer of the frost.

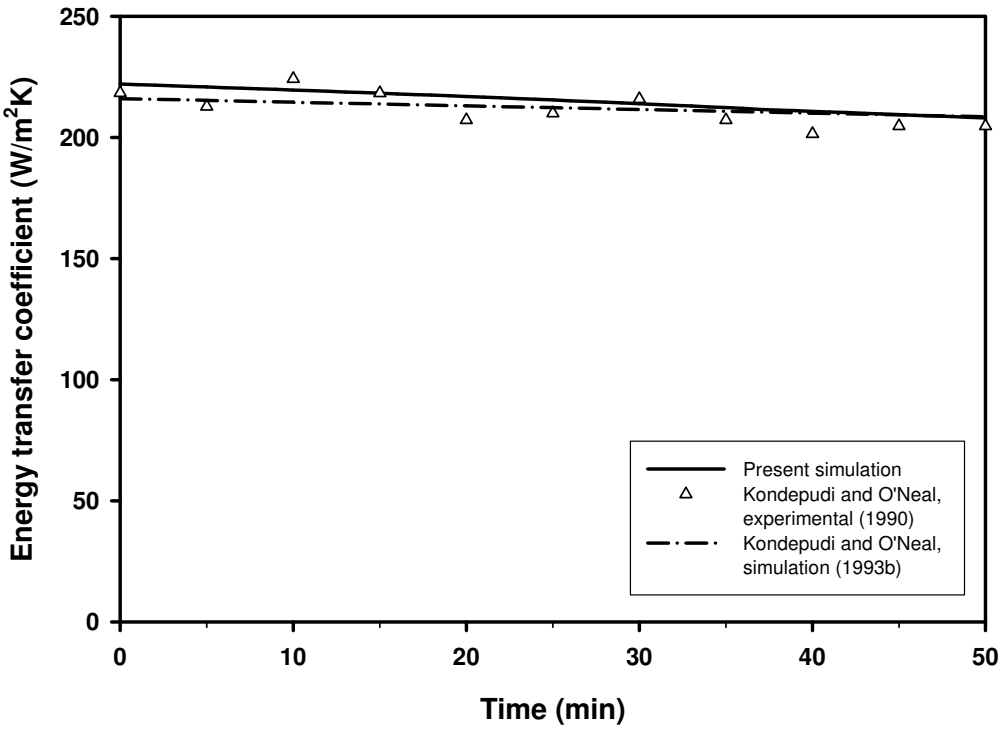

Figure 4.48*: Variation of energy transfer coefficient with time.*

4.6 Conclusion

In this chapter, the numerical simulation results and discussion are presented. The selection of number of cells, convergence criterion, time steps and drift flux model are carried out. The discussion on the results for non-frosted evaporator using volatile refrigerant and the effect of refrigerant liquid dry-out position on the air temperature distribution inside the evaporator is highlighted. The variations of air

and wall temperature have significant influences on the frost deposition on the evaporator.

The discussion continues on the simulated results on frosted evaporator. The effects of the various environmental conditions and fin geometries on frost deposition, energy transfer, air outlet temperature, frost accumulation, frost growth and air pressure drops are presented. The results have been qualitatively compared with what have been reported in literature. In general, the simulated results from the model presented compare well with what reported by other investigators.

The following conclusions can be made.

a) The frost formation is greater at lower air mass flow rate, higher relative humidity, higher air inlet temperature and higher fin pitch.
b) Formation of frost degrades the performance of the heat exchanger.
c) With the increase of frost growth, the total airside heat transfer decreases and the air pressure drop across evaporator increases.
d) The air and wall temperature vary along the tubes and coil which lead to non-uniform frost growth along coil.
e) The temperature along fin varies and this causes uneven frost growth. The frost height at fin base is higher than that at the fin tip
f) The tube row where the refrigerant inlet located, which has lower wall temperature, has more frost accumulation and growth.
g) The frost growth propagates along the tube toward the coil exit.

CHAPTER 5

Field Investigation Results and Discussion

5.1 Description of the field test unit

Refrigerated shipping containers are widely used in transporting and preserving perishable food and biological material. It is an important part of the global cold food chain which accounts for up to 31 % of the world's food supply and has been estimated to grow at an annual rate of about 10 % with the volume of about half a million 20-foot containers in Year 2000 (Jolly et al. 2000). The container temperature can vary from -30 to +20 ^{o}C depending on the type of goods. Operating carriage temperature at below freezing temperature is subjected to frost deposition and progressive build-up on the evaporator coil. The presence of the frost affects the system performance and hence the cargo being cooled. Temperature sensitive products require precise temperature control in the chilled cargo range (Chia et al. 1997) and temperature variation caused by frost deposition and build-up is a parameter to be concerned. However, there is scarcity in the literature about research on containers, especially in modeling and validation of container refrigeration systems under frosting condition. The present study focused on the transient performance of the evaporator under frosting condition for container refrigeration by comparing the numerical results and the field data collected.

Field investigations were conducted on a full-scale refrigerated container at the end of February 2004. A commercial 12.2 m (40 ft) container box consisting of a cargo section and a compactly designed refrigeration system at the front as shown in

Fig. 5.1 was used in the present study. The evaporator is a finned-tube type heat exchanger consisting of nine circuits, six rows of copper tubing and a total of 514 aluminum fins. The outer diameter of the copper tube is 12.7 mm with a thickness of 0.432 mm. The working refrigerant is R-12, and the flow rate is controlled by a thermal expansion valve based on the superheat temperature picked up by the sensing bulb located at the evaporator outlet. Four electric heaters each rated at 750 W and 230 V are located at the bottom air-off coil side of the evaporator for defrosting purpose. The evaporator overall dimensions are 1632 mm long, 286 mm wide and 165 mm high, with a total air side surface area of 44.8 m^2. The air and refrigeration flows are arranged in a counter flow configuration as illustrated in Fig. 5.2. Detailed description of the refrigeration unit is given in Table 5.1.

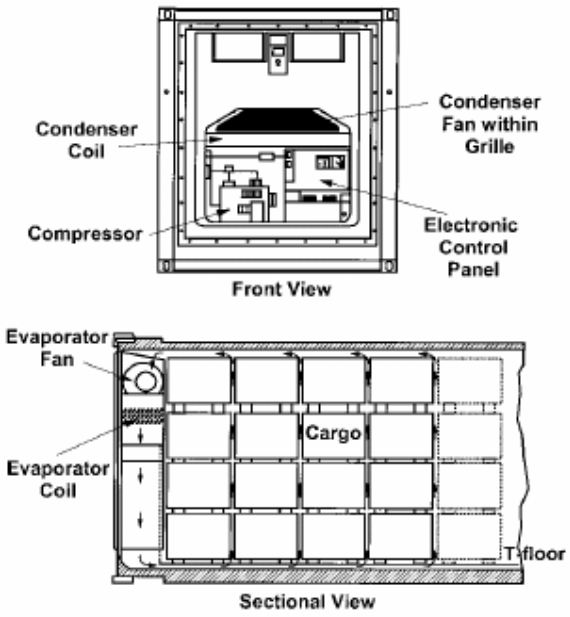

Figure 5.1: ***Views of refrigeration container.***

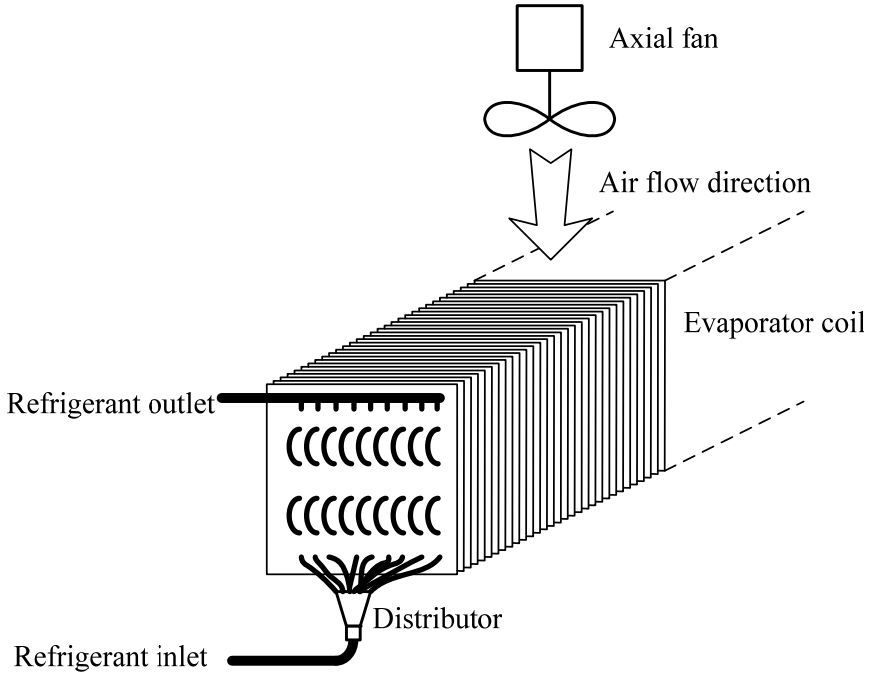

Figure 5.2: ***Schematic views of counter flow type evaporator*****.**

Table 5.1*: Specifications of refrigeration unit*

Item	**Description**
Evaporator	Aluminum finned, 12.7 mm diameter copper tube External dimensions: 1.65 m length x 0.286 m width x 0.165 m height, 6 row x 9 circuits, staggered tubes
Condenser	Copper finned, 7.94 mm diameter copper tube External dimensions: 1.4 m length x 0.3 m width x 0.088 m height, 5 row x 10 circuits, staggered tubes
Compressor	Three cylinder, in-line, 5.6 kW (7.5 hp), suction cooled, semi-hermetic type
Refrigerant	R-12, 5.5 kg
Evaporator fan	2 axial fans
Condenser fan	1 axial fans
Refrigerant expansion device	Thermal expansion valve
Controller	Solid-state microprocessor-based controller

5.2 Description of the measuring unit

The refrigerant mass flow rate was measured by a rotameter. The error on the flow rate was corrected based on a factor provided by the manufacturer and the accuracy estimated to be within ± 2 %. The air flow rate was estimated according to the fan speed and the fan performance curves. Two humidity sensors with an accuracy of ± 3 % were used for measurement on the air on and off the coil and the current signals are outputs to the data logger. Calibrated K-type thermocouples with an accuracy of ± 0.5 ^{o}C were used for measurement of air and refrigerant circuit temperatures. Differential pressure across the evaporator coil was measured with a pressure differential transducer of accuracy ± 1 %. Pressure taps were also located along the coil length at the inlet and outlet, and tubing from these taps were connected to two single tubes and then to the pressure differential transducer. Pressure transducers of accuracy ± 0.25 % were installed to record the dynamic responses of the evaporating and condensing pressures. The sensors deliver a voltage signal that has been calibrated against pressure. The location of thermocouples and pressure transducer mountings are indicated in Fig. 5.3. The measurements were collected through the use of the data acquisition system which was connected to a personal computer. The list of measuring instrument is given in Table 5.2.

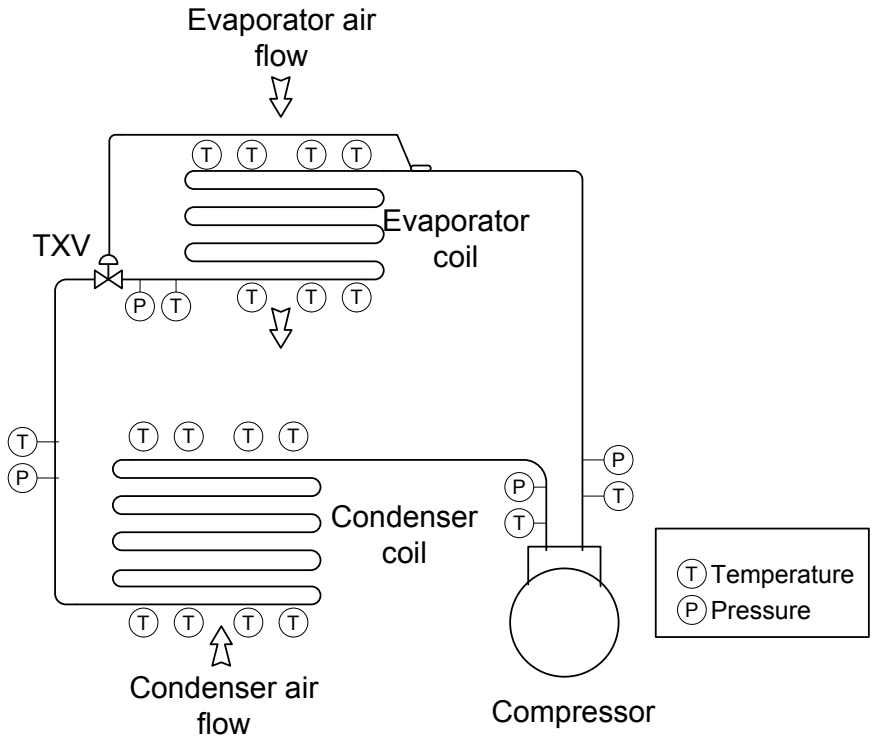

Figure 5.3: ***Schema of locations of thermocouples and pressure transducers mountings.***

Table 5.2*: List of measuring instruments*

No.	Item	Makes	Model
1	Refrigerant flow meter	Krohne	H250/RR/M9/ESK
2	Thermocouples		K type
3	Humidity sensor	GE	MRH-2-D-T
4	Differential pressure transmitter for air side	Setra	M264-2R5WD
5	Refrigerant pressure and temperature transmitter	Measurement Specialist	MSP-310-250PSI-2-N-1 MSP-310-500PSI-2-N-1
6	Steam generator	HT Engineering	HT-S4
7	Weighting machine	Digi	DS-1000
8	Data acquisition unit	Agilent Technologies	34970A

5.2.1 Field procedure

An artificial load generation system was used to provide the system with latent heat load to enable manipulating the moisture content inside the container during the test period. It was supplied with city water and consisted of a 4 kW heater to produce 5.9 kgh^{-1} of steam. The refrigeration system was operated from its initial ambient container condition. The air inside the container was cooled and dehumidified with door closed. When the air temperature reaches around 9.5 ^{o}C, the artificial load generation system was initiated in order to provide the container with sufficient latent heat load to manipulate the moisture content inside the container. The steam was injected into the container at constant flow rate. The observation of the frost growth was carried out by replacing the front metal panel of the evaporator by a clear acrylic window.

5.3 Field observation

There were total three field observations carried out on the container refrigeration. The outdoor temperature for the three observations was in the range of 33 ^{o}C to 35 ^{o}C. The data were collected over a period of more than 3 hours from around 12:30 pm to 3.50 pm. The data collected were made comparisons with the simulated results based on the operating conditions.

5.3.1 Field observation on air side

Three field observations were carried out and the evaporator inlet air temperature and relative humidity for the test period are shown in Fig. 5.4. The air

inlet temperature decreases with time as the space was cooled. The relative humidity of air increases as the air temperature decreases, since lower air temperature has less moisture-holding capacity. There was a hike in the air relative humidity and the rate of decrease for air inlet temperature reduced at around 2950 s for observation 1 (Fig. 5.4 (a)), around 2730 s for observation 2 (Fig. 5.4 (b)) and around 1830 s for observation 3 (Fig. 5.4 (c)). These hikes were due to the commencement of the artificial load generation system when the air temperature reaches around 9.5 ^{o}C, in order to provide the container with sufficient latent heat load for manipulating the moisture content inside the container. The air inlet temperature continues to decrease while the air inlet humidity increases. It can be observed on the air inlet temperature for all three observations that, after 8500 s, there was a minimum temperature existing around 2.5 ^{o}C, probably due to the frost blockage that reduces air flow and heat transfer.

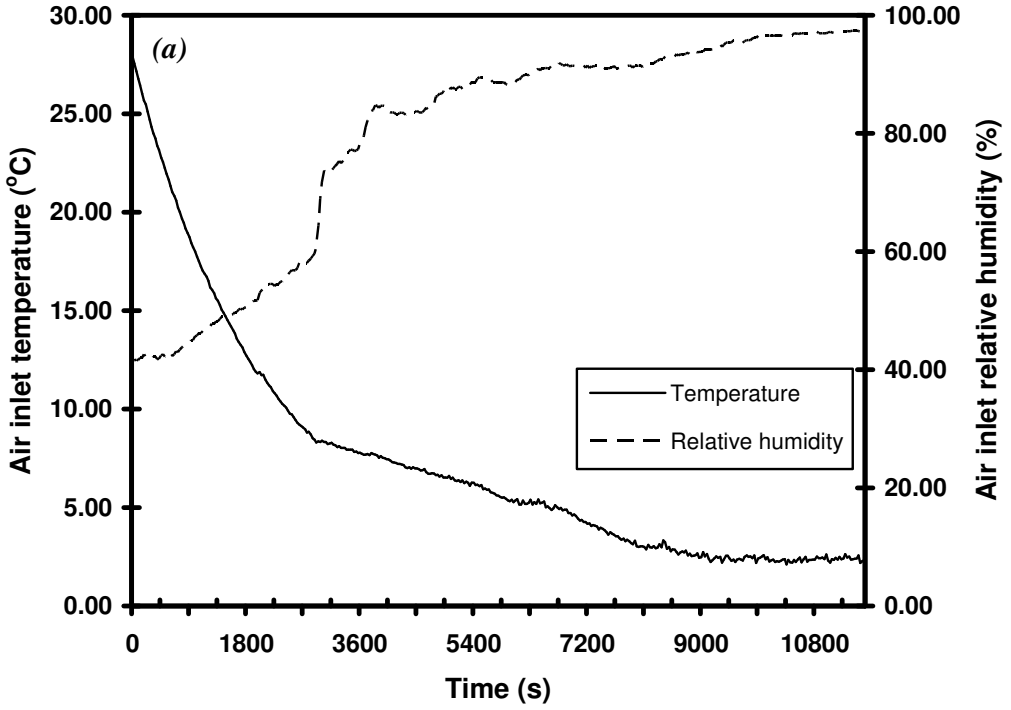

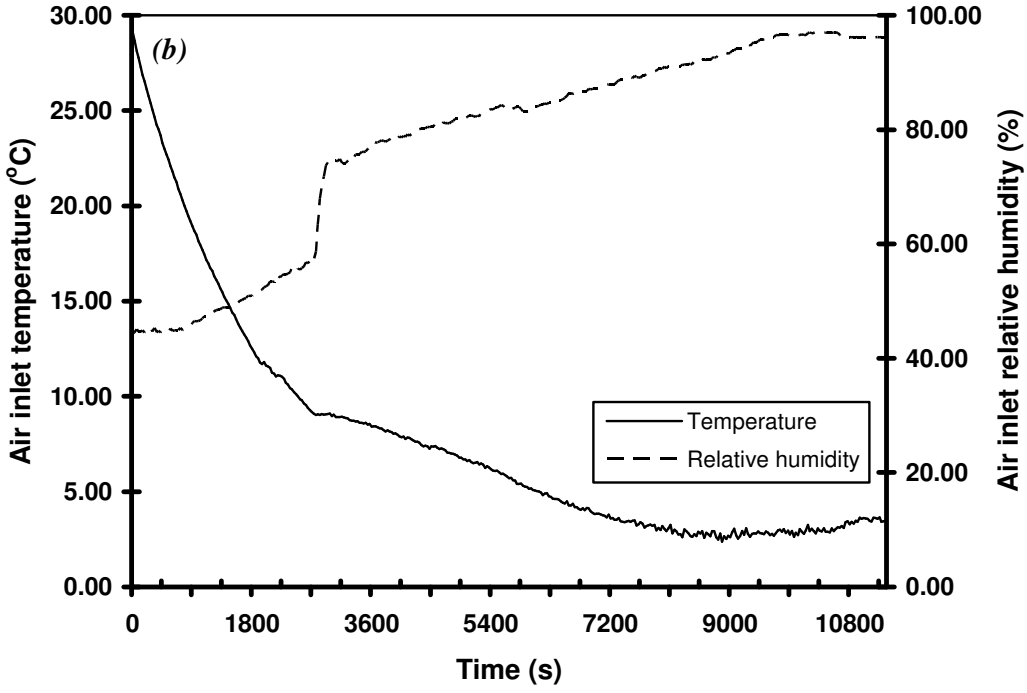

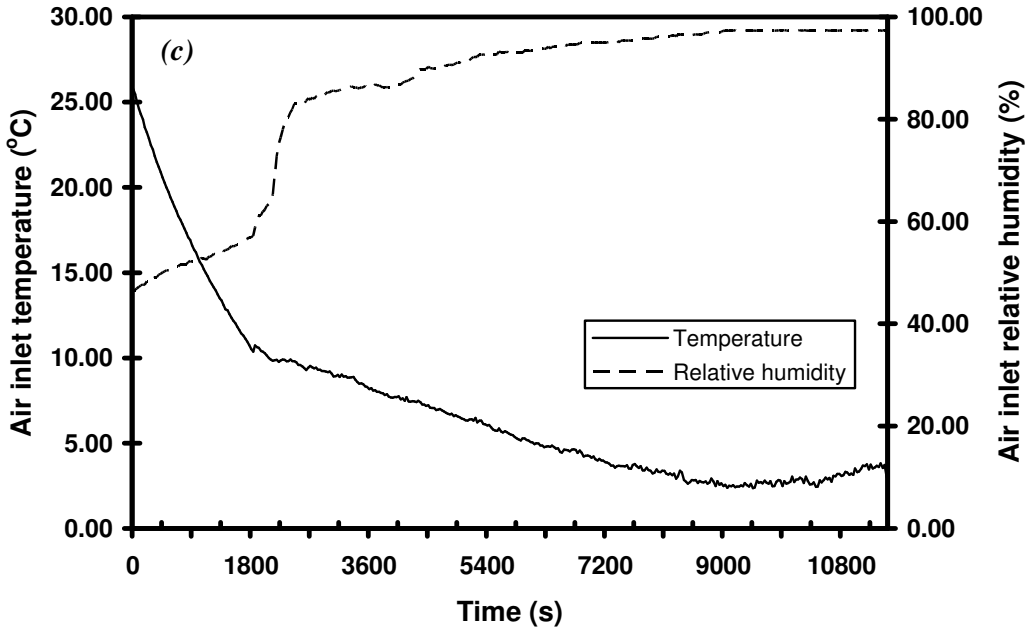

Figure 5.4: ***Evaporator air inlet temperature and relative humidity for (a) observation 1, (b) observation 2 and (c) observation 3.***

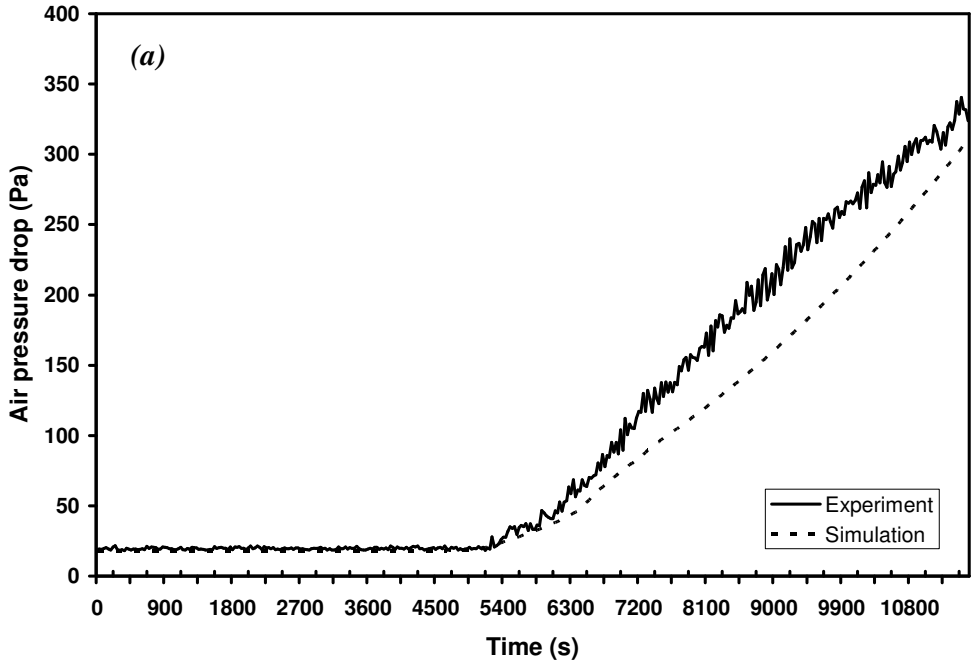

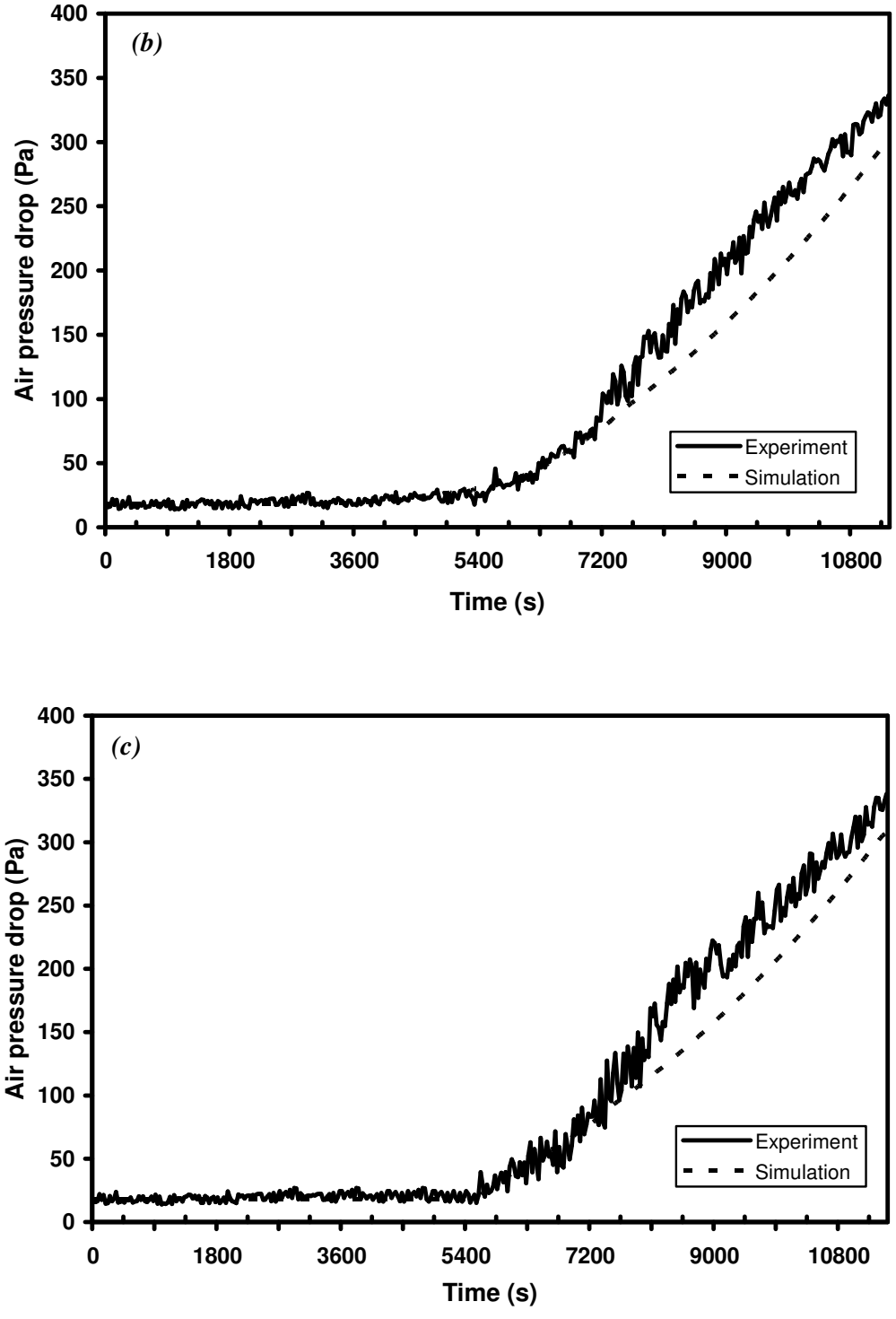

Figure 5.5: ***Comparison for air pressure drop across the coil for (a) observation 1, (b) observation 2 and (c) observation 3.***

The air pressure drop was maintained constant at approximately 20 Pa until at around 5400 s when the air pressure dropped across the coil gradually increased and reached approximately 330 Pa at the end of the test for observation 1, 2 and 3, as shown in Fig. 5.5 (a), 5.5 (b) and 5.5 (c). This increase in pressure drop was caused by the significant growth of frost along the coil. The growth and propagation of frost reduce the air flow passage resulting in increased air pressure difference between the inlet and outlet. The trend of change in air pressure drop is consistent with the results reported by other researchers such as Senshu et al. (1990) and Yan et al. (2003).

From Fig. 5.6, the air outlet temperature was seen to reduce, as the air inlet temperature reduces, as shown earlier in Fig. 5.4. The air outlet temperature increases at around 2950 s for observation 1 (Fig. 5.6 (a)), around 2730 s for observation 2 (Fig. 5.6 (b)) and around 1830 s for observation 3 (Fig. 5.6 (c)), when the artificial load generator was initiated. The increase in temperature could be due to the fact that more of the cooling load was used for latent rather than sensible cooling. The air outlet temperature continues to decrease until it reaches around -3.9 ^{o}C for observation 1, around -4.0 ^{o}C for observation 2 and around -3.5 ^{o}C for observation 3 at the end of the test.

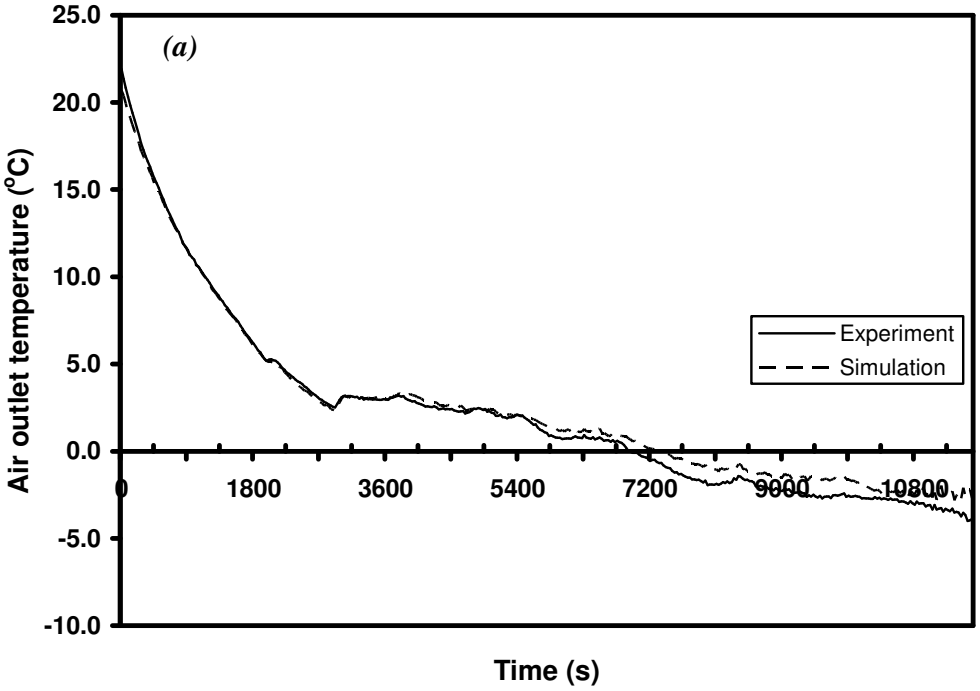

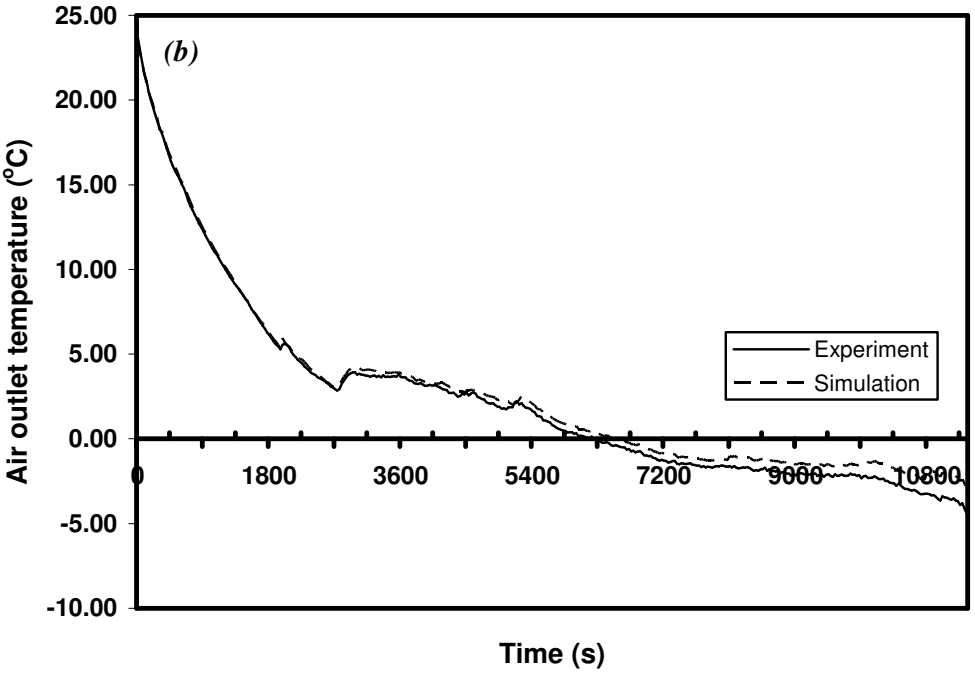

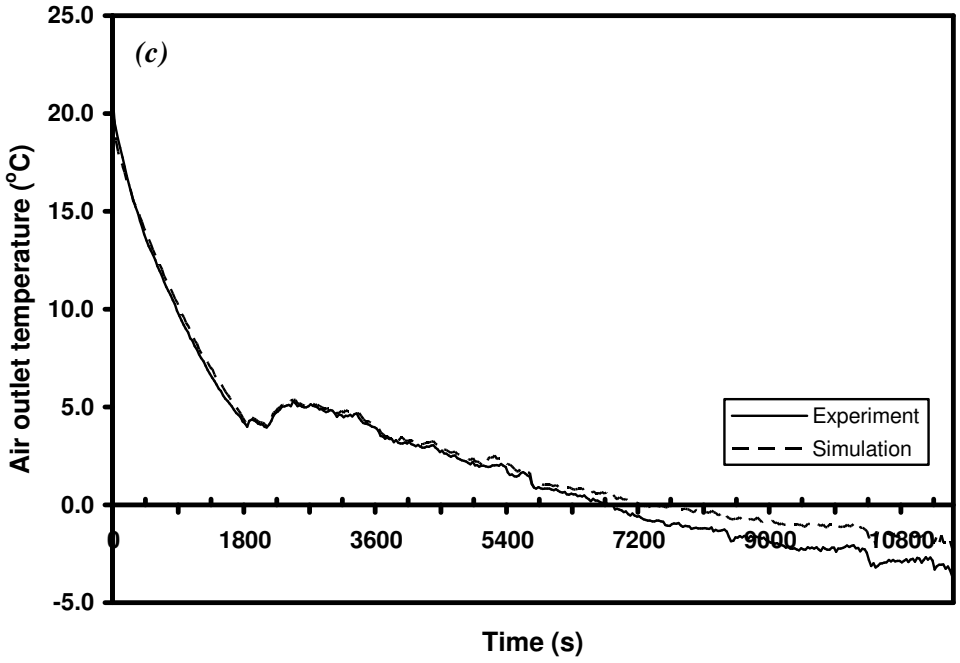

Figure 5.6: ***Comparison for air outlet temperature for (a) observation 1, (b) observation 2 and (c) observation 3.***

5.3.2 Field observation on refrigerant side

The evaporating refrigerant pressure reduces as the air temperature reduces. This change was due to the lower air inlet temperature and the thermal expansion device limits the flow of refrigerant inside the coil to maintain the preset refrigerant outlet superheat. The evaporator pressure kept decreasing until at approximately 10700 s for observation 1 (Fig. 5.7 (a)), 10830 s for observation 2 (Fig. 5.7 (b)) and 10350 s for observation 2 (Fig. 5.7 (c)) when the evaporator pressure begins to fluctuate till the end of the test.

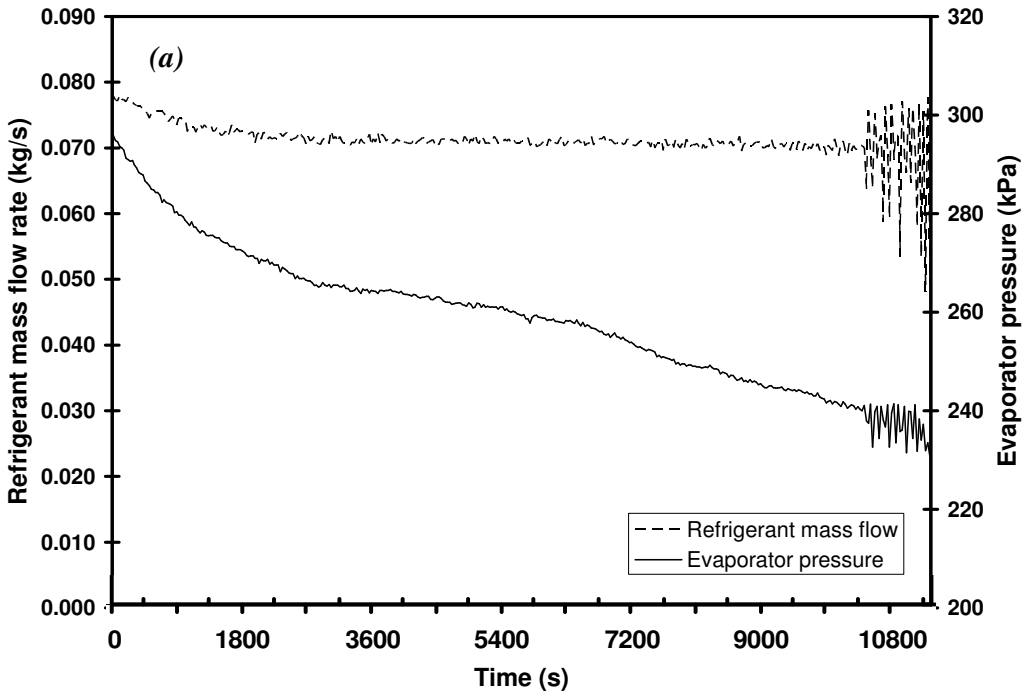

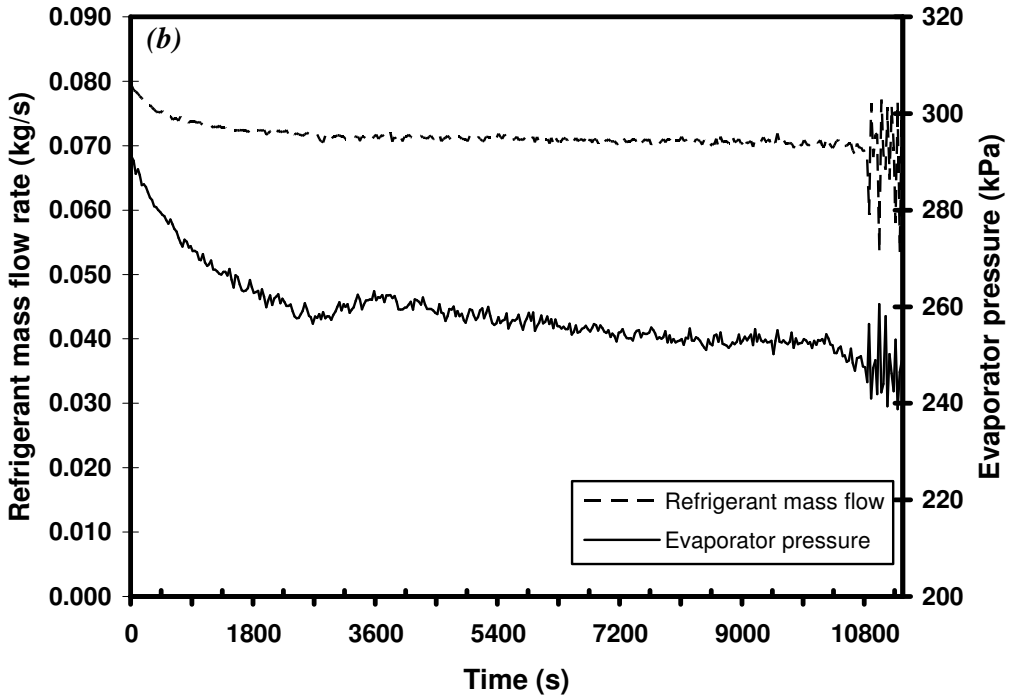

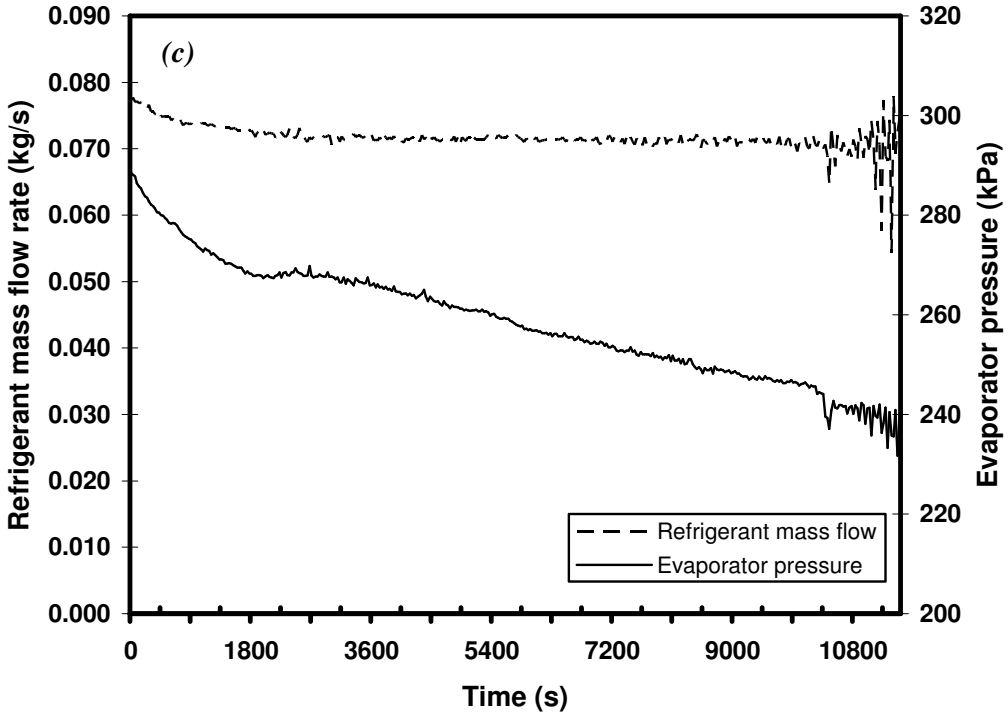

Figure 5.7: ***Refrigerant mass flow rate and evaporator pressure for (a) observation 1, (b) observation 2 and (c) observation 3.***

The mass flow rate of refrigerant was rather constant at around 0.075 kg/s for all three observations, and starts fluctuating at approximately 10700 s for observation 1, 10830 s for observation 2 and 10350 s for observation 3. The fluctuation becomes more severe toward the end of the test for all three observations. These fluctuations were due to the hunting behavior of the thermal expansion valve (TXV) that endeavors to maintain the refrigerant superheat at the coil exit. Formation of frost on the evaporator acts as insulation that leads to the reduction of heat transfer from the air to the refrigerant. Less heat transferred implies less refrigerant evaporation and in order to maintain the refrigerant superheat leaving the coil, the TXV limits the refrigerant flow into the coil. This causes the refrigerant superheat to exceed the

TXV set-point and therefore, the TXV responds by increasing the refrigerant mass flow. The fluctuation caused by this increase and decrease of refrigerant mass flow was aggravated when frost growth continues.

5.3.3 Field observation of frost formation

A thin layer of frost was observed on the tube and fin at the end of the first row and the beginning of the second row (on the right hand side) along the tube circuit at 3600 s for observation 1. The refrigerant pressure was 264.6 kPa with refrigerant temperature of -4.6 ^{o}C. Similar thin layer of frost were also observed during second and third observation at 3750 s and 3700 s with the refrigerant pressure and temperature of 262.3 kPa, -4.8 ^{o}C and 265.5 kPa, -4.5 ^{o}C. The frost starts to form here because of the uneven air distribution, where less air was channeled to the side, and because of the pressure reduction inside the refrigerant due to the 180 degree tube bend. Less air flow leads to lower heat transfer rate and therefore, the wall temperature was lower, and this encourages frost growth. The tube bend causes the refrigerant pressure to decrease and results in a lower wall temperature which also promotes frost formation. The frost progressively builds up at this area and eventually blocks the fin gaps at around 5900 s for observation 1, 5600 s for observation 2 and 6000 s.

Frost was seen on fins at the refrigerant inlet side at around 4300 s for observation 1, and by 5900 s, the first and second rows were covered with frost. In second and third observation, frost was seen around 4200 s and 4500 s and first and second rows were covered with frost around 5600 s and 6000 s. This was due to the

fact that the refrigerant inside the tube for the first few rows were still in the two-phase region and less amount of refrigerant boils off. Clear vision of frost was observed on the entrance of the third row around 6000 s and the frost propagates toward the end of third row by 7700 s for first observation. Second and third observation also showed sign of frost at the entrance of third row around 5900 s and 6300 s and covered the third row at around 7600 s and 7800 s. At the same time, frost on the first and second rows continued to grow with growth on the first row faster than that of the second row. This phenomenon occurred because frost formation and built-up increased insulation effect and reduced the heat transfer. As less refrigerant evaporates, the wall temperature decreased and therefore the frost growth increases. The liquid refrigerant then flows along the coil, causing the wall temperature along the coil to decrease. Hence the frost propagation along the coil could be observed. The fins for the fourth row were covered with frost by 9840 s for observation 1, 9700 s for observation 2 and 9900 for observation 3. Frost continued to form on the surface of the fifth row when the wall temperature at that row dropped below freezing point.

At the end of the test, the whole system was shut-down and the frost was allowed to melt at room temperature. The resulting water was collected in bottles via a funnel.

5.4 Comparison with simulation results

The air inlet temperature, air humidity, refrigerant mass flow rate and evaporator pressure shown in Fig. 5.4 and Fig. 5.7 are used as the input conditions for the numerical simulation. Comparisons are made in terms of air side pressure drop, air outlet temperature, energy transfer rate and frost growth.

5.4.1 Air side comparisons

Comparison between the simulation results and the experimental results on the air side pressure drop across the coil can also be seen in Fig. 5.5. The trend of pressure drop increasing with frost growth is found to be true for both cases and consistent with other researchers as mentioned in section 5.3.1. The simulated pressure drop before 5500 s matches closely with the experiment with differences within 7 %. When frost height starts to grow and cause the air pressure drop to increase, the predicted values deviates to a maximum value of around 22 % and then closer again to approximately 7 % at the end. On average, it is found that the model under-predicts the experiment data within 20 % of each other. For second observation, the air pressure drop starts to deviate around 7200 s to a maximum of around 20 % and approximately 10 % at the end. As for third observation, it starts to deviate around 7200 s to a maximum of around 20 % and approximately 10% at the end. The pressure drop influences the air flow which is also one of the variables that affects the frost growth. It changes the air side heat transfer coefficient as a consequence of the velocity associated with the blockage at the fins. A more accurate model for predicting the air pressure drop is desirable.

Referring to Fig. 5.6 again, comparison with simulation results shows that the model is capable of predicting accurately the air outlet temperature for conditions before frost formation. There is also close agreement between the experiment and model prediction with frost formation, with the model under-predicting the air outlet temperature by approximately 1 to 2 ^{o}C for all three observations. Inferring from the figure, it can be seen that the temperatures begin to deviate at around 5400 s for first observation, 5300 s for second observation and 5800 s for third observation, where the first row and most of the second row are covered with frost. The differences could be due to the under-prediction of the pressure drop across the coil and also the accuracy of the heat transfer coefficient. The air side heat transfer coefficient is not only a function of the geometry of evaporator, air properties and frost surface roughness, but also changes with time. The Reynolds and Prandtl numbers, Colburn j factor and the spacing between fins changes with time too. Therefore, a more accurate heat transfer coefficient can improve the model.

5.4.2 Energy transfer rate comparison

The energy transferred, Q, to the refrigerant is calculated based on the refrigerant enthalpy difference, which is:

$$Q = m_r (h_{r,out} - h_{r,in}) \tag{5.1}$$

where m_r is refrigerant mass flow rate (kg/s), $h_{r,in}$ is the inlet refrigerant enthalpy (J/kg) and $h_{r,out}$ is the outlet refrigerant enthalpy (J/kg).

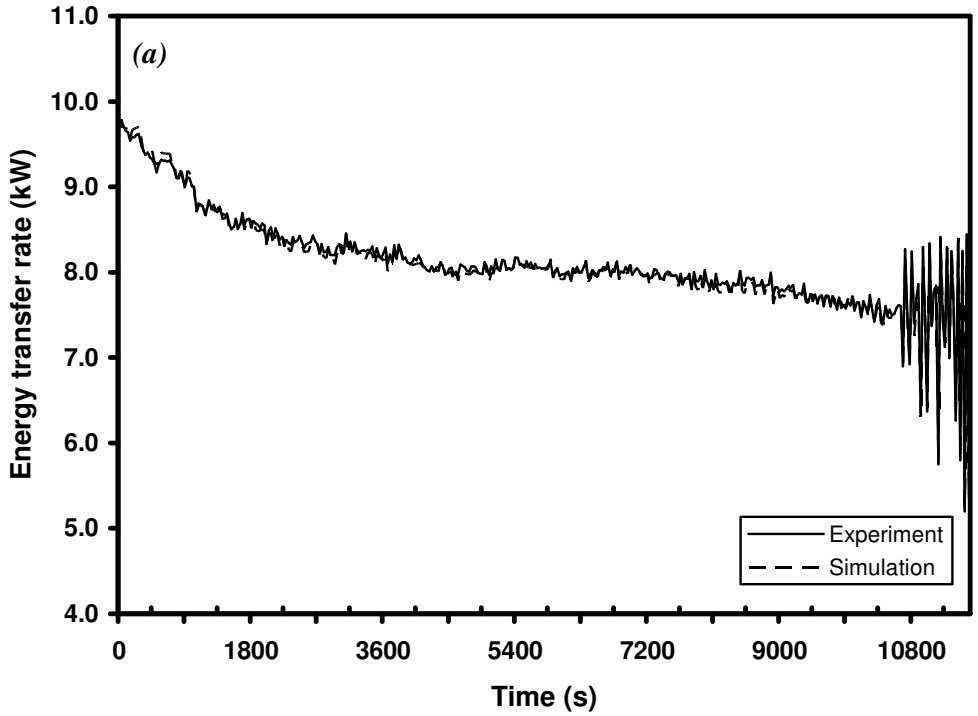

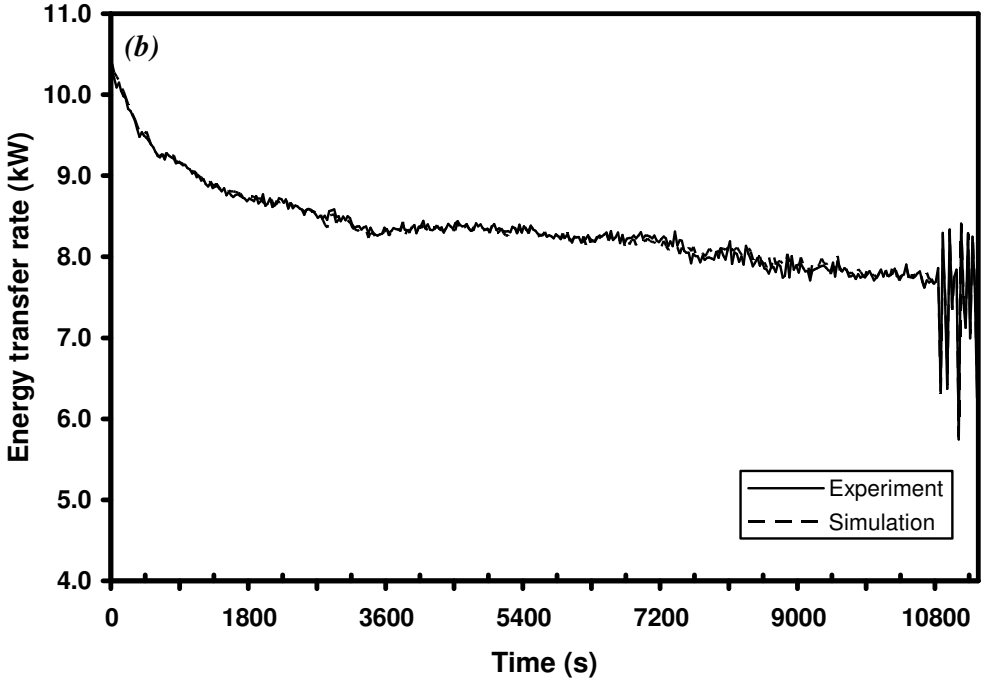

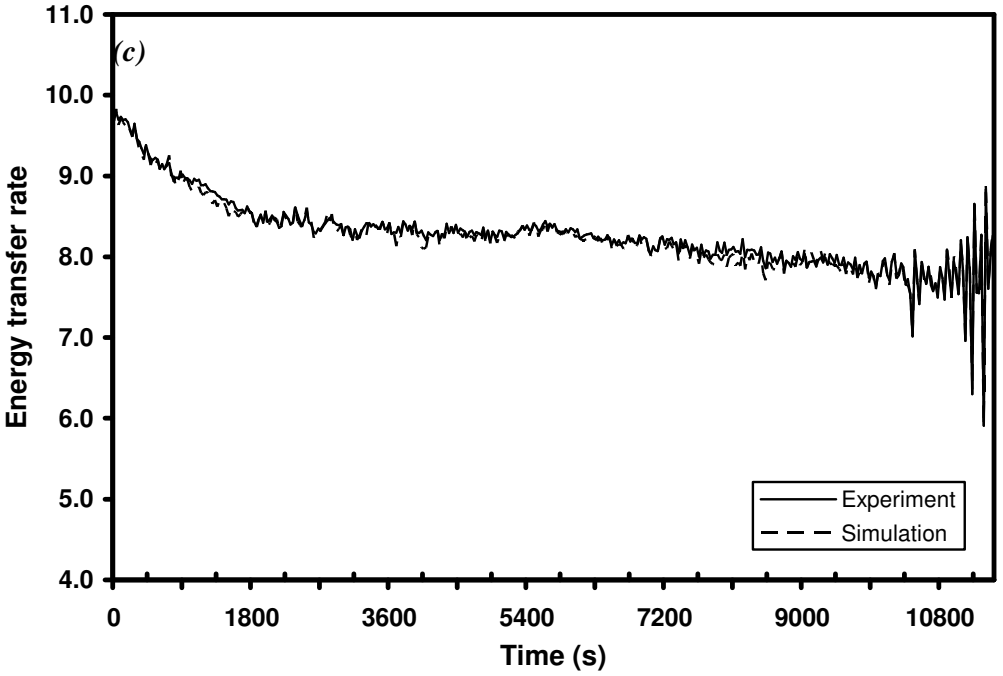

Figure 5.8: ***Comparison of energy transfer rates for (a) observation 1, (b) observation 2 and (c) observation 3.***

As the difference between refrigerant and air temperatures reduces, the energy transferred to the refrigerant reduces as shown in Fig. 5.8. When frost begins to form and build up on the evaporator, it acts as insulator to reduce energy transfer from air to refrigerant, which causes the energy transfer to decrease. Less evaporated refrigerant reduces the enthalpy of the refrigerant leaving the coil. The energy transfer begins to fluctuate at 10700 s for observation 1, around 10800 s for observation 2 and around 10300 s for observation 3 with hunting of the TXV, as described earlier in section 5.3.2.

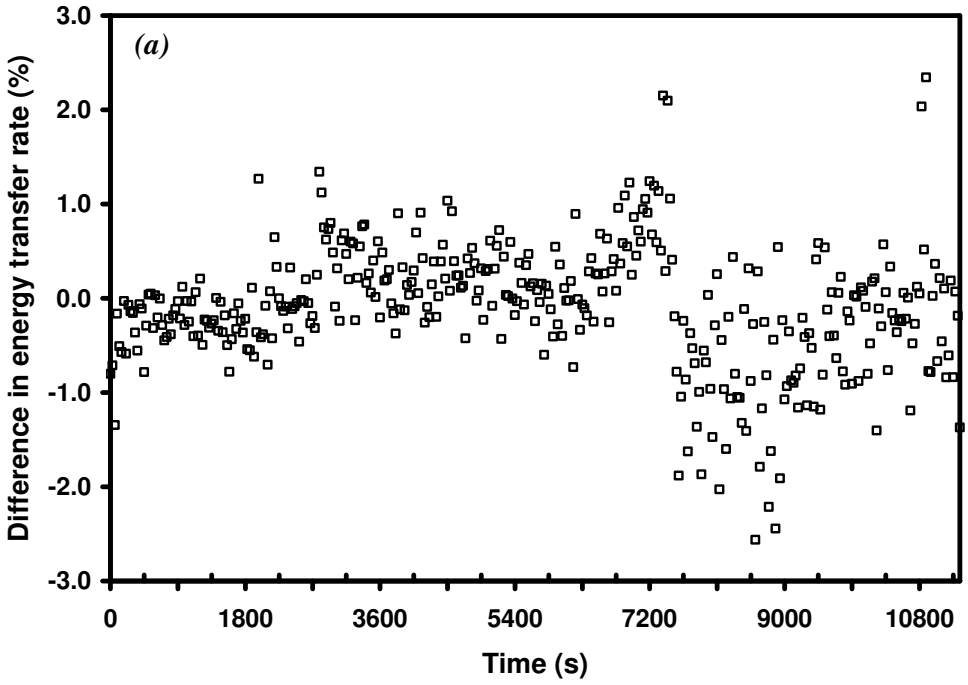

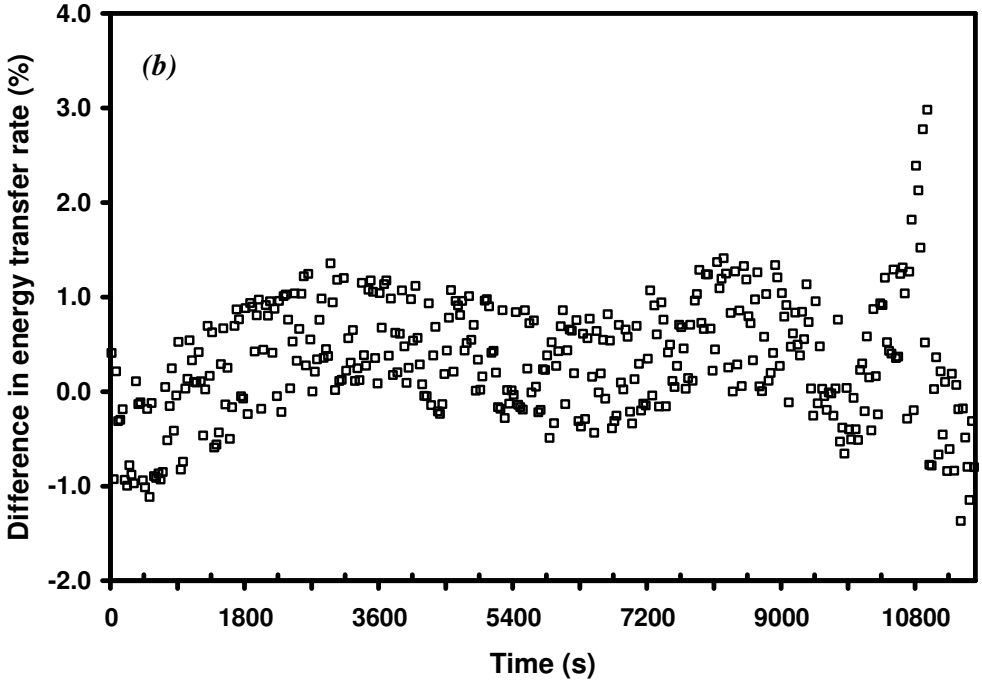

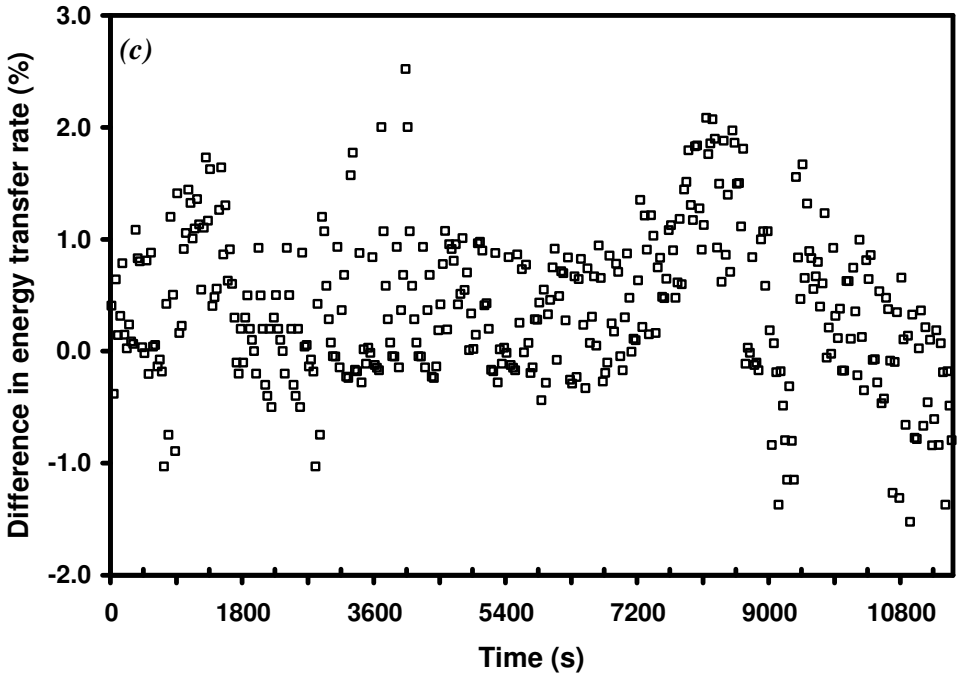

Figure 5.9: ***Differences between experimental and predicted energy transfer rates for (a) observation 1, (b) observation 2 and (c) observation 3.***

The Fig. 5.9 accentuates the differences in energy transfer rates between experimental and predicted values, as defined by:

$$\text{Difference in energy transfer rate} = \frac{\text{Experimental} - \text{Predicted}}{\text{Experimental}} \times 100\% \qquad (5.2)$$

Overall, it is found that the model predicts well, with an overall difference of ± 3 % of each other for all three observations. The uncertainty of energy transfer rate is estimated to be within ± 6 %.

5.4.3 Frost growth comparison

The predicted frost mass accumulation and the corresponding field observation of frost as discussed in section 5.3.3 are shown in Fig. 5.10. From field observation, the frost begins to form at both ends of first row before 4500 s but the simulated result shows frost formation at around 5000 s. This is because in simulation, the air flow is assumed to be evenly distributed whereas the flow is uneven in practice. The frost mass accumulation increases gradually initially and later increases approximately in a linear fashion till the end. This linear trend is consistent with results in Kondepudi and O'Neal (1993) and other researchers.

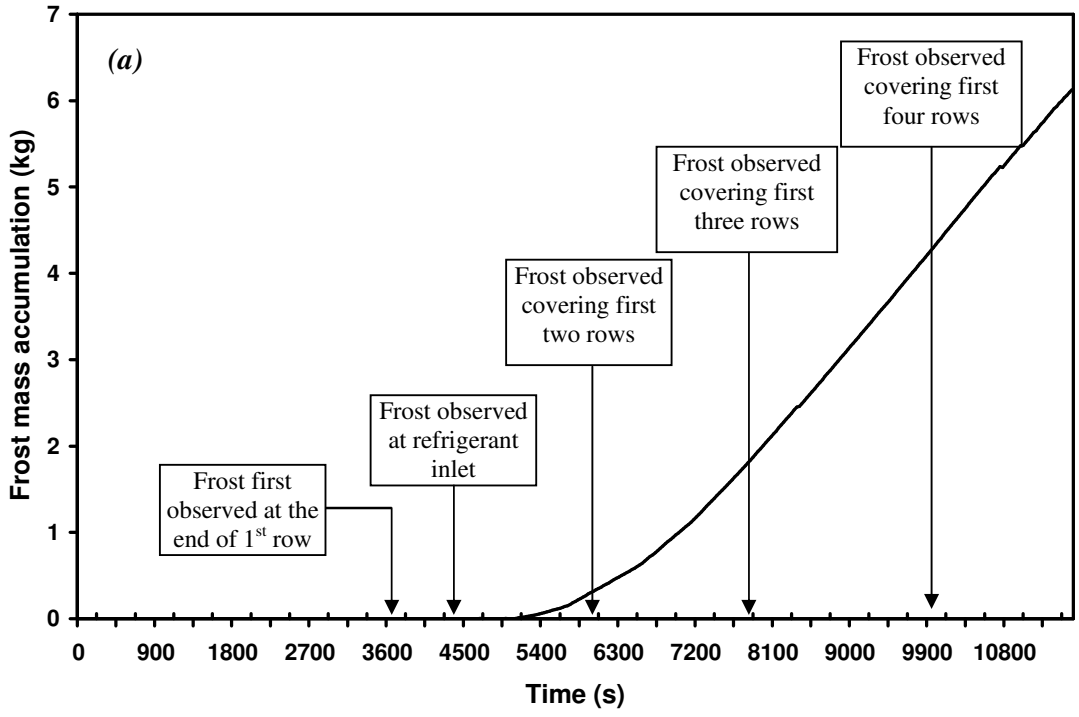

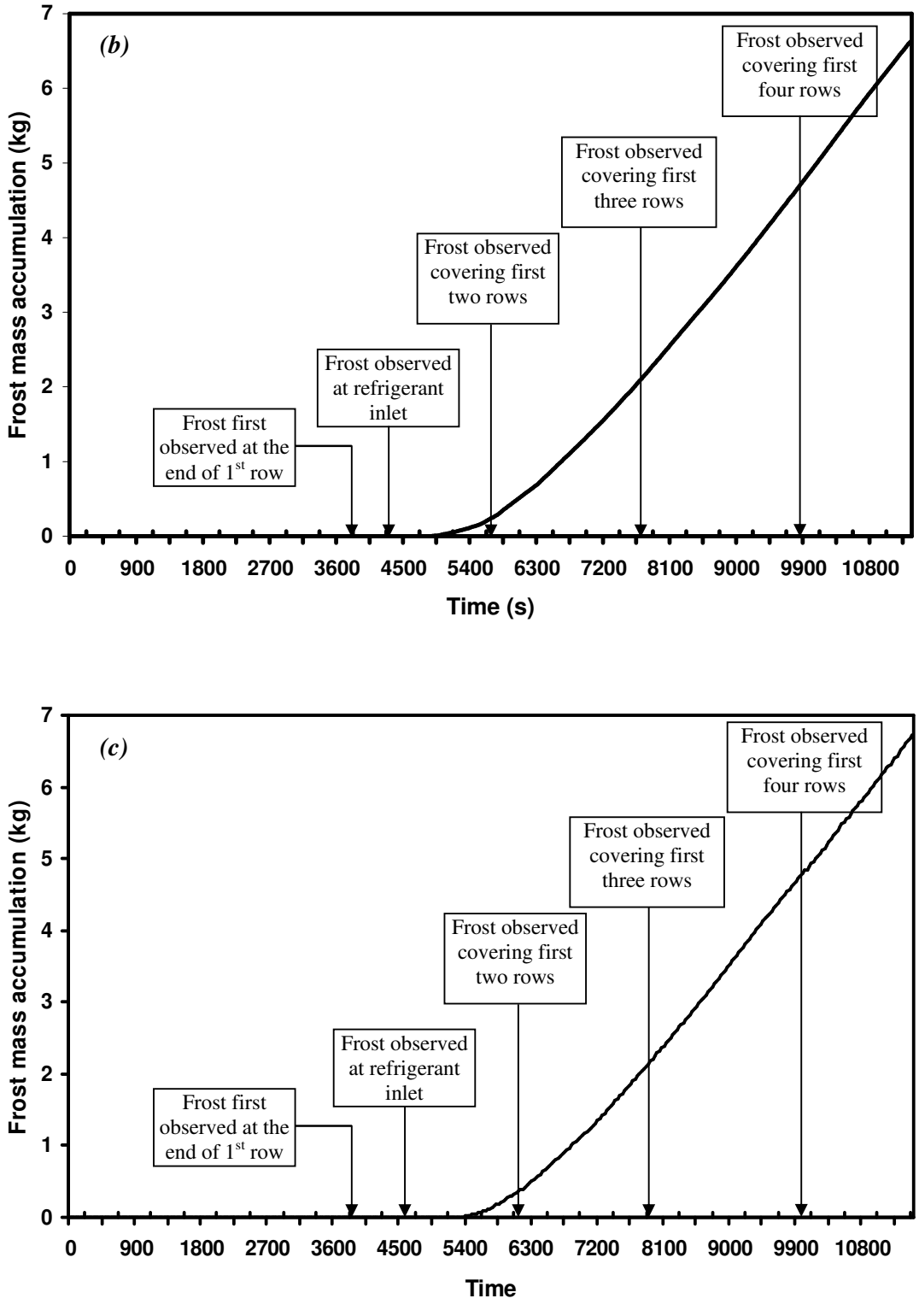

Figure 5.10: ***Predicted frost mass accumulation and observation of frost in field test for (a) observation 1, (b) observation 2 and (c) observation 3.***

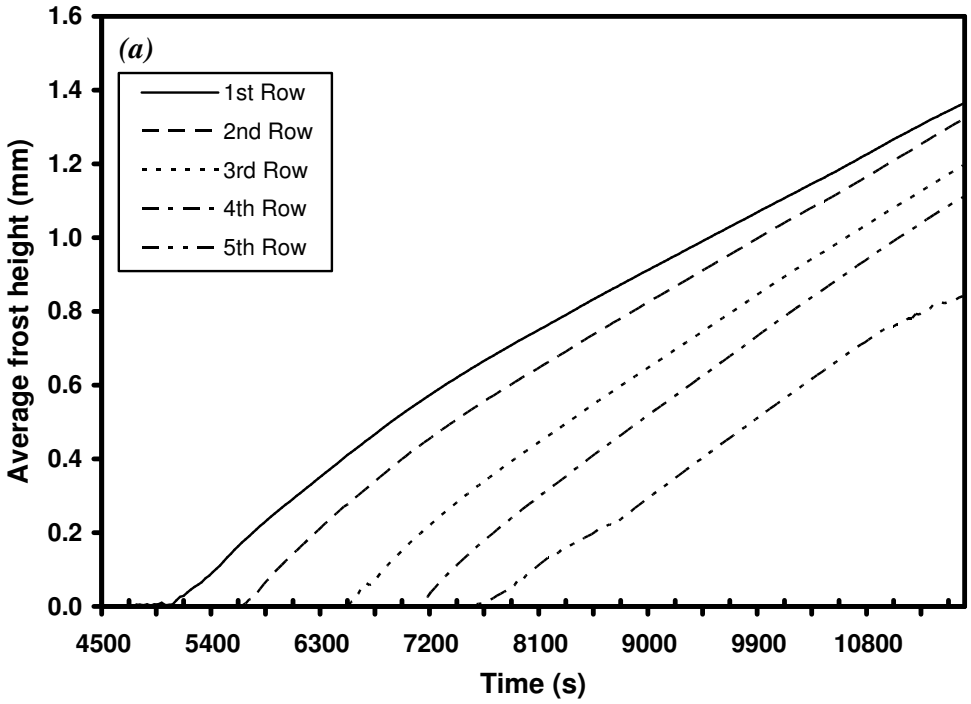

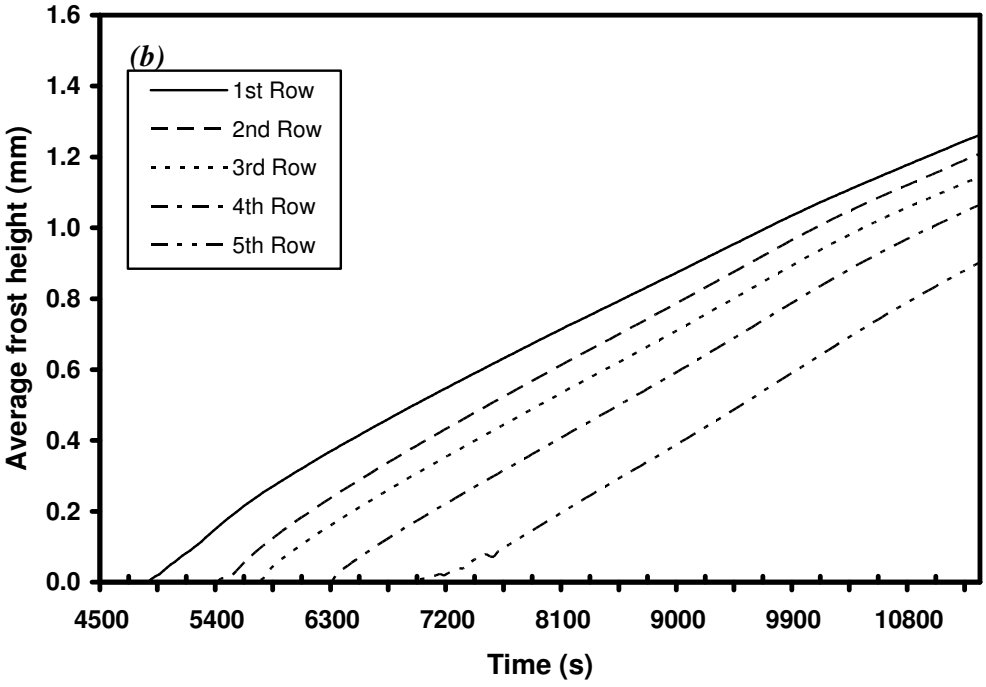

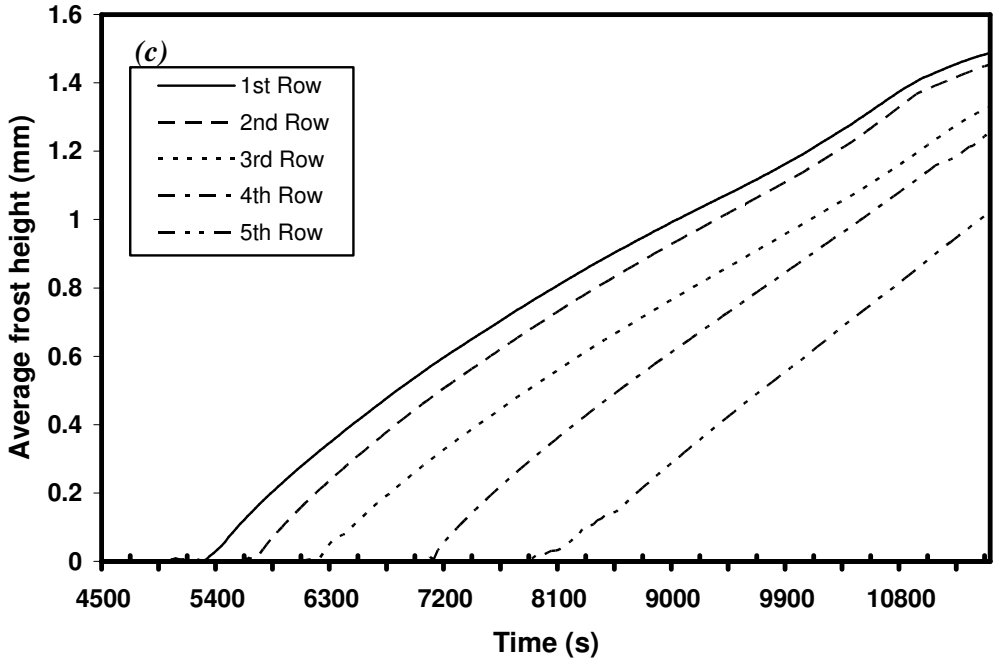

Figure 5.11: ***Predicted average frost height for various rows based on operating data for (a) observation 1, (b) observation 2 and (c) observation 3.***

The Fig. 5.11 shows the predicted average frost height for respective rows. The results are based on the average values of 40 cells per row. The prediction based on the operating conditions of observation 1, first row has the highest frost height which has an average frost height of 1.36 mm at the end of simulation. This is followed by the second row which has an average of 1.32 mm, the third row with 1.20 mm, the fourth row with 1.11 mm and fifth row with 0.84 mm. Predicted frost height based on operating conditions for observation 2 are 1.26 mm, 1.20 mm, 1.14 mm, 1.06 mm and 0.9 mm for first to fifth rows. Based on the operating conditions of the third observation, the predicted frost height are 1.48 mm, 1.45 mm, 1.32 mm, 1.25 mm and 1.01 mm. The trend of frost height for counter flow configuration

where the first row has the highest frost growth rate is found to be true for both experimental and model and is consistent with experimental data of Aoki et al (1991).

Comparing the field observation of frost growth with the predicted average frost height, they are agreeable that frost covers the first two rows around 5900 s, 5600 s and 6000 s for the three observations. From the field observation, the frost covers the first three rows at around 7700 s for the first observation but the simulated result shows frost appearing at the fourth row with an average frost height of around 0.25 mm. Similarly for the second and third observation where at around 7600 s and 7800 s, frost covers the first three rows but the simulated results shows frost on forth row with average frost height of 0.3 mm and 0.27 mm. At 9840 s, the simulated result shows frost covers the fifth row with an average height of 0.4 mm for observation 1, but in the field, only four rows are covered with frost. The simulated results based on second and third observation shows similar condition with average frost height of 0.54 mm and 0.55 mm but only four rows are observed covering with frost. The formation and propagation of frost seems to be slower than the simulated results because during the coil frosting at the first few rows, the wall temperatures for last few rows of the coil are still above freezing point but could be below the dew point. This could lead to the condensation of water on the fin and wall surface, and the condensate drip effect causes water to soak into the frost layer at the subsequent row below.

The total amount of condensate collected after the experiment is 8.28 kg, 8.49 kg and 8.82 kg for observation 1, 2 and 3. Fig. 5.10 shows the predicted frost mass

accumulation at the end of the experiment to be 6.13 kg, 6.62 kg and 6.73 kg for the three observations. The difference is 2.15 kg, 1.87 kg and 2.09 kg or approximately 25 % less than the actual amount. This difference could be due to two reasons. Firstly, the condensate drip effect incurs additional mass onto the total frost mass. Secondly, when the system is shut-down and allowed to melt at room temperature, the coil and frost surfaces are still below freezing or dew point. Mass transfer of water vapor from air continues to occur even after the system has shut-down. This additional mass transfer is not taken into consideration of simulation. Between the two reasons, the condensate drip effect is more dominant.

5.5 Conclusions

A field investigation was conducted successfully on a full-scale commercial refrigerated container. The field observation and data collected are compared with predicted results from model simulations. Comparison in terms of air side pressure drop, air outlet temperature, energy transfer rate and frost growth are made. The following conclusions can be made:

a) Frost formation is observed to occur first at both ends of the first row where the refrigerant enters the evaporator, due to the uneven air flow and pressure drop at the bend.
b) The distributed model is capable of predicting the dynamic performance of the evaporator under non-frosting and frosting conditions.

c) The model under-predicts the pressure drop for coil with 6 rows by about 20 %, hence a better model to predict the pressure drop under frosting condition is required.

d) The air outlet temperature compares well with model results for non-frosting condition, but for the frosting condition, the deviation increases slowly to 2 ^{o}C at the end of field investigation. A better prediction for the air side heat transfer coefficient would improve.

e) The energy transferred to refrigerant has good agreement between the field observation and model with differences within ± 3 %, although the uncertainty in the experiment is within ± 6 %.

f) The model can predict results for the occurrence of frost on respective rows of the evaporator. For this counter flow arrangement, model and experimental results are agreeable on the propagation of frost from the first row at the refrigerant inlet to subsequent rows, as well as that the first row having the highest frost accumulation.

g) The model under-predicts frost mass accumulation by about 25 %. The main reason for this could be due to the condensate drip effect. The condensate drip effect should be accounted for in future work.

CHAPTER 6
Conclusions and Recommendations

6.1 Conclusions

The presence of frost and frost growth on air cooler is a continuous transient process. Frost formation on air cooler degrades the performance of the air cooler as well as the whole cooling / refrigeration system. The effects of frost on the performance of the air cooler have been studied theoretically. Field investigation has been carried out on a full scale refrigerated container to validate the theoretical / mathematical model.

A general distributed model with two-phase flow for refrigerant coupled with a frost model for non-steady performance of finned-tube evaporator under frosting and non-frosting conditions has been presented. The governing equations for refrigerant are derived from conservation of mass, momentum and energy in one-dimensional time-dependent state. The refrigerant flow inside the tube is modeled by a two-phase drift flux model. For tube wall side, the governing equation is derived using conservation of energy in time-dependent state. The equations for air side derived using conservation of mass and energy are resolved. The model for single-phase fluid such as brine or glycol/water mixture is also presented in time-dependent state. The frost model is developed based on the molecular diffusion of water vapor, energy and mass balance, as well as equation of state. The frost layer is treated as a porous media with transient and one-dimensional heat and mass transfer. The

prediction of frost growth and densification is analyzed with quasi-steady state approach. During each time step, the heat and mass transfer processes of the frost layer are regards as the steady state. The calculation results at one time step are stored and used at the next time step. A literature search has been carried out and the suitable correlations are selected for the mathematical model.

A FORTRAN program is developed and selection of number of cells, convergence criterion, time steps and drift flux model are carried out, based on a full scale container refrigeration system. The computer code was an extension from an in house previous code with substantial modifications in order to incorporate the air cooler under frost condition. The modifications involve developing a new subroutine for calculation of frost properties which include the frost thermal conductivity, frost thickness, frost density and heat and mass transfer in frost layer. Extensive modifications of subroutines to include solving the equations when the frost forms on the cell, changes of air side heat transfer coefficient and pressure drop when frost occurs. The results for non-frosted evaporator using volatile refrigerant compared well with the reported experimental results. Further studies were carried out on the effect of refrigerant liquid dry-out position on the air temperature distribution inside the evaporator. The simulated results showed that variation of air and wall temperature would have effect on the frost deposition on the evaporator.

The effects of the various environmental conditions and fin geometries on frost deposition, energy transfer, air outlet temperature, frost accumulation, frost

growth and air pressure drops were simulated. The results have been qualitatively compared with the findings reported in literature and can be summarised as follows:

a) The frost formation is high for a low air mass flow rate, high relative humidity, high air inlet temperature and high fin pitch.
b) Formation of frost degrades the performance of the heat exchanger.
c) With the increase of frost growth, the total air side heat transfer will decrease and the air pressure drop across evaporator will increase.
d) The air and wall temperature vary along the tubes and coil which lead to non-uniform frost growth along coil.
e) The temperature along fin varies and this causes uneven frost growth.
f) At the tube row where the refrigerant inlet is located, which has lower wall temperature, it is found that more frost accumulation and growth.
g) The frost growth propagates along the tube toward the coil exit.
h) The model predicts Kondepudi and O'Neal (1990) experimental data for single row heat exchanger with single-phase fluid well.

    (i) Total frost mass predicted is 0.46 kg as compared to 0.43 kg from experiment with discrepancy of 7 %.
    (ii) The air pressure drop across the heat exchanger matches closely within 8 % with experimental result.

Besides simulation conducted, a field investigation has been performed on a full-scale commercial refrigerated container. The evaporator consists of 6 rows, 9

circuits with R12 as working fluid. The field observation and data collected are compared with predicted results from model simulations. Comparisons in terms of air side pressure drop, air outlet temperature, energy transfer rate and frost growth are made. The findings can be summarized as follows:

a) Frost formation is observed to occur first at both ends of the first row where the refrigerant enters the evaporator, due to the uneven air flow and pressure drop at the bend.
b) The distributed model is capable of predicting the dynamic performance of the evaporator under non-frost and frost conditions.
c) The model under-predicts the pressure drop by about 20 %, comparing to the field observation.
d) The air outlet temperature compares well with model results for non-frosting condition, but for the frosting condition, the deviation increases slowly to around 1 – 2 ^{o}C toward the end of the field observation.
e) The energy transferred to refrigerant has good agreement between the collected data and model with differences within ± 3 %, although the uncertainty in the experiment is within ± 6 %.
f) The model can predict results for the occurrence of frost on respective rows of the evaporator. For this counter flow arrangement, model and the data collected are agreeable on the propagation of frost from the first row at the refrigerant inlet to subsequent rows, as well as that the first row having the highest frost accumulation.

6.2 Recommendations

Based on the results of this study, the following recommendation can be made:

a) The current model is developed based on air cooler with flat fin and smooth tube. Improvement can be made on modeling of enhanced fin surface and tube inner surface to be incorporated in the mathematical model.

b) The proposed air cooler model could be link into a system model (Dabiri (1982), Damasceno et al. (1990)) in future.

c) The model for air pressure drop across the air cooler matched closely with experiment for single row but not for air cooler greater than one row. A better model to predict the pressure drop under frosting condition is required.

d) The heat transfer coefficient employed in the model predicts well for non frost condition but starts to deviate when frost starts to form. A better prediction for the air side heat transfer coefficient would improve.

e) The condensate drip effect was observed when part of the evaporator is above the freezing temperature and below the dew point temperature. This condensate drip effect will affect the frost and should be accounted in the modeling.

f) The permeation process which occurs once the air frost interface temperature reaches the freezing temperature, a proper experimental setup to validate the mathematical model is required.

g) Any further studies should consider to include the following measurement in the experimental setup.

i. A series of cameras that could provide visual confirmation of frost on different rows and along the rows.

ii. Temperature measurement on the fins and tube in several locations of the coil to provide some indication on the refrigerant distribution and possible of shifts in refrigeration distribution due to frost.

References

1. Abdel-Wahed, R.M., Hifni, M.A. and Sherif, S.A., 1984, "Heat and mass transfer from a laminar humid air stream to a plate at subfreezing temperature", Int. J. Refrigeration 7(1), pp. 49-55.
2. Ameen, F.R., 1993, "Study of frosting of heat pump evaporator", ASHRAE Transaction, 99 (1), pp. 61-71.
3. Aoki, K., Hattori, M. and Hayashi, Y., 1991, "A study of frost formation", Freezing and Melting Heat Transfer In Engineering, Hemisphere Publishing Corporation, pp. 451-487.
4. ASHRAE, 2001, Handbook of Fundamentals, Atlanta: America Society of Heating, Refrigerating and Air-Conditioning Engineers.
5. ASHRAE, 2002, Handbook of Refrigeration, Atlanta: America Society of Heating, Refrigerating and Air-Conditioning Engineers.
6. Biguria, G.O. and Wenzel, L.A., 1970, "Measurement and correlation of water frost thermal conductivity and density", Industrial and Engineering Chemistry Fundamentals 9(1), pp. 129-138.
7. Brian, P.L.T., Reid, R.C. and Brazinsky, I., 1969, "Cryogenic frost properties", Cryogenic Technology, 5, pp. 205-212.
8. Chen, H., Besant, R.W. and Tao, Y.X., 1999, "Frost characteristics and heat transfer on a flat plate under freezer operating conditions: Part II, Numerical modeling and comparison with data", ASHRAE Transaction, 105(2), pp. 252-259.

9. Chen, H., Thomas, L. and Besant, R.W., 2000a, "Modeling frost characteristics on heat exchanger fins: Part I, Numerical model", ASHRAE Transactions, 106(2), pp. 357-367.

10. Chen, H., Thomas, L. and Besant, R.W., 2000b, "Modeling frost characteristics on heat exchanger fins: Part II, Model validation and limitations", ASHRAE Transactions, 106(2), pp 368-376.

11. Chen, H., Thomas, L. and Besant, R.W., 2002, "Fan supplied heat exchanger fin performance under frosting conditions", Int. J. Refrigeration, 26, pp. 140-149.

12. Chen, M.M. and Rohsenow, W., 1964, "Heat, mass and momentum transfer inside frosted tubes- experimental and theory", Journal of Heat Transfer, 86(3), pp.334-340.

13. Cheng, CH and Shiu, C.C., 2002, "Frost formation and frost crystal growth on a cold plate in atmospheric air flow", Int. Journal of Heat and Mass Transfer, 45, pp.4289-4303.

14. Cheng, CH and Wu, KH, 2003, "Observations of early-stage frost formation on a cold plate in atmospheric air flow", ASME Journal of Heat Transfer, 125, pp. 95-102.

15. Chisholm, D., 1973, "Void fraction during two-phase flow", Journal of Mechanical Engineering Science, 15 (3), pp. 235-357.

16. Chuang, M.C., 1976, "The frost formation parallel plates at very low temperature in a humid stream", ASME Paper 76-WA/HT-60, pp.1-5.

17. Chung, P.M. and Algren, A.B., 1958a, "Frost formation and heat transfer on a cylinder surface in humid air cross flow, part I: experimental study", Heating, piping and air conditioning, 30(9), pp. 171-177.

18. Chung, P.M. and Algren, A.B., 1958b, "Frost formation and heat transfer on a cylinder surface in humid air cross flow, part II: theoretical study and conclusion", Heating, piping and air conditioning, 30(10), pp. 115-122.

19. Dabiri, A. E., 1982. "A Steady-State Computer Simulation Model for Air-To-Air Heat Pumps", ASHRAE Transactions, 88, Pt. 2, pp. 973–987.

20. Damasceno, G. S., Goldschmidt, V. W., and Rooke, S. P., 1990. "Comparison of Three Steady-State Heat Pump Computer Models", ASHRAE Transactions, 96, Pt. 2.

21. Deng, DQ, Xu, L. and Xu, SQ, 2003, "Experimental investigation on the performance of air cooler under frosting conditions", Applied Thermal Engineering, 23, pp. 905-912.

22. Dietenberger, M.A., 1983, "Generalized correlation of the water frost thermal conductivity", Int. J. Heat Mass Transfer, 26 (4), pp. 607-619.

23. Gatchilov, T.S. and Ivanova, V.S., 1979, "Characteristics of the frost formed on the surface of finned air coolers", 15th International Congress of Refrigeration, Venice, B2/71, pp. 997-1003.

24. Gates, R.R., Sepsy, C.F. and Huffman, G.D., 1967, "Heat transfer and pressure loss in extended surface heat exchangers operating under frosting conditions", ASHRAE Transaction, 73(2), pp. I.2.1-I.2.13.

25. Hayashi, Y., Aoki, A., Adachi, S. and Hori, K., 1977, "Study of frost properties correlating with frost formation types", ASME Journal of Heat Transfer, 99(2), pp. 239-245.

26. Hewitt, G. F., 1990, Hemisphere Handbook of Heat Exchanger Design. New York: Hemisphere.

27. Hoffenbecker, N., 2004, "Investigation of alternative defrost strategies", M. Sc. Dissertation, University of Wisconsin – Madison.

28. Incropera, F.P. and DeWitt, D.P., 2002, Fundamentals of Heat and Mass Transfer, Fifth Edition, John Wiley & Sons, Inc., New York.

29. Ismail, K.A.R and Salinas, C.S., 1999, "Modeling of frost formation over parallel cold plates", Int. J. Refrigeration, 22, pp. 425-441.

30. Jia, X., Tso, C. P. Jolly, P. and Chia, P. K., 1995, "A distributed model for prediction of the transient response of an evaporator", Int. J. Refrigeration, 18, pp. 336-342.

31. Jones, B.W. and Parker, J.D., 1975, "Frost formation with varying environmental parameters", ASME Journal of Heat Transfer, 97, pp. 255-259.

32. Kays, W.M. and London, A.L., 1984, "Compact heat exchangers", Second edition, McGraw-Hill, New York, NY.

33. Kline, S.J. and McClintock, F.A., 1953, "Describing uncertainties in single-sample experiments", Mechanical Engineering, 75, pp. 3-8.

34. Kondepudi, S.N. and O'Neal, D.L., 1989a, "The performance of finned tube heat exchangers under frosting conditions", ASME collected paper in Heat Transfer,HTD- 123, pp. 193-200.

35. Kondepudi, S.N. and O'Neal, D.L., 1989b, "Effect of frost growth on the performance of louvered finned tube heat exchangers", Int. J. Refrigeration 12(3), pp. 151-158.

36. Kondepudi, S.N. and O'Neal, D.L., 1990, "The effects of different fin configurations on the performance of finned-tube heat exchangers under frosting conditions", ASHRAE Transaction, 96 (2), pp.439-444.

37. Kondepudi, S.N. and O'Neal, D.L., 1991, "Frosting performance of tube heat exchangers with wavy and corrugated fins", Experimental Thermal and Fluid Science 4(5), pp. 613-618.

38. Kondepudi, S.N. and O'Neal, D.L., 1993a, "Performance of finned-tube heat exchanger under frosting conditions: I. Simulation model, Int. J. Refrigeration, 16(3), pp. 175-180.

39. Kondepudi, S.N. and O'Neal, D.L., 1993b, "Performance of finned-tube heat exchanger under frosting conditions: II. Comparison of experimental data with model, Int. J. Refrigeration, 16(3), pp. 181-184.

40. Le Gall, R., Grillot, J.M. and Jallut, C., 1997, "Modeling of frost growth and densification", Int. J. Heat Mass Transfer, 40(13), pp. 3177-3187.

41. Lee Y.B. and Ro, S.T., 2001, "An experimental study of frost formation on a horizontal cylinder under cross flow", Int. J. Refrigeration, 24, pp. 468-474.

42. Lee, K.S., Jhee, S. and Yang, DK., 2003, "Prediction of the frost formation on a cold flat surface", Int. J Heat Mass Transfer, 46, pp. 3789-3796.

43. Lee, K.S., Lee, T.H. and Kim, W.S., 1994, "Heat and mass transfer of parallel plate heat exchanger under frosting condition", SAREK Journal, 6, pp.155-165.

44. Luer, A. and Beer, H., 2000, "Frost deposition in a parallel plate channel under laminar flow conditions", Int. J. Therm. Sci. 39, pp. 85-95.

45. MacArthur, J. W., 1984, "Transient heat pump behavior: a theoretical investigation", Int. J. Refrigeration, 7(2), pp. 123-132.

46. Mago, P. J. and Sherif, S. A., 2002, "Modeling the cooling process path of dehumidifying coil under frosting conditions", ASME Journal of Heat Transfer, 124, pp. 1182-1191.

47. Mao, Y., Besant, R.W. and Chen, H., 1999, "Frost characteristics and heat transfer on a flat plate under freezer operating conditions: Part I, experimentation and correlations", ASHRAE Transactions, 105(2), pp. 231-239.

48. Mao, Y., Besant, R.W. and Rezkallah, K.S., 1992, "Measurement and correlations of frost properties with air flow over a flat plate", ASHRAE Transactions, 98 (1), pp. 65-78.

49. Marinyuk, B.T., 1980, "Heat and mass transfer under frosting conditions", Int. J. Refrigeration, 3(6), pp. 366-368.

50. Martinez-Frias, J. and Aceves, S.M., 1999, "Effects of evaporator frosting on the performance of an air-to-air heat pump", ASME Journal of Energy Resources Technology, 121(1), pp. 60-65.

51. Mason, B.J. and Hallet, 1971, The physics of clouds, Clarendon Press, Oxford, 1971.

52. Na, B. and Webb, R.L., 2004, Int. J. Heat Mass Transfer, 47, pp. 899-911.

53. Niederer, D.H., 1976, "Frosting and defrosting effects on coil heat transfer", ASHRAE Transactions, 81(1), pp. 467-473.

54. Nyers, J., Stoyan, G., 1994, "Dynamic model adequate for controlling the evaporator of a heat pump", Int. J. Refrigeration, 17, pp. 101-108.

55. O'Neal, D.L. and Tree, D.R., 1984, "Measurement of frost growth and density in a parallel plate geometry", ASHRAE Transactions, 90(2A), pp. 278-290.

56. O'Neal, D.L. and Tree, D.R., 1985, "A review of frost formation in simple geometries", ASHRAE Transactions, 91 (2A), pp. 267-281.

57. Ogawa, K., Tanaka, N. and Tekeshita, M., 1993, "Performance improvement of plate fin-and –tube heat exchangers under frosting conditions", ASHRAE Transactions, 99 (1), pp. 762-771.

58. Oskarsson, S.P., Krakow, K.I. and Lin, S., 1990a, "Evaporator models for operation with dry, wet and frosted finned surfaces, Part I: Heat transfer and fluid flow theory", ASHRAE Transactions, 96 (1), pp. 373-380.

59. Oskarsson, S.P., Krakow, K.I. and Lin, S., 1990b, "Evaporator models for operation with dry, wet and frosted finned surfaces, Part II: Evaporator models verification", ASHRAE Transactions, 96 (1), pp. 381-392.

60. Ostin, R. and Anderson, S., 1991, "Frost growth parameters in a forced air stream", Int. J. Heat Mass Transfer, 34 (4), pp. 1009-1017.

61. Parish, H.C. and Sepsy, C.F., 1972, "A numerical analysis of frost formation under forced convection", ASHRAE Transaction, 78, pp. 236-251.

62. Payne, W.V. and O'Neal, D.L., 1994, "A temperature-based variable for monitoring outdoor coil airflow in an air-source heat pump during frost forming conditions", ASHRAE Transactions, 100, pp. 131-139.

63. Premoli, A., Francesco, D., and Prina, A. A., 1971, "Dimensionless correlation for determining the density of two-phase mixtures", Lo Termotecnica, 25, pp. 17-26.

64. Rite, R.W. and Crawford, R.R., 1991a, "The effect of frost accumulation on the performance of domestic refrigerator-freezer finned-tube evaporator coils, ASHRAE Transactions, 97(2), pp. 428-437.

65. Rite, R.W. and Crawford, R.R., 1991b, "A parametric study of the factors governing the rate of frost accumulation on domestic refrigerator-freezer finned-tube evaporator coils", ASHRAE Transaction, 97 (2), pp. 438-446.

66. Sami, S.M. and Duong, T., 1989, "Mass and heat transfer during frost growth", ASHRAE Transactions, 95 (1), pp. 158-165.

67. Sanders, C., 1974, "The influence of frost formation and defrosting on the performance of air coolers", Ph.D. Dissertation, Technische Hogeschool, Delft University – Netherlands.

68. Schneider, H.W., 1978, "Equation of the growth rate of frost forming on cooled surfaces", Int. J. Heat Mass Transfer, 21, pp. 1019-1024.

69. Schulte, D.W. and Howell, R. H., 1982, "The effect of air turbulence on the rate of frost growth on a horizontal flat plate", ASHRAE Transactions, 88 (2), pp. 201-217.

70. Sekar, D., Kartas, H. and Egrican, N., 2004a, "Frost formation on fin-and-tube heat exchangers. Part I- Modeling of frost formation on fin-and-tube heat exchangers", Int. J. Refrigeration, 27, pp. 367-374.

71. Sekar, D., Kartas, H. and Egrican, N., 2004b, "Frost formation on fin-and-tube heat exchangers. Part II- Experimental investigation of frost formation on fin-and-tube heat exchangers", Int. J. Refrigeration, 27, pp. 375-377.

72. Senshu, T., Yasuda, H., Oguni, K. and Ishibane, K., 1990, "Heat pump performance under frosting conditions: Part I- heat and mass transfer on cross-finned tube heat exchangers under frosting conditions", ASHRAE Transaction, 96 (1), pp. 324-329.

73. Sherif, S.A., Raju, S.P., Padki, M.M. and Chan, A.B., 1993, "Semi-empirical transient method for modeling frost formation on a flat plate", Int. J. Refrigeration 16(5), pp. 321-329.

74. Smith, S.L., 1970, "Void fraction in two-phase flow: A correlation based upon an equal velocity head model", Proceedings of Inst. of Mechanical Engineers, 184(36), pp. 647-664.

75. Stoecker, W.F and Jones, J.W., 1982, "Refrigeration & air conditioning", McGraw-Hill, pp.239-242.

76. Stoecker, W.F, 1957, "How frost formation on coils affects refrigeration system", Refrigeration Engrg., pp. 42.

77. Stoecker, W.F., 1960, "Frost formation on refrigeration coils", ASHRAE Transactions, 96(1), pp. 91-103.

78. Tantakitti, C. and Howell, R.H., 1986, "Air-to-air heat pumps operating under frosting conditions on the outdoor coil", ASHRAE Transactions, 92(1B), pp. 827-842.

79. Tao, Y.X. and Besant, R.W., 1993, "Prediction of spatial and temporal distributions of frost growth on a flat plate under forced convection", Journal of Heat Transfer, 115, pp. 278-281.

80. Tassou, S.A. and Marquand, C.J., 1987, "Effects of evaporator frosting and defrosting on the performance of air-to-water heat pumps", Applied Energy, 28(1), pp. 19-33.

81. Wang, C.C. and Chi, K.U., 2000, "Heat transfer and friction characteristics of plain fin-and-tube heat exchangers; Part 2; Correlation", Int. J. Heat Mass Transfer, 43, pp. 2692-2700.

82. Wang, H. and Touber, S., 1991, "Distributed and non-steady-state modeling of an air cooler", Int. J. Refrigeration, 14, pp. 98-111.

83. Waters, R.J., O'Neal, D.L. and Yang, J., 2001a, "Effect of fin staging on frost/defrost performance of a two-row heat pump evaporator at standard test conditions", ASHRAE Transaction, 107(2), pp. 240-249.

84. Waters, R.J., O'Neal, D.L. and Yang, J., 2001b, "Effect of fin staging on frost/defrost performance of a two-row heat pump evaporator under heavy frosting conditions", ASHRAE Transaction, 107(2), pp. 250-258.

85. White, J.E. and Creamers, C.J., 1981, "Prediction of growth parameters of frost deposits in forced convection", ASME Journal of Heat Transfer, 103, pp. 3-6.

86. Williams, H.P., Brian, P.F., Saul, A.T. and Williams, T.V., 1986, "Numerical Recipes – the Art of scientific computing", Cambridge University Press.

87. Wongwises, S., Disawas, S., Kaewon, J. and Onurai, C., 2000, "Two-phase Evaporative Heat Transfer Coefficients of Refrigerant HFC-134a Under

Forced Flow Conditions in a Small Horizontal Tube**",** Int. Comm. in Heat and Mass Transfer, 27 (1), pp. 35-48.

88. Yamakawa, N., Takahashi, N. and Ohtani, S., 1972, "Forced convection heat and mass transfer under frost conditions", Heat Transfer- Japanese Research, Vol(1), No. 2, pp. 1-9.

89. Yan, WM., Li, HY., Wu, YJ., Lin, JY. and Chang, WR., 2003, "Performance of finned tube heat exchangers operating under frosting conditions, Int. J. Heat Mass Transfer, 46, pp. 871-877.

90. Yao, Y., Jian, Y., Deng, S. and Ma, Z., 2004, "A study on the performance of the air side heat exchanger under frosting in an air source heat pump water heater/chiller unit", Int. J. Heat Mass Transfer , 47, pp. 3745-3756.

91. Yasuda H., Senshu, T., Kuroda, S., Atsumi, A. and Oguni, K., 1990, "Heat pump performance under frosting conditions: Part II- simulation of Heat Pump cycle characteristics under frosting conditions", ASHRAE Transaction, 96 (1), pp. 330-336.

92. Yonko, J.D. and Sepsy, C.F., 1967, "An investigation of the thermal conductivity of frost while forming on a flat horizontal plate", ASHRAE Transactions, 73, pp. I.1.1-I.1.11.

Appendix

Uncertainty Analysis

The method used for the uncertainty calculation is the one described by Kine and McClintock (1953). Suppose that a result "R" is a function of a number of independent variables X_1, X_2, X_3, …, X_n.

$$R = R(X_1, X_2, X_3, \ldots, X_n) \tag{A-1}$$

And each of those variables has an uncertainty $\left(\xi_{x_1}, \xi_{x_2}, ..., \xi_{x_n}\right)$. The total uncertainty in the result, "ξ_R", is found through the following equation:

$$\xi_R = \left[\left(\frac{\partial R}{\partial X_1}\xi_{X_1}\right)^2 + \left(\frac{\partial R}{\partial X_2}\xi_{X_2}\right)^2 + \ldots + \left(\frac{\partial R}{\partial X_n}\xi_{X_n}\right)^2\right]^{1/2} \tag{A-2}$$

Energy Transfer rate

$$Q = m_r (h_{r,out} - h_{r,in}) \tag{A-3}$$

where m_r is refrigerant mass flow rate (kg/s), $h_{r,in}$ is the inlet refrigerant enthalpy (J/kg) and $h_{r,out}$ is the outlet refrigerant enthalpy (J/kg).

The uncertainty in energy transfer rate, Equation A-4, is proportional to the root mean square sum of the uncertainty contributions of each independent parameter that defines energy transfer rate in Equation A-3.

$$\xi_Q = \left[\left(\frac{\partial Q}{\partial m_r} \right)^2 \left(\xi_{m_r} \right)^2 + \left(\frac{\partial Q}{\partial h_{r,in}} \right)^2 \left(\xi_{h_{r,in}} \right)^2 + \left(\frac{\partial Q}{\partial h_{r,out}} \right)^2 \left(\xi_{h_{r,out}} \right)^2 \right]^{1/2} \quad \text{(A-4)}$$

The refrigerant flow rate is a directly measured value, as the uncertainty in flow rate is directly related to the flow meter. On the other hand, the uncertainties in the inlet and outlet refrigerant enthalpies were derived from directly measured pressures and temperatures.

The enthalpy of the refrigerant is a function of temperature and pressure. Therefore, the uncertainty can be determined using Equation A-2. The uncertainty for inlet refrigerant enthalpy can be calculated as follow:

$$\xi_{h_{r,in}} = \left[\left(\frac{\partial h_{r,in}}{\partial T_r} \right)^2 \left(\xi_{T_r} \right)^2 + \left(\frac{\partial h_{r,in}}{\partial p_r} \right)^2 \left(\xi_{p_r} \right)^2 \right]^{1/2}$$